2010

Statistics of the received power for free space optical channels

Stephen D. Lyke
Michigan Technological University

STATISTICS OF THE RECEIVED POWER FOR FREE SPACE OPTICAL CHANNELS

By

STEPHEN D. LYKE

A DISSERTATION

Submitted in partial fulfillment of the requirements

for the degree of

DOCTOR OF PHILOSOPHY

(Electrical Engineering)

MICHIGAN TECHNOLOGICAL UNIVERSITY

2010

This dissertation, "Statistics of the Received Power for Free Space Optical Channels", is hereby approved in partial fulfillment of the requirements for the degree of DOCTOR OF PHILOSOPHY in the field of Electrical Engineering.

DEPARTMENT:
Electrical and Computer Engineering

Signatures:

Dissertation Advisor _____
Dr. Michael C. Roggemann

Department Chair _____
Dr. Daniel R. Fuhrmann

Date _____

To my advisor Michael C. Roggemann, without whom this dissertation would not have been possible. Mike, your advice and guidance has been invaluable. Thank You!

Contents

List of Figures **xiii**

List of Tables **xv**

Acknowledgments **xvii**

Abstract **xix**

1 Introduction **1**

1.1 Atmospheric Turbulence 3

1.1.1 Refractive Index Fluctuations 4

1.1.2 Power Spectrum of Refractive Index Fluctuations 6

1.1.2.1 Kolmogorov Spectrum 7

1.1.2.2 Tatarskii Spectrum 8

1.1.2.3 von Kármán Spectrum 9

1.1.3 Atmospheric Temporal Statistics and Taylor's Hypothesis 9

1.2 Free Space Optical Communication 11

1.2.1 Brief Review of Communication Systems 12

1.2.2 Optical Communication Through Atmospheric Turbulence 13

1.3 Approach 14

1.4 Summary of Key Results 17

1.5 Organization of Dissertation 19

2 Probability density of aperture averaged irradiance fluctuations for long range free space optical communication links 21

2.1 Introduction 21

2.2 Background 24

2.2.1 Probability Density Function Models 24

2.2.1.1 Gamma-Gamma Probability Density Function 25

2.2.1.2 Lognormal Probability Density Function 26

2.2.2 Scintillation 26

2.2.3 Summary of Recent Relevant Scintillation Study 28

2.3 Simulation 29

2.3.1 Simulation Description 29

2.3.2 Comparison to Previous Simulation Results 33

2.4 Results 36

2.4.1 Probability Distribution 36

2.4.2 Bit Error Rate 49

2.5 Conclusions 51

3 Probability density of received optical power fluctuations for adaptively compensated Gaussian laser beams 53

3.1 Introduction 53

3.2 Theory 56

3.2.1 Probability Density Function Models 56

3.2.1.1 Gamma-Gamma Probability Density Function 57

3.2.1.2 Lognormal Probability Density Function 58

3.2.2 Adaptive Optics System 60

3.2.2.1 Laser Beacon 60

3.2.2.2 Tilt Correction 61

3.2.2.3 Wavefront Sensor 62

3.2.2.4 Deformable Mirror 64

3.3 Simulation 65

3.4 Results 68

3.4.1 Probability Distribution 68

3.4.2 Bit-Error Rate 75

3.5 Conclusions 82

4 Temporal power spectral density of the received power for a free space optical channel and coherence times 85

4.1 Introduction 85

4.2 Background 89

4.2.1 Temporal Fading Channel 89

4.2.2 Detection of received signal 90

4.3 Simulation 91

4.4 Experiment, System Design, and Data Collection 97

4.4.1 Transmitter 98

4.4.2 Receiver 99

4.4.3 Data Collection 101

4.4.4 Coherence Time Calculation 102

4.5 Results and Discussion 103

4.5.1 Simulation Results 103

4.5.2 Experimental Results 105

4.6 Conclusions 106

5 Conclusions **109**

5.1 Summary of Dissertation 109

5.2 Summary of Key Results 112

5.3 Future Work 114

Bibliography **115**

Index **121**

List of Figures

1.1 Kolmogorov and von Kármán turbulence spectral models. $C_n^2 = 10^{-15}\,\mathrm{m}^{-2/3}$ with $l_0 = 5$ mm, and $L_0 = 2, 5$, and 10 m for the von Kármán model. 10

2.1 PDF of the normalized log irradiance $\ln(I)$ for the receiving apertures of diameter 1.8 mm, 5 mm, and 13 mm. Simulation results for two turbulence strengths $C_n^2 = 6.47 \times 10^{-14}\, m^{-2/3}$ and $C_n^2 = 4.58 \times 10^{-13}\, m^{-2/3}$ respectively are compared to gamma-gamma and lognormal PDFs. Results compare to Fig. 3 in [1]. 35

2.2 PDF of the normalized log irradiance $\ln(I)$ for the receiving apertures of diameter 5.6 mm ((a),(c),(e)) and $\rho_0/2$ ((b),(d),(f)). Simulation results for turbulence strength $C_n^2 = 1 \times 10^{-18}\ m^{-2/3}$ and propagation distance of 50 km, 75 km, and 100 km are compared to the gamma-gamma and lognormal PDF for each case. 38

2.3 PDF of the normalized log irradiance $\ln(I)$ for the receiving apertures of diameter ρ_0 ((a),(c),(e)) and $3\rho_0/2$ ((b),(d),(f)). Simulation results for turbulence strength $C_n^2 = 1 \times 10^{-18}\ m^{-2/3}$ and propagation distance of 50 km, 75 km, and 100 km are compared to the gamma-gamma and lognormal PDF for each case. 39

2.4 PDF of the normalized log irradiance $\ln(I)$ for the receiving apertures of diameter 5.6 mm ((a),(c),(e)) and $\rho_0/2$ ((b),(d),(f)). Simulation results for turbulence strength $C_n^2 = 1 \times 10^{-17}\ m^{-2/3}$ and propagation distance of 50 km, 75 km, and 100 km are compared to the gamma-gamma and lognormal PDF for each case. 42

2.5 PDF of the normalized log irradiance $\ln(I)$ for the receiving apertures of diameter ρ_0 ((a),(c),(e)) and $3\rho_0/2$ ((b),(d),(f)). Simulation results for turbulence strength $C_n^2 = 1 \times 10^{-17}\ m^{-2/3}$ and propagation distance of 50 km, 75 km, and 100 km are compared to the gamma-gamma and lognormal PDF for each case. 43

2.6 PDF of the normalized log irradiance $\ln(I)$ for the receiving apertures of diameter 5.6 mm ((a),(c),(e)) and $\rho_0/2$ ((b),(d),(f)). Simulation results for turbulence strength $C_n^2 = 1 \times 10^{-16}\ m^{-2/3}$ and propagation distance of 50 km, 75 km, and 100 km are compared to the gamma-gamma and lognormal PDF for each case. 44

2.7 PDF of the normalized log irradiance $\ln(I)$ for the receiving apertures of diameter ρ_0 ((a),(c),(e)) and $3\rho_0/2$ ((b),(d),(f)). Simulation results for turbulence strength $C_n^2 = 1 \times 10^{-16}\ m^{-2/3}$ and propagation distance of 50 km, 75 km, and 100 km are compared to the gamma-gamma and lognormal PDF for each case. 45

2.8 PDF of the normalized log irradiance $\ln(I)$ for the receiving apertures of diameter 5.6 mm ((a),(c),(e)) and $\rho_0/2$ ((b),(d),(f)). Simulation results for turbulence strength $C_n^2 = 1 \times 10^{-15}\ m^{-2/3}$ and propagation distance of 50 km, 75 km, and 100 km are compared to the gamma-gamma and lognormal PDF for each case. 47

2.9 PDF of the normalized log irradiance $\ln(I)$ for the receiving apertures of diameter ρ_0 ((a),(c),(e)) and $3\rho_0/2$ ((b),(d),(f)). Simulation results for turbulence strength $C_n^2 = 1 \times 10^{-15}\ m^{-2/3}$ and propagation distance of 50 km, 75 km, and 100 km are compared to the gamma-gamma and lognormal PDF for each case. 48

2.10 BER of the laser communication channel for the point-like and $3\rho_0/2$ diameter apertures for propagation distances of 75 km and 100 km and for turbulence strengths $C_n^2 = 1 \times 10^{-16}\,\mathrm{m}^{-2/3}$ ((a),(b)) and $C_n^2 = 1 \times 10^{-15}\,\mathrm{m}^{-2/3}$ ((c),(d)). 50

3.1 Wavefront sensor showing subaperture locations and subaperture centers for a. low order (12 subapertures), b. medium order (24 subapertures), and c. high order (52 subapertures) configurations 63

3.2 PDF of the normalized log irradiance $\ln(I)$ for an uncompensated Gaussian beam for the receiving apertures of diameter 5.6 mm(point receiver)(a), $\rho_0/2$ (b), ρ (c), and $3\rho/2$ (d). Simulation results for turbulence strength $C_n^2 = 1 \times 10^{-15}\ m^{-2/3}$ and propagation distance of 10 km are compared to the gamma-gamma and lognormal PDF for each case. 70

3.3 PDF of the normalized log irradiance $\ln(I)$ for a low order adaptively compensated Gaussian beam for the receiving apertures of diameter 5.6 mm(point receiver)(a), $\rho_0/2$ (b), ρ (c), and $3\rho/2$ (d). Simulation results for turbulence strength $C_n^2 = 1 \times 10^{-15}\ m^{-2/3}$ and propagation distance of 10 km are compared to the gamma-gamma and lognormal PDF for each case. . . . 71

3.4 PDF of the normalized log irradiance $\ln(I)$ for a medium order adaptively compensated Gaussian beam for the receiving apertures of diameter 5.6 mm(point receiver)(a), $\rho_0/2$ (b), ρ (c), and $3\rho/2$ (d). Simulation results for turbulence strength $C_n^2 = 1 \times 10^{-15}\ m^{-2/3}$ and propagation distance of 10 km are compared to the gamma-gamma and lognormal PDF for each case. 72

3.5 PDF of the normalized log irradiance $\ln(I)$ for a high order adaptively compensated Gaussian beam for the receiving apertures of diameter 5.6 mm(point receiver)(a), $\rho_0/2$ (b), ρ (c), and $3\rho/2$ (d). Simulation results for turbulence strength $C_n^2 = 1 \times 10^{-15}\ m^{-2/3}$ and propagation distance of 10 km are compared to the gamma-gamma and lognormal PDF for each case. 73

3.6 PDF of the normalized log irradiance $\ln(I)$ for an uncompensated Gaussian beam for the receiving apertures of diameter 5.6 mm(point receiver)(a), $\rho_0/2$ (b), ρ (c), and $3\rho/2$ (d). Simulation results for turbulence strength $C_n^2 = 1 \times 10^{-15}\ m^{-2/3}$ and propagation distance of 20 km are compared to the gamma-gamma and lognormal PDF for each case. 74

3.7 PDF of the normalized log irradiance $\ln(I)$ for a low order adaptively compensated Gaussian beam for the receiving apertures of diameter 5.6 mm(point receiver)(a), $\rho_0/2$ (b), ρ (c), and $3\rho/2$ (d). Simulation results for turbulence strength $C_n^2 = 1 \times 10^{-15}\ m^{-2/3}$ and propagation distance of 20 km are compared to the gamma-gamma and lognormal PDF for each case. . . . 75

3.8 PDF of the normalized log irradiance $\ln(I)$ for a medium order adaptively compensated Gaussian beam for the receiving apertures of diameter 5.6 mm(point receiver)(a), $\rho_0/2$ (b), ρ (c), and $3\rho/2$ (d). Simulation results for turbulence strength $C_n^2 = 1 \times 10^{-15}\ m^{-2/3}$ and propagation distance of 20 km are compared to the gamma-gamma and lognormal PDF for each case. 76

3.9 PDF of the normalized log irradiance $\ln(I)$ for a high order adaptively compensated Gaussian beam for the receiving apertures of diameter 5.6 mm(point receiver)(a), $\rho_0/2$ (b), ρ (c), and $3\rho/2$ (d). Simulation results for turbulence strength $C_n^2 = 1 \times 10^{-15}\ m^{-2/3}$ and propagation distance of 20 km are compared to the gamma-gamma and lognormal PDF for each case. 77

3.10 BER of the laser communication channel for the uncompensated laser (a, b) and low order compensated laser (c, d) for the ρ_0 diameter aperture and 10 km and 20 km link distances respectively. 78

3.11 BER of the laser communication channel for the medium order compensated laser (a, b) and high order compensated laser (c, d) for the ρ_0 diameter aperture and 10 km and 20 km link distances respectively. 79

3.12 Intensity spot at the transmitter (a) and at the receiver (b) for the 10 km link distance showing the non-reciprocal nature of the long distance propagation path. 80

4.1 Transmitter:Extended view. 99

4.2 Transmitter:View from the top shows directions of adjustments required for proper alignment of the transmitter with the receiver 99

4.3 Receiver:Extended view 100

4.4 Receiver:Details of the WFS assembly 101

4.5 PSD for 25 km link distance and aperture diameters 0.68 cm, 5 cm, 15 cm, and 50 cm (a) and PSD for 5 cm aperture and all link distances (b) showing that in both cases the PSD narrows, indicating that the coherence time measured from the associated correlation function is increasing 105

List of Tables

2.1 Table 1. Numerical simulation parameters 30

4.1 Table 1. Coherence times per aperture diameter for simulated data 103

4.2 Table 2. Coherence times per aperture diameter for experimental data 106

Acknowledgments

My journey here at Michigan Tech is nearly complete. It has been quite a roller coaster of ups and downs, though thankfully mostly ups. Dr. Roggemann has been more than patient with me, while I struggled with my research. His mentorship has been invaluable and that is why this dissertation is dedicated to him.

I am also very grateful to Dr. David Voelz for the time he has spent working with me. He has been very gratious and helpful and I have learned so much in such a short time. I am very fortunate to have had the opportunity to work with Dave.

I would like to thank Dr. Zhijun Zhao (Zach) for his advice and guidance both in my studies and in my research. Also, I want to thank Dr. Christopher Middlebrook and Dr. Barbara Bertram for their helpful comments and advice regarding this dissertation. Also, I appreciate working with the people in this department. I value the friendships I have made and am sure our paths will cross from time to time in the future.

Finally, I want to thank my family and friends for their support and encouragement while I was pursuing my doctoral degree. I couldn’t have done it without you!

Abstract

Free space optical (FSO) communication links can experience extreme signal degradation due to atmospheric turbulence induced spatial and temporal irradiance fluctuations (scintillation) in the laser wavefront. In addition, turbulence can cause the laser beam centroid to wander resulting in power fading, and sometimes complete loss of the signal. Spreading of the laser beam and jitter are also artifacts of atmospheric turbulence. To accurately predict the signal fading that occurs in a laser communication system and to get a true picture of how this affects crucial performance parameters like bit error rate (BER) it is important to analyze the probability density function (PDF) of the integrated irradiance fluctuations at the receiver. In addition, it is desirable to find a theoretical distribution that accurately models these fluctuations under all propagation conditions. The PDF of integrated irradiance fluctuations is calculated from numerical wave-optic simulations of a laser after propagating through atmospheric turbulence to investigate the evolution of the distribution as the aperture diameter is increased. The simulation data distribution is compared to theoretical gamma-gamma and lognormal PDF models under a variety of scintillation regimes from weak to very strong. Our results show that the gamma-gamma PDF provides a good fit to the simulated data distribution for all aperture sizes studied from weak through moderate scintillation. In strong scintillation, the gamma-gamma PDF is a better fit to the distribution for point-like apertures and the lognormal PDF is a better fit for apertures the size of the atmospheric spatial coherence radius ρ_0 or larger. In addition, the PDF of received

power from a Gaussian laser beam, which has been adaptively compensated at the transmitter before propagation to the receiver of a FSO link in the moderate scintillation regime is investigated. The complexity of the adaptive optics (AO) system is increased in order to investigate the changes in the distribution of the received power and how this affects the BER. For the 10 km link, due to the non-reciprocal nature of the propagation path the optimal beam to transmit is unknown. These results show that a low-order level of complexity in the AO provides a better estimate for the optimal beam to transmit than a higher order for non-reciprocal paths. For the 20 km link distance it was found that, although minimal, all AO complexity levels provided an equivalent improvement in BER and that no AO complexity provided the correction needed for the optimal beam to transmit. Finally, the temporal power spectral density of received power from a FSO communication link is investigated. Simulated and experimental results for the coherence time calculated from the temporal correlation function are presented. Results for both simulation and experimental data show that the coherence time increases as the receiving aperture diameter increases. For finite apertures the coherence time increases as the communication link distance is increased. We conjecture that this is due to the increasing speckle size within the pupil plane of the receiving aperture for an increasing link distance.

Chapter 1

Introduction

The current limit to commercially available free space optical (FSO) communication link distances is only a few kilometers. The main reason for this is turbulence within the atmosphere along the path through which the laser beam must propagate. However, there is interest in long range FSO link distances on the order of several tens of kilometers. Some applications for such long links are airborne laser platforms, mountaintop to mountaintop communication links, communication with satellites, or some combination of these.

FSO communication system performance can be severely degraded by turbulence induced fluctuations in the received signal, otherwise known as scintillation. Scintillation can lead to loss of recieved power or fading of the signal below a prescribed threshold [2]. The reliablility of an FSO system can be deduced from a mathematical model for the probability

density function (PDF) of the fluctuating signal [2].

One of the goals of this research is to characterize to PDF of the received power from an uncompensated Gaussian laser beam after having propagated through atmospheric turblence for longer links than have been evaluated previously. How the PDF of the received power evolves with aperture size for different scintillation conditions is investigated. Another goal is to characterize the PDF of the received power from an adaptively compensated Gaussian laser beam. How the PDF of the received power is affected by increasing the complexity in the adaptive optics (AO) is examined. In addition, we evaluate the performance of the FSO link by analyzing the bit error rate (BER) while increasing the AO complexity. The final goal of this research is to explore the power spectral density (PSD) of the received power for various reciever aperture diameters and link distances. The channel coherence times associated with the PSD for an increasing aperture size and longer link distances than shown previously are presented.

This dissertation is comprised of three separate but related studies investigating the statistics of the received power for FSO links and how atmospheric turbulence affects those statistics. The first study, detailed in chapter 2, involves characterizing the probability density function (PDF) of the received power from an uncompensated Gaussian beam. The second study, detailed in chapter 3, expands on the findings of chapter 2 by adding adaptive optics (AO) to the system. This study investigates the influences on the PDF of the received power and on the bit error rate (BER) of the FSO channel from increasing the complexity

of the AO. Finally the third study, detailed in chapter 4, investigates the temporal power spectral density (PSD) of the received power and the associated coherence times of the atmospheric channel. In this chapter, the affects that increasing the receiver aperture diameter as well as the link distance has on the PSD and the coherence times is investigated.

This chapter is outlined as follows. Section 1.1 begins with a review of atmospheric turbulence and the forces that influence its creation. In section 1.1.1, the refractive index fluctuations within the atmosphere are discussed in mathematical detail followed by a discussion of the different power spectrum models of the refractive index fluctuations, which can be found in section 1.1.2. In section 1.1.3, the temporal statistics of the atmosphere is discussed including Taylor's hypothesis. Section 1.2 is comprised of an overview of free space optical communication beginning with a review of communications given in section 1.2.1 followed by communications through a turbulent atmosphere given in section 1.2.2. Section 1.3 outlines the approach that we take to the studies contained within this thesis. Finally, section 1.4 gives a summary of the key results found in each study followed by an outline of the thesis.

1.1 Atmospheric Turbulence

Solar heating of the earth's surface and subsequent cooling during the night leads to variations in the temperature gradient within the atmosphere. These temperature gradients cause

fluctuations in the mean velocity field within the atmosphere, otherwise known as wind [2]. Temperature gradients also cause random large and small scale motions called turbulent eddies within the mean velocity field. These eddies are unstable randomly distributed and randomly sized air pockets independent of the surrounding air mass. Due to the influence of inertial forces, larger eddies break up into smaller eddies and those into even smaller eddies so that there is a transfer of energy from large scale air masses, characterized by the atmospheric outer scale L_0 to small scale air masses, characterized by the atmospheric inner scale l_0 [2]. L_0 can vary in size depending upon the altitude. Near the ground the scale of L_0 is approximately the height above ground, while in higher altitudes L_0 can range in size from several meters to a few tens of meters [3]. The inner scale l_0 on the other hand is on the order of a few millimeters near the ground but can be on the order of centimeters in the troposphere and stratosphere [2]. The turbulence eddy scale range, which is bounded above by L_0 and below by l_0 is known as the inertial subrange [2]. Scale sizes below l_0 fall into the viscous dissipation range, where eddies disappear and the remaining energy is dissipated as heat [2].

1.1.1 Refractive Index Fluctuations

The index of refraction $n(\vec{r},t)$ is an important parameter in the atmosphere in terms of optical wave propagation. Temperature fluctuations combined with turbulent mixing create a random behavior to the atmospheric index of refraction, which is very sensitive to small-

scale temperature fluctuations [2]. The index of refraction at a three dimensional position $\vec{r}$ and time t can be mathematically expressed by [3]

$$n(\vec{r},t) = n_0 + n_1(\vec{r},t), \tag{1.1}$$

where $n_0 \cong 1$ is the mean value of the index of refraction and $n_1(\vec{r},t)$ is a random deviation of $n(\vec{r},t)$ from its mean so that $\langle n_1(\vec{r},t)\rangle = 0$. These fluctuations in the refractive index $n_1(\vec{r})$ (where the dependance on time has been removed) are related to corresponding temperature and pressure fluctuations. Hence, the refractive index fluctuation term can be written as [2]

$$\begin{aligned} n_1(\vec{r}) &= 77.6\times 10^{-6}\left(1+7.52\times 10^{-3}\lambda^{-2}\right)\frac{P(\vec{r})}{T(\vec{r})} \\ &\cong 79\times 10^{-6}\frac{P(\vec{r})}{T(\vec{r})}, \end{aligned} \tag{1.2}$$

where λ is the optical wavelength and was set to $\lambda \approx 0.5\mu$m in the second expression, P is the air pressure in millibars, and T is the air temperature in Kelvin. Index of refraction fluctuations are due primarily to temperature variations within the atmosphere since fluctuations in pressure are usually negligible [2, 3]. Since $\langle n_1(\vec{r})\rangle = 0$, the covariance function of $n(\vec{r})$ can be expressed as [2]

$$B_n(\vec{r_1},\vec{r_2}) = B_n(\vec{r_1},\vec{r_1}+\vec{r}) = \langle n_1(\vec{r_1})n_1(\vec{r_1}+\vec{r})\rangle, \tag{1.3}$$

which can be reduced to a function of the scalar distance $r = |\vec{r}_1 - \vec{r}_2|^2$ if the random field of index of refraction fluctuations is statistically homogeneous and isotropic [2]. In that case, the structure function of r can be expressed as [2]

$$D_n(r) = 2[B_n(0) - B_n(r)] = \begin{cases} C_n^2 l_0^{-4/3} r^2, & 0 \leq r << l_0 \\ C_n^2 r^{2/3}, & l_0 << r << L_0, \end{cases} \tag{1.4}$$

where C_n^2 is a measure of the strength of the fluctuations in the refractive index and is known as the refractive index structure parameter with units of $m^{-2/3}$. C_n^2 values typically range from $10^{-17}\,\mathrm{m}^{-2/3}$ or less for weak turbulence conditions up to $10^{-13}\,\mathrm{m}^{-2/3}$ or more for strong turbulence conditions. It is reasonable to assume that C_n^2 is constant over short time intervals for a fixed propagation distance and at a fixed height above ground. In the studies discussed within this dissertation, it is assumed that C_n^2 is constant and that the propagation paths are horizontal.

1.1.2 Power Spectrum of Refractive Index Fluctuations

The statistical distribution and size of the turbulent eddies discussed earlier are characterized by the power spectral density of $n(r)$, which is related to the covariance function under the assumption of a statistically homogeneous and isotropic atmosphere by the three-

dimensional Fourier transform [2]

$$\begin{aligned}\Phi_n(\kappa) &= \frac{1}{(2\pi)^3}\int\int\int_{-\infty}^{\infty} B_n(r)\exp(-i\vec{\kappa}\cdot\vec{r})d^3r \\ &= \frac{1}{2\pi^2\kappa}\int_0^{\infty} B_n(r)\sin(\kappa r)r\,dr, \end{aligned} \tag{1.5}$$

where $\kappa = \sqrt{\kappa_x^2+\kappa_y^2+\kappa_z^2} = |\vec{\kappa}|$ is the scalar wavenumber with units of rad/m and spherical symmetry was used to obtain the last integral. The power spectral density and the covariance function are considered Fourier transform pairs, therefore it follows that [2]

$$B_n(r) = \frac{4\pi}{r}\int_0^{\infty} \kappa\Phi_n(\kappa)\sin(\kappa r)\,d\kappa. \tag{1.6}$$

Now, the relationship between the power spectrum and the structure function can be expressed as [2]

$$\begin{aligned} D_n(r) &= 2[B_n(0)-B_n(r)] \\ &= 8\pi\int_0^{\infty}\kappa^2\Phi_n(\kappa)\left(1-\frac{\sin\kappa r}{\kappa r}\right)d\kappa. \end{aligned} \tag{1.7}$$

1.1.2.1 Kolmogorov Spectrum

Kolmogorov theory for atmospheric scale sizes larger than L_0 does not predict a mathematical form for $\Phi_n(\kappa)$ nor does it predict a mathematical form for $\Phi_n(\kappa)$ for atmospheric scale sizes smaller than l_0. However, within the inertial subrange, $1/L_0 << \kappa << 1/l_0$, the

form for $\Phi_n(\kappa)$ predicted by Kolmogorov can be expressed as [2]

$$\Phi_n(\kappa) = 0.033 C_n^2 \kappa^{-11/3}, \tag{1.8}$$

which is known as the Kolmogorov power-law spectrum. It is widely used in theoretical calculations due to its simple mathematical form. It is useful to assume that $L_0 = \infty$ and that $l_0 = 0$ when working with this spectrum in order to justify its use for certain calculations over all wavenumbers [2]. The Kolmogorov power-law spectrum of Eq. 1.8 is used in the simulations of the projects defined within this dissertation.

1.1.2.2 Tatarskii Spectrum

Some applications require extension of the power spectrum into the dissipation range $\kappa > 1/l_0$. A spectrum model for refractive-index fluctuations, known as the Tatarskii model was developed that includes inner and outer scale effects. This model expressed below, essentially truncates the spectrum at high wavenumbers

$$\Phi_n(\kappa) = 0.033 C_n^2 \kappa^{-11/3} \exp\left(-\frac{\kappa^2}{\kappa_m^2}\right), \qquad \kappa >> 1/L_0, \tag{1.9}$$

where $\kappa_m = 5.92/l_0$.

1.1.2.3 von Kármán Spectrum

When Eqs. 1.8 or 1.9 are used to model the spectrum of index of refraction fluctuations in the $\kappa < 1/l_0$ regime or when $\kappa \to 0$ there can be mathematical problems due to a non-integrable pole at $\kappa = 0$ [3]. Therefore a spectrum model was developed to overcome this problem. That spectrum is known as the modified von Kármán spectrum and is given by [3]

$$\Phi_n(\kappa) = \frac{0.033 C_n^2}{(\kappa^2 + \kappa_0^2)^{11/6}} \exp\left\{-\frac{\kappa^2}{\kappa_m^2}\right\}, \tag{1.10}$$

where $\kappa_0 = 2\pi/L_0$ and $\kappa_m = 5.92/l_0$. Eq. 1.10 is referred to as the modified von Kármán spectrum because of the Gaussian term, which was added later to combine Tatarskii and the original von Kármán spectrums. The original model did not include this inner scale term and was as such including only outer scale effects. A plot of the Kolmogorov and von Kármán spectrums for $C_n^2 = 10^{-15}\,\mathrm{m}^{-2/3}$, $l_0 = 5$ mm, and $L_0 = 2, 5$, and 10 m is shown in Fig. 1.1.

1.1.3 Atmospheric Temporal Statistics and Taylor's Hypothesis

This dissertation involves the statistics of the received power from a free space optical communication link. The probability density functions examined in chapters 2 and 3 are calculated from an ensemble of data points of integrated optical power collected at the receiver from a Gaussian laser beam after having propagated through atmospheric turbulence. Be-

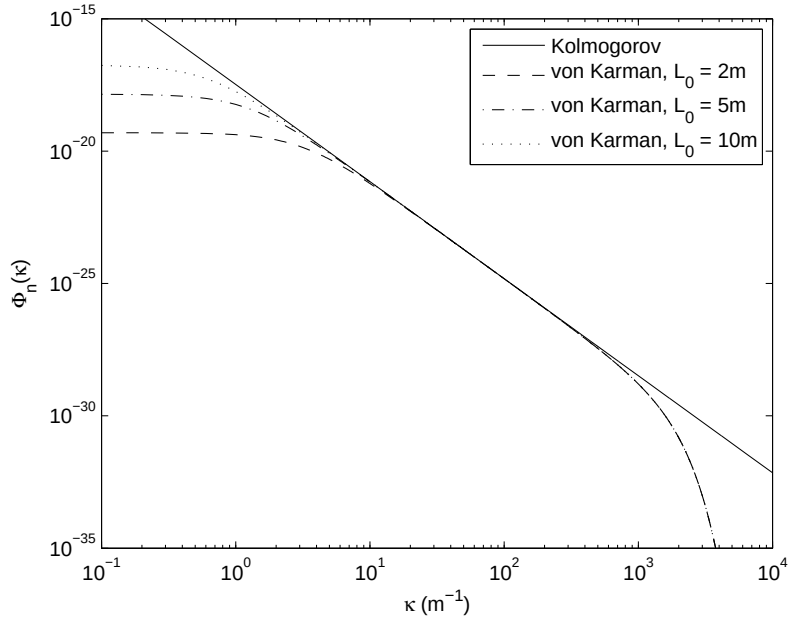

Figure 1.1: Kolmogorov and von Kármán turbulence spectral models. $C_n^2 = 10^{-15}\,\mathrm{m}^{-2/3}$ with $l_0 = 5$ mm, and $L_0 = 2, 5$, and 10 m for the von Kármán model.

tween each subsequent data point collection of the optical power within the framework of the simulation, the turbulence along the propagation path was assumed independent from the previous data point collection. However, in reality atmospheric turbulence does not change so rapidly. We make use of this fact in the study outlined in chapter 4 in which we are interested in the temporal power spectral density of these optical power fluctuations.

Taylor's hypothesis of "frozen" turbulence states that temporal variations in an atmospheric quantity measured at a point are caused by the uniform motion of the atmosphere past the point and that internal motions of the atmosphere can be neglected [4]. This means that in the atmosphere there are two time scales with which to be concerned. The first time scale is due to the perpendicular motion across the propagation path of the laser beam.

This time scale can be estimated by $L_0/V_\perp$, where $V_\perp$ is the mean wind speed transverse to the propagation path and is typically on the order of 1 s [2]. The other time scale is due to the evolution of the turbulent eddies described above and is typically on the order of 10 s. This means that we can consider a measured quantity in the atmosphere such as index of refraction to be relatively unchanging for a short period of time. This idea can be represented mathematically by the expression

$$s(\vec{r}, t+\tau) = s(\vec{r} - V_\perp \tau, t), \tag{1.11}$$

for any time t. In the above expression Eq. 1.11, s represents any atmospheric turbulence variable of interest, and $\tau = t_2 - t_1$ is a time difference.

1.2 Free Space Optical Communication

Now that a foundation has been laid for an understanding of turbulence within the atmosphere and the forces that influence it, an overview can be given in this section of how turbulence within the channel of a laser communication link affects the received power. This section begins with a general review of communication systems in section 1.2.1 then transitions into a brief description of optical communication through atmospheric turbulence given in section 1.2.2.

1.2.1 Brief Review of Communication Systems

Communication is the transmission of information through some medium and the reception of that information. There are three basic components that comprise all communication systems. They are the transmitter, the channel, and the receiver.

The transmitter is comprised of an encoder and a modulator. Its function is to encode the information bits, often with an error-correction code, and convey that information with an electrical signal or an optical/infrared wave. This dissertation is only concerned with transmission via optical waves.

The channel is the medium through which the information is transmitted. It includes effects such as distortion, additive noise, and interference [2]. The medium may be a transmission line, such as fiber optic, free space, or the atmosphere. This dissertation is concerned with transmission through the atmospheric channel.

The receiver is comprised of a demodulator and a decoder. Its function is to capture the signal sent through the channel and extract the information from the signal essentially in reverse order of the transmitter process.

1.2.2 Optical Communication Through Atmospheric Turbulence

Free space optical (FSO) communication is a rapidly growing field in wireless communications because of the high bandwidths and the ability to transfer high data-rates of information that is possible at optical wavelengths [2]. FSO systems are capable of transmitting several gigabits of information per second (GBPS) along line of sight paths through the turbulent atmosphere. Other attractive attributes of FSO communication systems include lower mass, power, and volume compared with conventional radio frequency (RF) systems, and a narrow-beam with high gain, which means a more secure channel [2].

Laser wavelengths for use in FSO systems are typically 850 and 1550 nm [2]. The FSO systems simulated for the studies within this dissertation use a laser wavelength of 1550 nm. The carrier frequency utilized in FSO systems are typically on the order of 10^{14} Hz and is selected from the optical spectrum, which extends from approximately $10^{-2}\,\mu$m to $10^{2}\,\mu$m including the ultraviolet, visible, and infrared wave bands [2].

FSO communication systems have some serious disadvantages that come about due to the smaller wavelengths compared to RF systems [2]. These include acquistion and pointing difficulties due to the high directivity of the beam and propagation problems caused by atmospheric conditions such as rain, snow, fog, haze, and turbulence.

This dissertation is concerned with the distorting effects that atmospheric turbulence can have on a laser beam. Turbulence, which is a result of temperature variations in the atmo-

sphere causes power losses in the FSO link from spreading of the beam spot radius beyond that due to diffraction alone, and from spatial and temporal fluctuations in the laser beam at the receiver known as scintillation. Power losses in the FSO link can eventually lead to fading of the received signal below a prescribed threshold [2].

1.3 Approach

In order to predict the fading in a FSO communication link caused by atmospheric turbulence, a reliable and accurate mathematical model for the probability density function (PDF) of the received optical power is essential. It is customary to assume that the PDF of irradiance in the plane of the photo detector comes from the same family as those in the pupil plane of the receiver [2]. This statement is equivalent to saying that the PDF of the received power is from the same family as the PDF of irradiance at a point in the pupil plane of the receiver [2]. Therefore it follows that in order to determine the best fitting theoretical model for the distribution of optical power, one may choose from among several PDF models that have been put forth in the literature over the years, whether for point apertures or finite apertures. These include log-normal, exponential, K-distribution, log-normally modulated exponential, log-normally modulated Rician (also known as Beckman's PDF) and gamma-gamma.

This dissertation characterizes the PDF of the received optical power collected from many

realizations of an uncompensated Gaussian laser beam. This is accomplished by comparing the PDF of the simulated data to theoretical lognormal and gamma-gamma PDF models. The lognormal and gamma-gamma PDF models are two of the most widely used PDF models in the literature [1, 5]. A wide range of scintillation conditions involving several link distances and turbulence strengths were simulated for the studies involving the PDF. We are interested in how the PDF changes as the receiver aperture is increased for a given link distance, or if the link distance is increased, or if the turbulence strength is increased while varying the former parameters. Simulations were run to model an uncompensated Gaussian laser beam propagating through atmospheric turbulence ranging from $C_n^2 = 1 \times 10^{-18}\,\mathrm{m}^{-2/3}$ to $C_n^2 = 1 \times 10^{-15}\,\mathrm{m}^{-2/3}$ with link distances of 50 km, 75 km, and 100 km. The receiver aperture sizes were determined based upon previous PDF theory suggesting that the PDF changes depending upon scintillation conditions and the size of the aperture relative to the coherence radius ρ_0.

In addition to characterizing the PDF of the received power from an uncompensated Gaussian laser beam, this research includes characterizing the PDF of a Gaussian laser beam that has been precompensated using adaptive optics (AO) before being transmitted through the atmospheric channel. We are interested in how the PDF changes while varying the parameters mentioned in the previous paragraph but also how the PDF is affected if the complexity of the AO is increased. Specifically, if we increase the number of subapertures in the WFS from low-order (12 subapertures) to medium-order (24 subapertures) to high-order (52 subapertures). Simulations were run to model a FSO communication link similar to the

uncompensated cases except using AO and propagating through channels with distances of 10 km and 20 km, while keeping the turbulence strength fixed at $C_n^2 = 1 \times 10^{-15}\,\mathrm{m}^{-2/3}$.

Finally, this research examined the power spectral density (PSD) of temporally changing optical power fluctuations at the receiver of a FSO communications link. We are interested in how the coherence time of the communication link changes if we increase the link distance or if we increase the receiver aperture size. We investigate the temporal PSD of the received power from a truncated Gaussian beam after propagation through the turbulent channel since this is a more realistic case compared to infinite beam cases. Simulations were run to model a Gaussian laser beam propagating through atmospheric turbulence as in the previous studies but in this case with a $6\,\mathrm{m/s}$ cross-wind velocity $V\perp$ along a 100 km path. The optical power was collected at 25 km intervals by a series of receiver apertures of various diameters from 0.68 cm to 150 cm. The PSD was calculated from the time-series of the data for each aperture, from which the correlation function was obtained. The coherence time was then measured as the half-width of the correlation function at the e^{-1} value.

In addition to the simulations run to obtain the PSD, data was collected experimentally from the receiver of a communication link located at Michigan Technological University in Houghton, Michigan. Optical power was collected at the receiver of a 3.1 km communication link from a 13 mW semiconductor laser operating at a wavelength of 808 nm. The amount of laser light entering the pupil was varied using a foam stop with cutouts in front

of the receiver. The receiver aperture diameters ranged from 9 cm to 13.26 cm. The goal of this portion of the study was to see whether the results observed in the simulation would be observed experimentally. The experimental results, although not directly comparable to the simulation results due to differences in link distance, receiver aperture size, and laser wavelength, nevertheless demonstrate the trend of increasing coherence time with aperture size shown in the simulation results.

Sections 1.1 and 1.2 contain some background theory germane to the topics covered within this dissertation. However, more detailed background sections can be found within chapters 2 through 4 that is pertinent for each specific topic.

1.4 Summary of Key Results

The main result found in the study involving the PDF of an uncompensated Gaussian laser beam found in chapter 2 is that the gamma-gamma PDF model provides a good fit to the distribution of optical power for all aperture sizes studied in the weak through moderate scintillation regions. This result is important since previous theory [6, 1] was that in weak scintillation, characterized by the Rytov variance $\sigma_R^2 = 1.23 C_n^2 k^{7/6} L^{11/6}$, where $\sigma_R^2 < 1$ the PDF should be lognormal for apertures larger than the first Fresnel zone $\sqrt{L/k}$, where L is the link distance and k is the wavenumber. In very weak scintillation, $\sigma_R^2 << 1$ both lognormal and gamma-gamma PDF models provide a good fit to the distribution, but as the

scintillation is increased the PDF quickly begins to widen and become better modeled by the gamma-gamma PDF. This trend continues through the moderate scintillation regime up to $\sigma_R^2 \cong 5$. In strong scintillation $\sigma_R^2 > 5$ the previous theory [1] holds, where the gamma-gamma PDF model provides a good fit to the distribution for apertures significantly smaller than ρ_0 and the lognormal PDF model is a better fit to the distribution for apertures equal in size or larger than ρ_0.

The main result found in the study involving the PDF of the laser beam compensated using AO detailed in chapter 3 is that any increase in complexity of the AO beyond a low-order will not significantly affect the PDF of the received power nor does it improve the bit-error rate (BER) in the moderate scintillation regime. The BER results were much more pronounced for the 10 km link compared with the 20 km link. This is to be expected since the degree of scintillation was higher for the longer link distance. It was also found that the PDF remained gamma-gamma distributed after AO compensation as it was before compensation in the moderate scintillation regime. The PDF results are in line with those shown by Tyson [7], however Tyson's study only incorporated tip/tilt AO correction. These results incorporate low-order, medium-order, and high-order degrees of AO complexity. The BER results for the 10 km link are relatively in line with those by Tyson [8] for a signal-to-noise ratio (SNR) of 21, however the BER for only the 4.62 cm diameter aperture was investigated in this study whereas Tyson used a 10 cm diameter aperture.

It was found that the coherence times in the PSD study found in chapter 4 increased as the

aperture size was increased for a given link distance. This trend was verified in the experimental data collection as well. Also, the coherence times were found to increase for all finite aperture sizes as the link distance was increased in the simulations. This is likely due to an increasing speckle size in the pupil of the receiver as the link distance is increased. A larger speckle is directly proportional to an increase in spatial coherence of an optical wave. This would account for the increase in the coherence time as link distance is increased. We examined the temporal PSD of the received power from a truncated Gaussian beam after propagation through the turbulent channel since this is a more realistic case compared to infinite beam cases. To our knowledge this is the only study involving the coherence time of the atmospheric channel using numerical simulations at these link distances. We investigate the temporal PSD of the received power from a truncated Gaussian beam after propagation through the turbulent channel since this is a more realistic case compared to infinite beam cases. These results, although not directly comparable, due mainly to the longer propagation distances in this study, are nevertheless in line with those predicted by Brookner [9] for a much shorter link.

1.5 Organization of Dissertation

The remainder of this dissertation is organized as follows. In Chapter 2, the characterization of the probability distribution of optical power for an uncompensated Gaussian laser beam in a free space optical communication link is given, In Chapter 3, the characterization of the

probability distribution of power for a Gaussian laser beam pre-compensated using adaptive optics in a free space optical communication link is given, In Chapter 4, the temporal power spectral density of optical power and coherence times are given for simulation and experimental data. In Chapter 5, conclusions are given.

Chapter 2

Probability density of aperture averaged irradiance fluctuations for long range free space optical communication links

2.1 Introduction

Free space optical (FSO) communication links can experience extreme signal degradation due to atmospheric turbulence induced spatial and temporal irradiance fluctuations (scintillation) in the laser wavefront. In addition, turbulence can cause the laser beam centroid to wander resulting in power fading, and sometimes complete loss of the signal. Spreading of

the laser beam and jitter are also artifacts of atmospheric turbulence.

To accurately predict the signal fading that occurs in a laser communication system and to get a true picture of how this affects crucial performance parameters like bit error rate (BER) it is important to analyze the probability density function (PDF) of the aperture averaged irradiance fluctuations at the receiver plane of the system. In addition, it is desirable to find a theoretical distribution that accurately models these fluctuations in the receiver plane under all propagation conditions. The PDF of the irradiance fluctuations at the receiver plane of a FSO link for both point size and finite size apertures has been studied extensively in the literature [10, 11, 6, 12, 13, 14, 15, 7, 1, 16, 17, 18, 19]. Many theoretical PDFs have therefore been proposed as viable models for differing scintillation strength regions from weak to saturated. These include lognormal, exponential, K-distribution, log-normally modulated exponential, log-normally modulated Rician (also known as Beckman's PDF) and gamma-gamma. Perhaps the two most widely accepted PDF models are lognormal and gamma-gamma. Some recent studies have been conducted comparing the irradiance PDF for FSO channels to the gamma-gamma PDF model [14, 15, 7, 1]. One study directly relevant to ours by Vetelino et al. [1] compared the lognormal and gamma-gamma probability distributions of irradiance to simulated and experimentally collected aperture averaged irradiance data for a Gaussian beam propagating through atmospheric turbulence in the moderate-to-strong turbulence regime. They concluded that for apertures that are significantly smaller than the atmospheric spatial coherence radius ρ_0, the irradiance fluctuations are gamma-gamma distributed, while for apertures with diameters of equal size or

greater than ρ_0, the irradiance fluctuations are lognormal.

In this study, the lognormal and gamma-gamma PDFs for irradiance fluctuation data are considered and comparisons are made with PDFs derived from numerical propagation simulations. A spatially truncated Gaussian beam is assumed to propagate through homogeneous and isotropic atmospheric turbulence. Propagation distances of 50 km, 75 km, and 100 km are considered and particular attention is placed on observing the changes in the fluctuation distributions as the receiver aperture size is increased from a point-like aperture to larger than the turbulence coherence radius. In addition, the relationship between the PDF form, the receiving aperture size, and the coherence size are explored in detail.

Results confirm that in the weak scintillation regime, irradiance fluctuations collected by apertures that are larger than the Fresnel zone are lognormal in their distribution. However, our results show that the gamma-gamma PDF also provides a good fit to the simulation data for all aperture sizes in the weak scintillation regime. In strong scintillation, irradiance fluctuations collected by apertures significantly smaller than the coherence radius are gamma-gamma distributed and irradiance fluctuation data collected by apertures larger than or equal in size to the coherence radius have a lognormal distribution. However, in moderate scintillation, our results indicate that the irradiance fluctuations are gamma-gamma distributed for apertures of all sizes studied from point-like to $3\rho_0/2$. This is interesting since from previous results [1] we expected the PDF to be lognormal for apertures larger than the coherence radius in moderate scintillation.

The remainder of this chapter is organized as follows. In section two, the theory associated with modeling irradiance fluctuations using the lognormal and gamma-gamma probability distributions with aperture averaging is presented. In addition, results from a previous work that is directly relevant by Vetelino et al. [1] are summarized. In section three, a detailed description of the wave-optics simulation is given. In section four, the results are presented and the effects of aperture averaging on the form of the simulated probability density function are discussed. Also in section four, the bit-error rate (BER) for on-off keying (OOK) modulation for the optical channel is calculated using the measured simulation data PDF and compared to the BERs using the theoretical gamma-gamma and lognormal PDFs. In section five, the conclusions are given.

2.2 Background

2.2.1 Probability Density Function Models

Several PDFs have been proposed as a model for the distribution function for the irradiance fluctuations. We now present the two PDF models that have found the widest acceptance in the literature, the gamma-gamma PDF and the lognormal PDF.

2.2.1.1 Gamma-Gamma Probability Density Function

The gamma-gamma distribution has been supported by simulation data as a possible model for irradiance fluctuations in weak, moderate and strong scintillation [14]. The aperture averaged irradiance at the receiver plane can be defined as $I = XY$, where X arises from large scale turbulent eddies and Y arises from statistically independent small scale turbulent eddies [15]. Here X and Y are random processes in which one process modulates the other and can generally be described as a multiple stochastic process. The gamma-gamma distribution is defined by [2]

$$p(I) = \frac{2(\alpha\beta)^{(\alpha+\beta)/2}}{\Gamma(\alpha)\Gamma(\beta)I}(I)^{(\alpha+\beta)/2}K_{\alpha-\beta}(2\sqrt{\alpha\beta I}), \qquad I > 0, \tag{2.1}$$

where α and β are parameters of the gamma-gamma distribution and represent the effects of the large and small spatial scale scintillation respectively, $\Gamma(x)$ is the gamma function, $K_{\xi}(\nu)$ is a modified Bessel function of the 2^{nd} kind, and I is the aperture averaged irradiance normalized by it's mean. The parameters α and β are specifically defined as $\alpha = 1/\sigma_X^2$ and $\beta = 1/\sigma_Y^2$. σ_X^2 and σ_Y^2 are the variances of the large and small spatial scale integrated irradiance fluctuations [2] and are given as $\sigma_X^2 = \exp(\sigma_{\ln X}^2) - 1$ and $\sigma_Y^2 = \exp(\sigma_{\ln Y}^2) - 1$, where $\sigma_{\ln X}^2$ and $\sigma_{\ln Y}^2$ are the variances of the large and small spatial scale log irradiance fluctuations [2]. Andrews and Phillips [2] give expressions for $\sigma_{\ln X}^2$ and $\sigma_{\ln Y}^2$ for a Gaussian-beam wave where the receiver aperture diameter is taken into account.

2.2.1.2 Lognormal Probability Density Function

The lognormal PDF is generally accepted as a representative model for irradiance fluctuations in the weak scintillation regime. This study uses the expression for the lognormal distribution found in [1]

$$p(I) = \frac{1}{I\sqrt{2\pi\sigma_{lnI}^2}} \exp\left\{ -\frac{\left[\ln(I) + \frac{1}{2}\sigma_{\ln I}^2\right]^2}{2\sigma_{\ln I}^2} \right\}, \qquad I > 0, \tag{2.2}$$

where $\sigma_{\ln I}^2$ is the log-irradiance variance. In the weak scintillation regime the scintillation index σ_I^2 is approximately equal to $\sigma_{\ln I}^2$, however in moderate-to-strong scintillation regimes this approximation no longer holds and the exact relation given in [1]

$$\sigma_{\ln I}^2 = \ln\left(\sigma_I^2 + 1\right), \tag{2.3}$$

must be used, as it is always true. For consistency, $\sigma_{\ln I}^2$ is used in the lognormal PDF for all simulations in this study.

2.2.2 Scintillation

The Rytov variance given by $\sigma_R^2 = 1.23 C_n^2 k^{7/6} L^{11/6}$, where k is the optical wave number defined as $k = 2\pi/\lambda$, and L is the propagation distance in meters represents the variance of the irradiance fluctuations of an infinite plane wave [2] that has propagated a distance

L through atmospheric turbulence characterized by the structure constant of the turbulence C_n^2. The Rytov variance is also considered a measure of optical turbulence strength when extended to the strong fluctuation regimes [15]. Consequently, the convention for characterizing the strength of scintillations found in Ref. [2] has been adopted here. Generally speaking, weak scintillation refers to $\sigma_R^2 < 1$, while strong scintillation refers to $\sigma_R^2 > 1$, and moderate scintillation is represented by $\sigma_R^2 \approx 1$ [2]. In the weak scintillation regime the Rytov variance $\sigma_R^2 \cong \sigma_I^2$, where σ_I^2 is the normalized irradiance variance, also referred to as the scintillation index and is defined as

$$\sigma_I^2 = \frac{\langle I^2 \rangle - \langle I \rangle^2}{\langle I \rangle^2}, \tag{2.4}$$

where I is the irradiance measured at the receiver plane.

In order to analyze the fluctuation statistics of a laser communication signal it is important to account for the fact that real receivers have finite-sized apertures. Accounting for the effects of receiving a spatially fluctuating beam with a finite-sized aperture is referred to as "aperture averaging" in the literature [1, 20, 21, 16, 17, 18, 19]. One method of reducing the fluctuations in the irradiance at the receiver plane is by increasing the size of the aperture. Using large apertures at the receiver plane reduces these fluctuations and therefore reduces σ_I^2 by averaging over the surface of the aperture [19]. Ref. [2] contains scintillation theory for Gaussian laser beam waves for finite-sized receiver apertures and is utilized in this study.

From the Kolmogorov theory, the dimensions of the turbulent eddies found in the atmosphere are bounded by the inner scale of turbulence l_0, which is the smallest size eddy and the outer scale of turbulence L_0, which is the largest size eddy that obeys Kolmogorov's power law theory. The range of these turbulent eddy dimensions are from a few millimeters for the inner scale l_0 to many tens of meters for the outer scale L_0 [3]. In this study it is assumed that, $l_0 = 0$ and $L_0 = \infty$. It has been shown [1] that the gamma-gamma distribution accurately models the aperture averaged irradiance fluctuations for apertures significantly smaller than the turbulence spatial coherence radius ρ_0, while the lognormal distribution can be used to model fluctuations for apertures larger than or equal in size to the coherence radius ρ_0 in moderate to strong turbulence. The expression for the spatial coherence radius for a Gaussian beam wave can be found in [2].

2.2.3 Summary of Recent Relevant Scintillation Study

Recently an experiment involving the propagation of a $1.55\,\mu$m wavelength laser was conducted by Vetelino et al. in South Australia. The laser beam was collected by three apertures of diameter 1 mm, 5 mm, and 13 mm simultaneously. Here is a summary of the results from their paper that is directly relevant to this study [1].

Vetelino et al. [1] compared the lognormal and gamma-gamma probability distributions of irradiance to simulated and experimentally collected aperture averaged irradiance data for

a Gaussian beam propagating 1500 meters through atmospheric turbulence along a horizontal path in the moderate-to-strong turbulence regime. They concluded that for apertures that are significantly smaller than the coherence radius ρ_0, the irradiance fluctuations are gamma-gamma distributed. In the gamma-gamma PDF model the large and small scale fluctuations are assumed to be gamma distributed [2]. However, Vetelino et al. tried unsuccessfully to fit a gamma function to the simulation data. Their results indicated that large scale fluctuations do not appear to be gamma distributed. In addition, their results indicated that for apertures larger than or equal in size to the coherence radius ρ_0, the irradiance fluctuations are log-normally distributed in moderate to strong turbulence ($\sigma_R^2 = 2.7$ and $\sigma_R^2 = 19.2$ in their study). A comparison to their simulation results can be found at the end of the next section.

2.3 Simulation

2.3.1 Simulation Description

A numerical wave-optics simulation was developed to expand on the findings found in [1] and observe how the PDFs behave under different propagation lengths and turbulence strengths, which led to higher σ_R^2 values than were studied in [1]. The parameters used in the simulation to recreate the simulation plots of Vetelino et al. had to be modified for long

Table 2.1: Table 1. Numerical simulation parameters

C_n^2	L(km)	N_{Grid}	N_{Steps}	Δx(mm)	ρ_0(m)	l_s(m)	σ_R^2(L)	σ_R^2(Δz)
1E-18	50	1024	5	5	1.6100	0.0077	0.026	1.36E-3
1E-18	75	1024	5	5	1.2644	0.0146	0.054	2.85E-3
1E-18	100	1024	5	5	1.0646	0.0232	0.092	4.83E-3
1E-17	50	1024	5	5	0.4044	0.0305	0.259	0.0136
1E-17	75	1024	5	5	0.3176	0.0583	0.545	0.0285
1E-17	100	1024	5	5	0.2674	0.0922	0.924	0.0483
1E-16	50	1024	10	5	0.1016	0.1214	2.593	0.0381
1E-16	75	1024	10	5	0.0798	0.2319	5.453	0.0800
1E-16	100	1024	12	5	0.0672	0.3672	9.241	0.0971
1E-15	50	1024	25	5	0.0255	0.4834	25.932	0.0709
1E-15	75	2048	35	5	0.0200	0.9232	54.535	0.0805
1E-15	100	2048	42	5	0.0169	1.4620	92.412	0.0976

propagation distances and thus stronger scintillation regimes. Careful attention was placed on the development of the simulation parameters and for this reason simulation guidelines presented by Rao [22] and Belmonte [23] were followed closely. A list of the relevant parameters used in the simulations is presented in Table 1.

The turbulence strengths used in this study were $C_n^2 = 1 \times 10^{-18}\,\mathrm{m}^{-2/3}$ through $C_n^2 = 1 \times 10^{-15}\,\mathrm{m}^{-2/3}$ as shown in the first column of Table 1. A total of 30,000 data points were obtained to create the PDFs. The normalized irradiance for each different turbulence and propagation distance case was obtained by averaging the irradiance values at the receiver plane over the circular aperture then they were divided by the mean irradiance value in the aperture. The normalized log irradiance was obtained by taking the natural log of the normalized irradiance for each case. The PDF was simulated by sorting each of the normalized log irradiance values into separate bins of equal width then the number of values

in each bin was divided by the bin width and the total number of data points collected for each case. 100 bins were used to create the histograms for all aperture sizes for the $C_n^2 = 1 \times 10^{-17}\,\mathrm{m}^{-2/3}$ through $C_n^2 = 1 \times 10^{-15}\,\mathrm{m}^{-2/3}$ turbulence strength cases. However, for the $C_n^2 = 1 \times 10^{-18}\,\mathrm{m}^{-2/3}$ turbulence strength in order to make the PDFs easier to interpret, 500 bins were used to create the histograms for the point-like and $\rho_0/2$ aperture size cases and 1000 bins were used to create the histograms for the ρ_0 and $3\rho_0/2$ aperture size cases.

The model for an initially collimated Gaussian beam is

$$U(x,y,z) = A_0 \frac{W_0}{W(z)} \exp\left[-\frac{(x+y)^2}{W^2(z)}\right] \times P(x,y), \tag{2.5}$$

where A_0 represents the peak amplitude of the outgoing beam, taken to be unity. W_0 and $W(z)$ are the beam waists at the transmitter and at a propagation distance z away respectively. $P(x,y)$ represents the finite pupil, where $P(x,y) = 1$ inside the pupil and $P(x,y) = 0$ outside the pupil. The initial beam radius $W_0 = 3.54$ cm is calculated from the transmitter aperture diameter d by the expression $W_0 = d/2\sqrt{2}$ given in Ref. [20], where d was chosen to be 10 cm. The beam wavelength was $\lambda = 1.55$ μm, a widely used wavelength in laser communication. The laser beam was then propagated through 50 km, 75 km, and 100 km of simulated atmospheric turbulence and the signal fluctuation data was collected simultaneously by four separate apertures. The diameter of each aperture was chosen to be a point-like aperture, $\rho_0/2$, ρ_0, and $3\rho_0/2$ respectively, where the numerical values of ρ_0

for each case are presented in column 6 of Table 1. The point-like aperture was simulated by a single square pixel located in the center of the propagation grid at the receiver plane. The area of the square pixel is $25\,\mathrm{mm}^2$, which corresponds to a circular aperture with a diameter of 5.64 mm. The remaining aperture diameters were calculated separately for each simulation based on the propagation length and turbulence strength.

The laser simulation was accomplished by propagating the complex field through homogeneous and isotropic atmospheric turbulence using a Fresnel propagator from a Matlab toolbox AOTools [24]. The atmosphere was simulated by dividing the total propagation distance into several smaller distances, each followed by a randomly generated phase screen. Each phase screen was comprised of either 1024×1024 grid points for turbulence strengths $C_n^2 = 1 \times 10^{-18}\,\mathrm{m}^{-2/3}$ through $C_n^2 = 1 \times 10^{-16}\,\mathrm{m}^{-2/3}$ and the 50 km case for $C_n^2 = 1 \times 10^{-15}\,\mathrm{m}^{-2/3}$ or 2048×2048 grid points for the longer propagation distances of 75 km and 100 km through turbulence with strength $C_n^2 = 1 \times 10^{-15}\,\mathrm{m}^{-2/3}$. The sample spacing was chosen to be 5 mm between each grid point for all cases of scintillation, making the edge dimension of each physical grid size 5.12 m or 10.24 m, respectively. The Kolmogorov turbulence spectrum phase screen generator by a widely available software tool from a Matlab toolbox AOTools [24] was used and inner and outer scale effects were ignored. The Rytov variance was calculated for the total propagation length for each turbulence strength. Next, the number of phase screens was calculated so that there would be no more than 10 % of the total Rytov variance between each propagation step Δz and the scintillation index per propagation step would be less than 0.1 as pointed out by Rao [22].

Both the Rytov variance for the total propagation length σ_R^2(L) and the Rytov variance per propagation step $\sigma_R^2(\Delta z)$ are presented in columns 8 and 9 respectively of Table 1. The first and last phase screens were placed half the distance $\Delta z/2$ of each propagation step from the transmitter and receiver apertures respectively. The sample spacing Δx between each grid point was set at 5 mm for all cases. However, this was checked to ensure that it complies with the sample spacing range given by Rao [22].

The inner and outer scale effects were ignored in the theoretical expression for the log-irradiance variance σ_{lnI}^2 in the lognormal PDF and as in [1] the scintillation index calculated directly from the simulated irradiance data did not match theory. As a result, it was necessary to determine σ_{lnI}^2 by using Eq. (2.3) and measuring the scintillation index directly from the simulation data. Also, the α and β parameters in the gamma-gamma distribution were obtained using a best fit to the simulation data as was done in [1], while maintaining the relationship between α, β and the scintillation index σ_I^2 given the equation

$$\sigma_I^2 = \left(1+\frac{1}{\alpha}\right)\left(1+\frac{1}{\beta}\right) - 1. \tag{2.6}$$

2.3.2 Comparison to Previous Simulation Results

Simulations using the same parameters as Vetelino et al. [1] were conducted in order to compare results and confirm the accuracy of our simulator. Results compare favorably

with Fig. 3 of [1]. Comparisons are made between simulation data and theoretical PDFs, which are displayed in Fig. 2.1. Each subplot represents the PDF of the normalized log irradiance $\ln(I)$ data collected for each of three different aperture sizes 1mm, 5mm, and 13mm diameters respectively and one of two different turbulence strengths ($C_n^2 = 6.47 \times 10^{-14}\, m^{-2/3}$ and $C_n^2 = 4.58 \times 10^{-13}\, m^{-2/3}$). As in [1], the 1 mm aperture was simulated with a single square pixel located at the optical axis. The pixel area was $2.47\,\text{mm}^2$, which corresponds to a circular aperture with a diameter of 1.8 mm. The simulation data was then compared to both of the theoretical PDFs within each subplot. The theoretical PDFs used in this comparison are the gamma-gamma PDF (solid curve) and lognormal PDF (dashed curve).

As shown in Fig. 2.1, the simulation data for $C_n^2 = 6.47 \times 10^{-14}\, m^{-2/3}$ for the 1.8 mm diameter and 5 mm diameter apertures fit a gamma-gamma well as in Fig. 3 of [1]. However, the simulation data for the 13 mm diameter aperture is close to a gamma-gamma distribution. Whereas Vetelino et al. found that their simulation data for the 13 mm diameter aperture and same turbulence strength fell between the gamma-gamma and lognormal distributions. However, it is worth noting that the simulation data for the 13 mm diameter aperture in this study more closely matched the experimental results for the same aperture size and turbulence strength found in Fig. 2 of [1]. The simulation data for the 1.8 mm diameter aperture for $C_n^2 = 4.58 \times 10^{-13}\, m^{-2/3}$ falls between the gamma-gamma and lognormal distribution while the 5 mm and 13 mm diameter aperture data more closely fits the lognormal distribution as did the simulation data in [1].

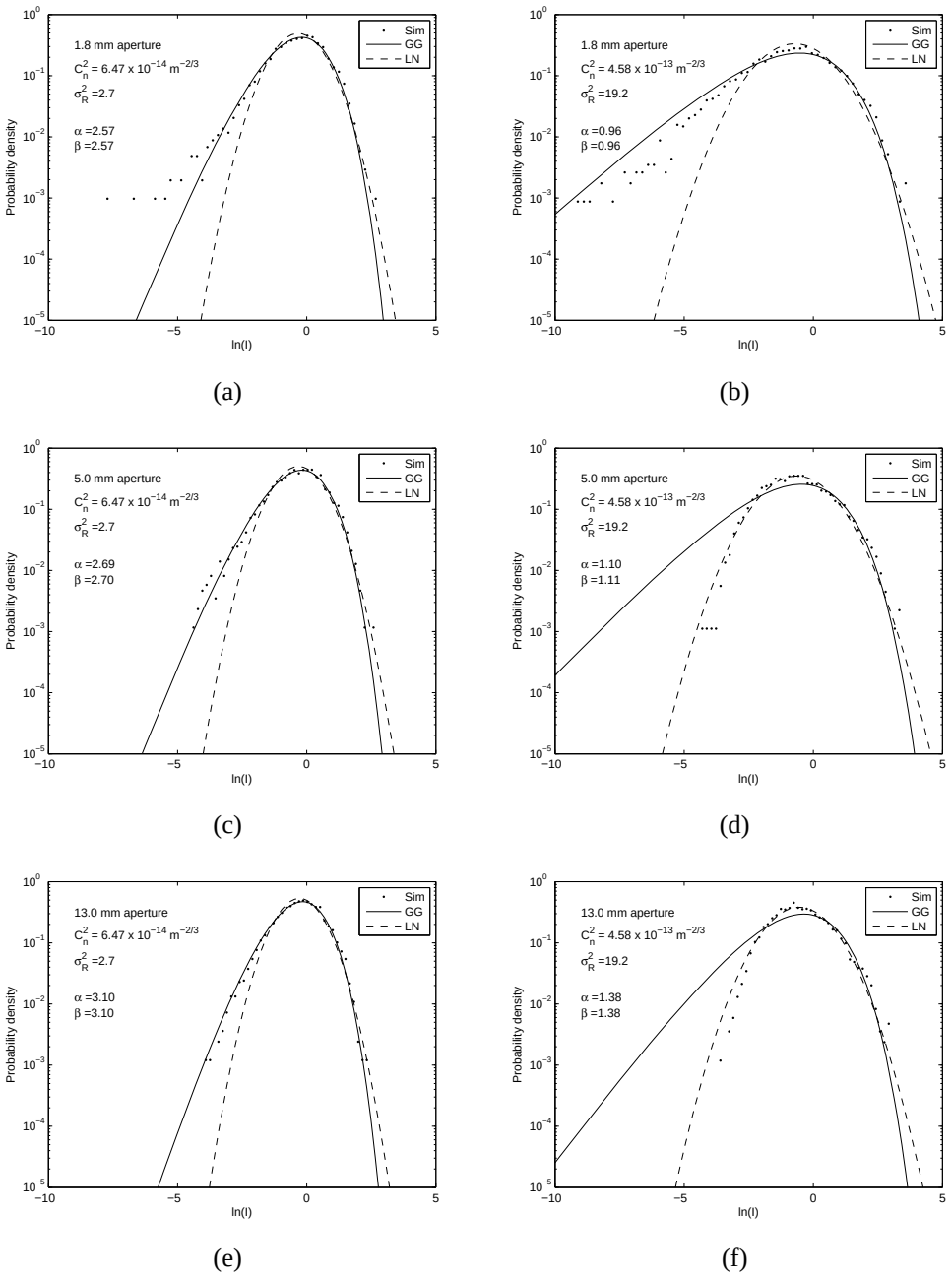

Figure 2.1: PDF of the normalized log irradiance $\ln(I)$ for the receiving apertures of diameter 1.8 mm, 5 mm, and 13 mm. Simulation results for two turbulence strengths $C_n^2 = 6.47 \times 10^{-14}\, m^{-2/3}$ and $C_n^2 = 4.58 \times 10^{-13}\, m^{-2/3}$ respectively are compared to gamma-gamma and lognormal PDFs. Results compare to Fig. 3 in [1].

2.4 Results

2.4.1 Probability Distribution

Comparisons are made between the theoretical and simulation derived PDFs, which are displayed in Figs. 2.2 through 2.9. Each subplot of a figure represents the PDF of the normalized log irradiance $\ln(I)$ data collected for each of four different diameter circular apertures. The aperture diameters used are point-like (5.64 mm), $\rho_0/2$, ρ_0, and $3\rho_0/2$, where ρ_0 is dependent on one of four different turbulence strengths $C_n^2 = 1 \times 10^{-18}\,\mathrm{m}^{-2/3}$, $C_n^2 = 1 \times 10^{-17}\,\mathrm{m}^{-2/3}$, $C_n^2 = 1 \times 10^{-16}\,\mathrm{m}^{-2/3}$, and $C_n^2 = 1 \times 10^{-15}\,\mathrm{m}^{-2/3}$ and one of three different propagation lengths 50 km, 75 km, and 100 km. The aperture sizes were chosen in this way to observe the form of the PDF of irradiance fluctuations on a point-like receiving aperture and on apertures as they transition in size through the turbulence coherence radius ρ_0 and beyond to an aperture larger than the coherence radius. The theoretical PDFs used in this comparison are the gamma-gamma PDF (solid curve) and lognormal PDF (dashed curve). The log irradiance variance $\sigma_{\ln I}^2$, which is related to the scintillation index by the relation given in Eq. (2.3) was used to calculate the lognormal PDF for all scintillation conditions. As in [1], the comparisons made between the irradiance fluctuation data PDF and the theoretical PDFs focuses on the tail (small irradiance values) since this is the portion of the PDF that is important for understanding the fade statistics of FSO communication systems.

Figs. 2.2 through 2.9 show comparisons between the simulation data and the gamma-gamma and lognormal distributions for each of the four turbulence strengths. Each figure represents the PDFs for two of the four aperture sizes and for all propagation lengths for a given turbulence strength. Each subplot represents the PDF of the normalized log irradiance $\ln(I)$ data collected for one of four different aperture sizes for a Gaussian laser beam after propagating through the atmosphere with a given turbulence strength C_n^2. The simulation data is presented on the same scale as the theoretical PDFs within each subplot to allow direct comparison. Due to the conclusions found in [1], it is expected that the form of the PDF will tend to be gamma-gamma distributed for apertures significantly smaller than the coherence radius in the moderate to strong fluctuation regime and migrate towards a lognormal distribution as the aperture size increases to equal to or larger than the coherence radius. For weak scintillation conditions, it is expected that the form of the PDF of the irradiance will be lognormal while the aperture is larger than the Fresnel zone [1, 17].

Figs. 2.2 and 2.3 show comparisons between the simulation data and the theoretical data for turbulence strength $C_n^2 = 1 \times 10^{-18}\,\mathrm{m}^{-2/3}$. The gamma-gamma distribution for large values of α and β, which are functions of the strength of scintillation and the aperture size is difficult to evaluate because of overflow and underflow calculation problems and thus no gamma-gamma model is present in several of the subplots. A direct form of the natural logarithm of the gamma function within the PDF is helpful for evaluation but no such form is available for the modified Bessel function K_ν. This phenomenon occurs when the scintillation strength is very weak ($\sigma_R^2 \leq 0.092$ in our simulations) as shown in Figs. 2.2(b)

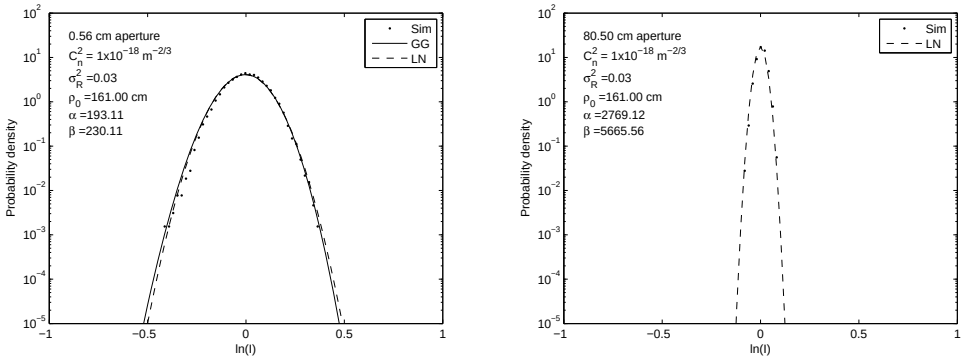

(a) 50 km

(b) 50 km

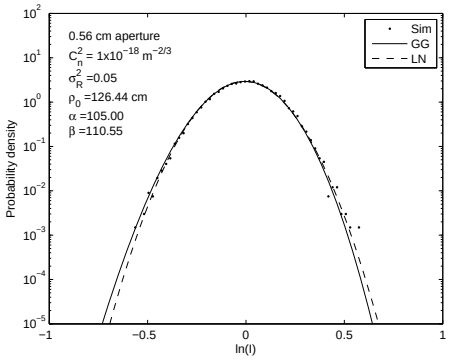

(c) 75 km

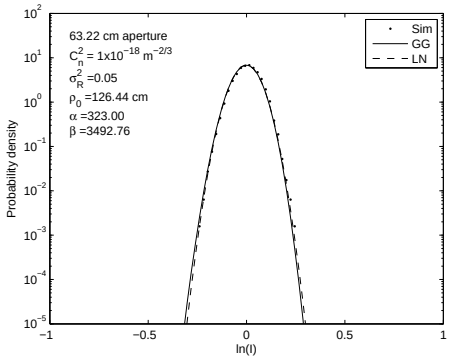

(d) 75 km

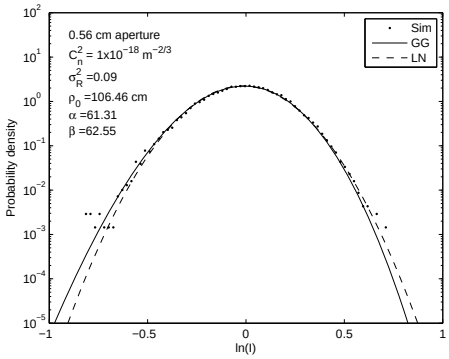

(e) 100 km

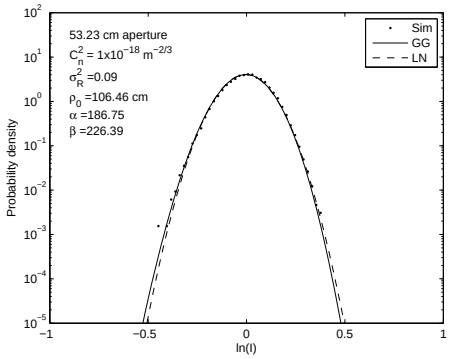

(f) 100 km

Figure 2.2: PDF of the normalized log irradiance $\ln(I)$ for the receiving apertures of diameter 5.6 mm ((a),(c),(e)) and $\rho_0/2$ ((b),(d),(f)). Simulation results for turbulence strength $C_n^2 = 1 \times 10^{-18}\ m^{-2/3}$ and propagation distance of 50 km, 75 km, and 100 km are compared to the gamma-gamma and lognormal PDF for each case.

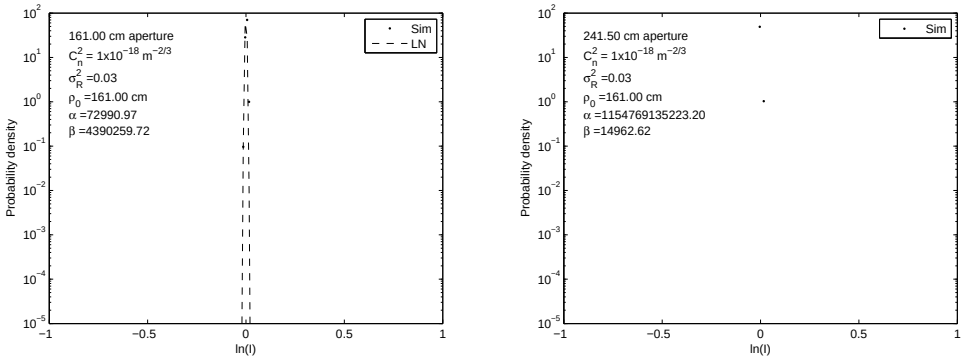

(a) 50 km

(b) 50 km

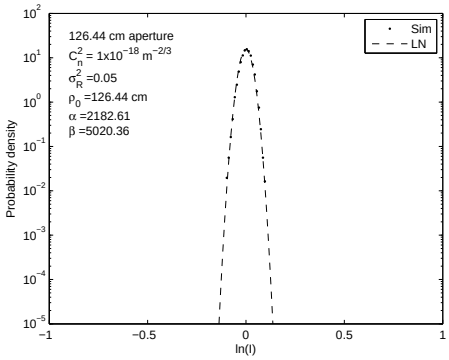

(c) 75 km

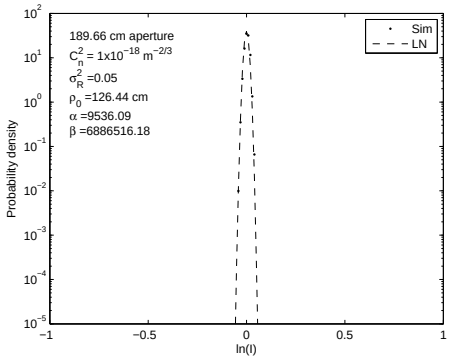

(d) 75 km

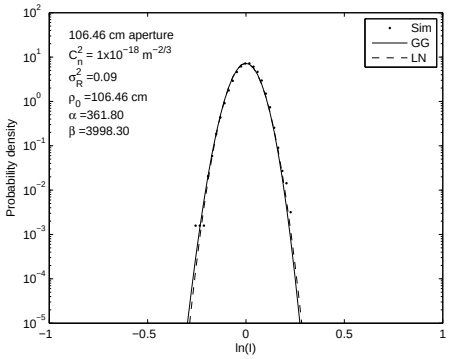

(e) 100 km

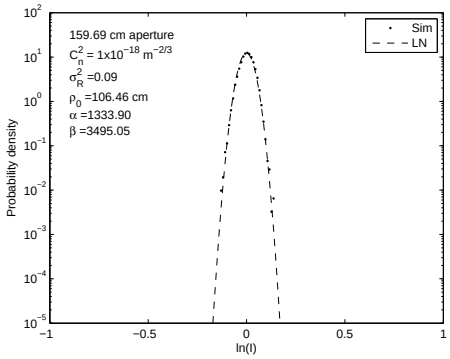

(f) 100 km

Figure 2.3: PDF of the normalized log irradiance $\ln(I)$ for the receiving apertures of diameter ρ_0 ((a),(c),(e)) and $3\rho_0/2$ ((b),(d),(f)). Simulation results for turbulence strength $C_n^2 = 1 \times 10^{-18}\ m^{-2/3}$ and propagation distance of 50 km, 75 km, and 100 km are compared to the gamma-gamma and lognormal PDF for each case.

and 2.3(a) to 2.3(d) and 2.3(f). It is therefore difficult to make a clear determination of the form of the PDF in these cases, but note that the gamma-gamma and lognormal curves are nearly identical for very small scintillation index values, so an argument could be made that either distribution in these cases provides a practical model for the PDF. The gamma-gamma PDF curves are present in the point-like aperture cases for all propagation lengths and for Fig. 2.2(a) both PDF models provide a good fit to the simulation data. For Figs. 2.2(c) and 2.2(e) the small irradiance values in the tail are not sufficiently resolved to be definite about the distribution, but again for practical purposes either PDF model appears to provide a good fit. For the $\rho_0/2$ aperture results of Fig. 2.2(f), the resolution in the tail again does not allow much differentiation between the distributions. Fig. 2.2(d) shows that both PDF models provide a good fit to the data and in Fig. 2.2(b) the lognormal PDF provides a good fit as is expected in weak scintillation for apertures larger than the Fresnel zone. Although the gamma-gamma curve is missing in Fig. 2.2(b), it should also provide a close fit to the data. This statement can also be applied to the remaining subfigures in figure 3 where the gamma-gamma curve is not present. In Fig. 2.3(b) neither model curve could be easily evaluated as the log-irradiance variance of the simulated data is nearly zero ($\sigma^2_{\ln I} = 4.4 \times 10^{-8}$) and, in fact, only two bins were filled in the histogram with a bin width of 0.02. Either model should be a good fit for these data although the conditions in this case are so benign that it is not much different than propagating through vacuum. Finally, in Fig. 2.3(e) generally both PDF models again provide a good fit. In general, differentiating the two PDF models for the weaker fluctuation cases in Figs. 2.2 and 2.3

would require considerably more sample values with higher resolution binning.

Figs. 2.4 and 2.5 show comparisons between the simulation data and the theoretical data for turbulence strength $C_n^2 = 1 \times 10^{-17}\,\mathrm{m}^{-2/3}$. In the point-like aperture cases (first column of Fig. 2.4) for the 50 km case with a Rytov variance of $\sigma_R^2 = 0.259$, the scintillation condition is still within the weak regime. In Fig. 2.4(a), close examination reveals that the PDF of the simulation data is between a gamma-gamma and a lognormal distribution. In Fig. 2.4(c) and 2.4(e) the distributions are clearly gamma-gamma. The remaining subfigures for the 50 km propagation distance case Figs. 2.4(b), 2.5(a), and 2.5(b) reveals that both PDF models provide good fits for the data. As the laser propagates through a stronger irradiance fluctuation regime $\sigma_R^2 = 0.55$ for the 75 km case and even more obviously in the 100 km case for $\sigma_R^2 = 0.92$ the simulated data PDFs demonstrate the gamma-gamma distribution for all aperture sizes. This is interesting, since as previously stated we expect that the irradiance fluctuation distribution should be lognormal for apertures larger than or equal to ρ_0 as shown in [1]. In Fig. 2.5(c) with aperture size equaling ρ_0 the data favors a gamma-gamma distribution. In Fig. 2.5(d) with aperture size equaling $3\rho_0/2$ close examination reveals that the data becomes gamma-gamma distributed in each case.

Figs. 2.6 and 2.7 show comparisons between the simulation data and the theoretical data for turbulence strength $C_n^2 = 1 \times 10^{-16}\,\mathrm{m}^{-2/3}$. In the 50 km case Figs. 2.6(a), 2.6(b), 2.7(a), and 2.7(b) with the Rytov variance $\sigma_R^2 = 2.59$, the simulated data PDFs for all aperture sizes still have a gamma-gamma distribution. At 75 km though $\sigma_R^2 = 5.45$, the simulated data

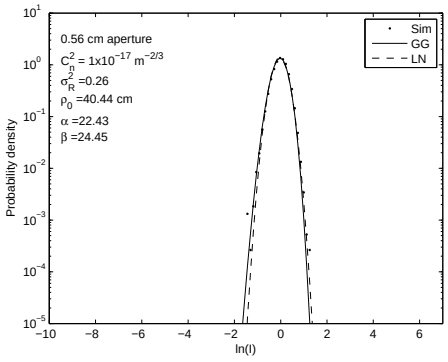

(a) 50 km

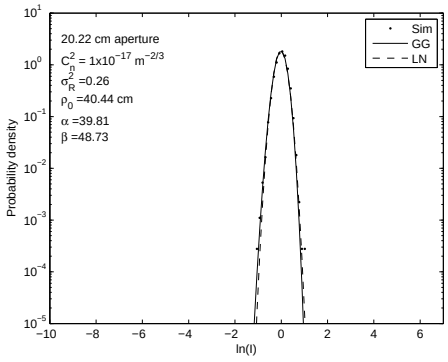

(b) 50 km

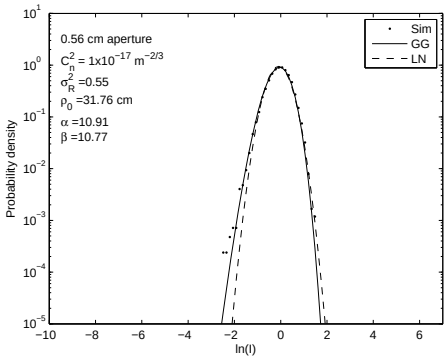

(c) 75 km

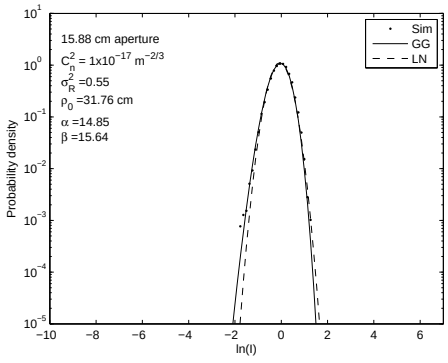

(d) 75 km

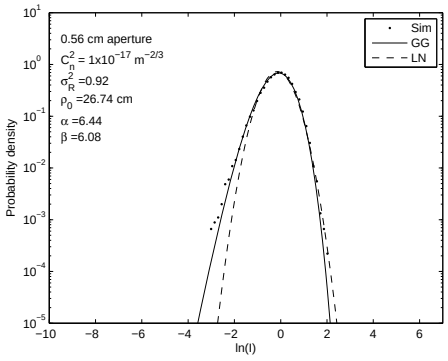

(e) 100 km

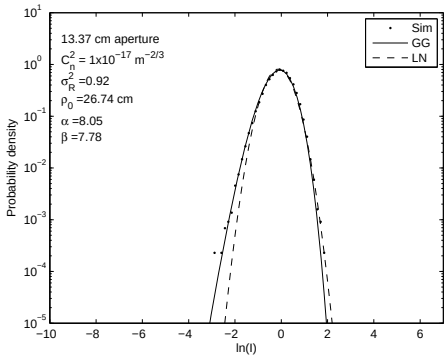

(f) 100 km

Figure 2.4: PDF of the normalized log irradiance $\ln(I)$ for the receiving apertures of diameter 5.6 mm ((a),(c),(e)) and $\rho_0/2$ ((b),(d),(f)). Simulation results for turbulence strength $C_n^2 = 1 \times 10^{-17}\ m^{-2/3}$ and propagation distance of 50 km, 75 km, and 100 km are compared to the gamma-gamma and lognormal PDF for each case.

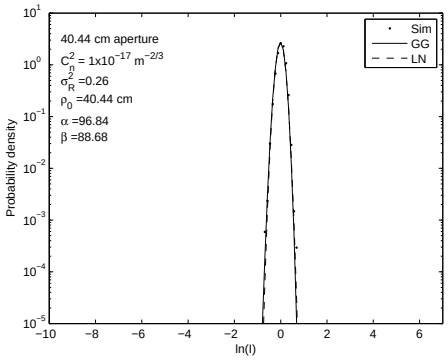

(a) 50 km

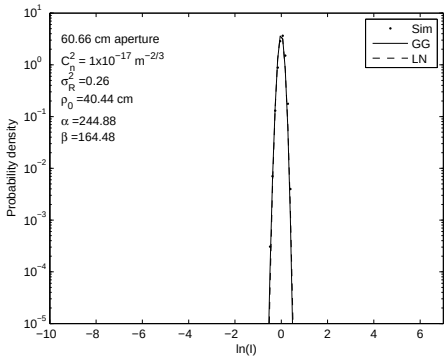

(b) 50 km

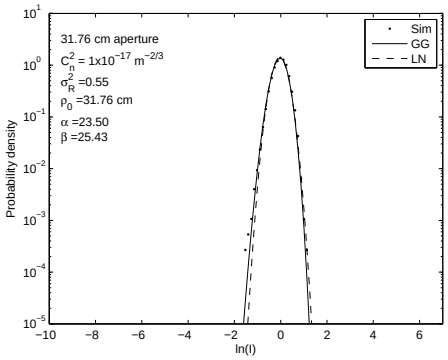

(c) 75 km

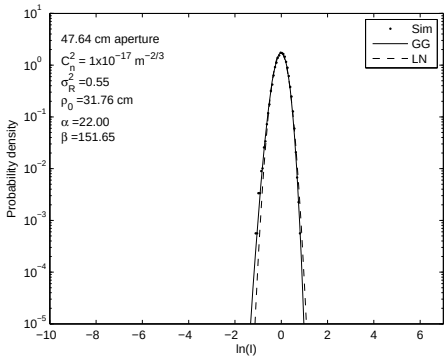

(d) 75 km

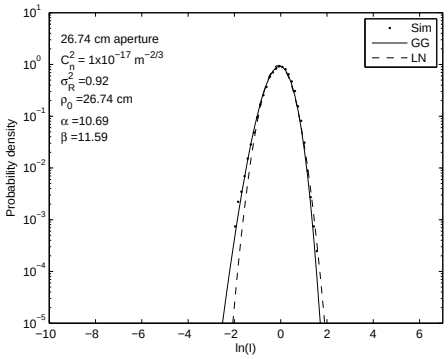

(e) 100 km

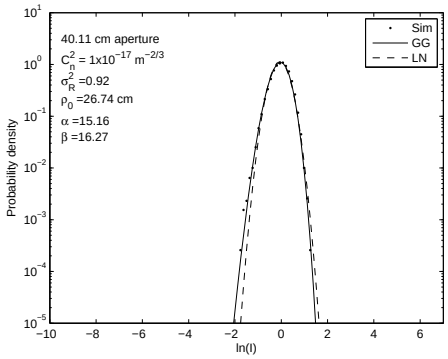

(f) 100 km

Figure 2.5: PDF of the normalized log irradiance $\ln(I)$ for the receiving apertures of diameter ρ_0 ((a),(c),(e)) and $3\rho_0/2$ ((b),(d),(f)). Simulation results for turbulence strength $C_n^2 = 1 \times 10^{-17}\ m^{-2/3}$ and propagation distance of 50 km, 75 km, and 100 km are compared to the gamma-gamma and lognormal PDF for each case.

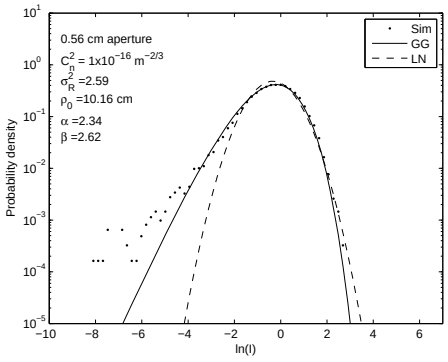

(a) 50 km

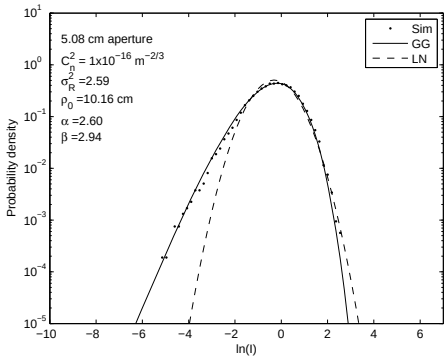

(b) 50 km

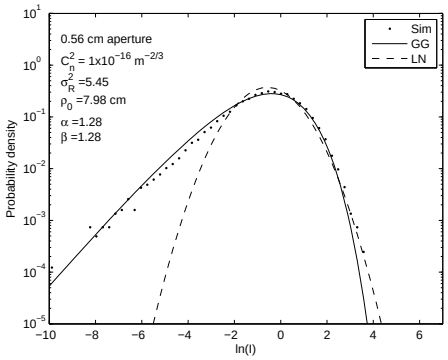

(c) 75 km

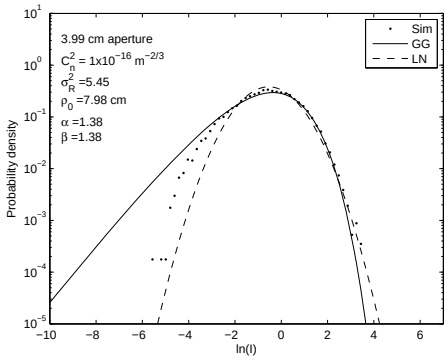

(d) 75 km

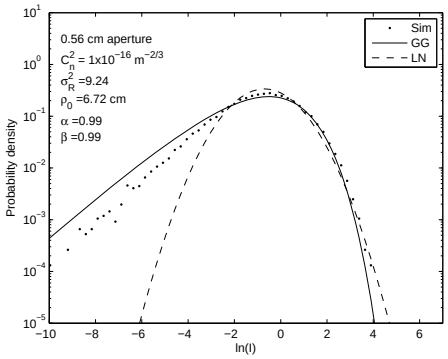

(e) 100 km

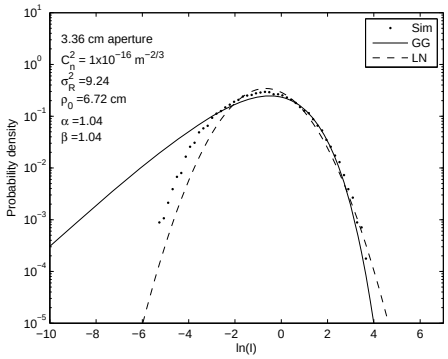

(f) 100 km

Figure 2.6: PDF of the normalized log irradiance $\ln(I)$ for the receiving apertures of diameter 5.6 mm ((a),(c),(e)) and $\rho_0/2$ ((b),(d),(f)). Simulation results for turbulence strength $C_n^2 = 1 \times 10^{-16}\ m^{-2/3}$ and propagation distance of 50 km, 75 km, and 100 km are compared to the gamma-gamma and lognormal PDF for each case.

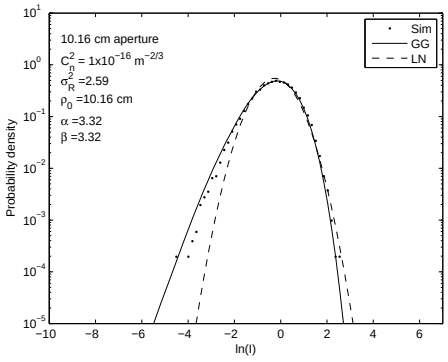

(a) 50 km

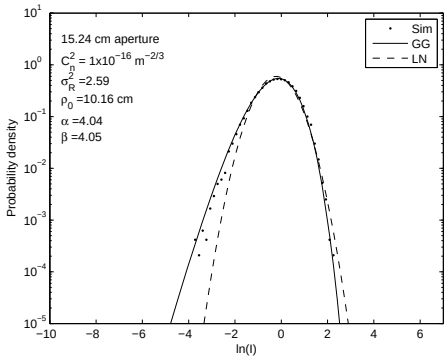

(b) 50 km

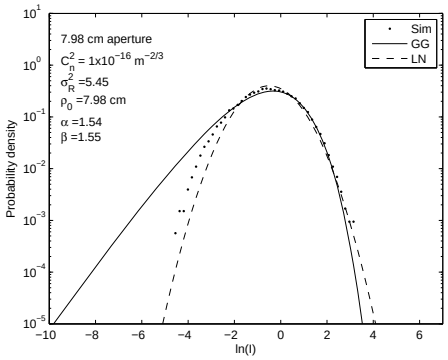

(c) 75 km

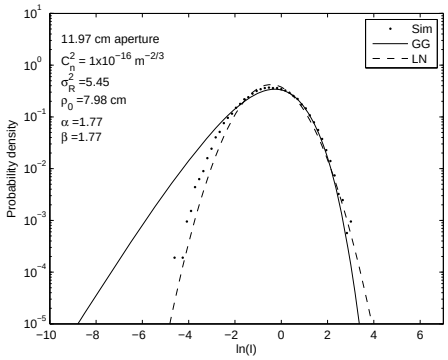

(d) 75 km

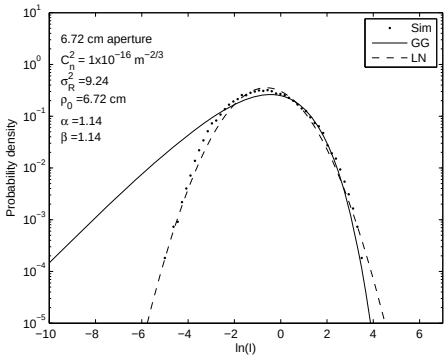

(e) 100 km

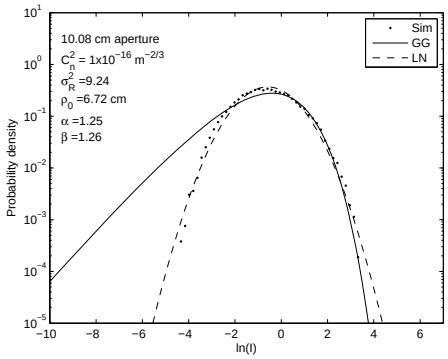

(f) 100 km

Figure 2.7: PDF of the normalized log irradiance $\ln(I)$ for the receiving apertures of diameter ρ_0 ((a),(c),(e)) and $3\rho_0/2$ ((b),(d),(f)). Simulation results for turbulence strength $C_n^2 = 1 \times 10^{-16}\ m^{-2/3}$ and propagation distance of 50 km, 75 km, and 100 km are compared to the gamma-gamma and lognormal PDF for each case.

PDFs begin to take on a different form. In Fig. 2.6(c) the PDF for the point-like aperture case is clearly gamma-gamma, but the remaining figures in the 75 km case reveal that the PDFs are transitioning between gamma-gamma and lognormal distributions. When the laser beam is in the moderate to strong scintillation regime the PDFs for the ρ_0 and $3\rho_0/2$ aperture size cases are expected to more closely match the lognormal PDF. Thus, one may infer that the laser beam although still in the moderate scintillation regime is nevertheless transitioning into the strong scintillation region. The subplots for the 100 km case show that the form of the PDFs are what we expect in strong scintillation. The gamma-gamma PDF provides a good fit for the point-like (0.56 mm diameter) aperture case 2.6(e), while the PDF in Fig. 2.6(f) is transitioning from a gamma-gamma PDF to a lognormal PDF. The remaining subfigures in the 100 km case show that the aperture averaged irradiance data are lognormal in their distribution.

Figs. 2.8 and 2.9 show comparisons between the simulation data and the theoretical data for turbulence strength $C_n^2 = 1 \times 10^{-15}\,\mathrm{m}^{-2/3}$. In strong turbulence and into the very strong turbulence condition, the shape of the PDF of the simulated irradiance data follows closely with that predicted for strong scintillation. The PDFs for the point-like aperture cases (first column of Fig. 2.8) are transitioning from a gamma-gamma distribution to a lognormal distribution. This may be due to the aperture size not being sufficiently smaller than the coherence radius for each propagation distance case. When the apertures are increased in size to $\rho_0/2$ for each propagation distance Fig. 2.8(b), 2.8(d), 2.8(f) (second column of Fig. 2.8), the simulated data appears to be transitioning from a gamma-gamma to a lognormal

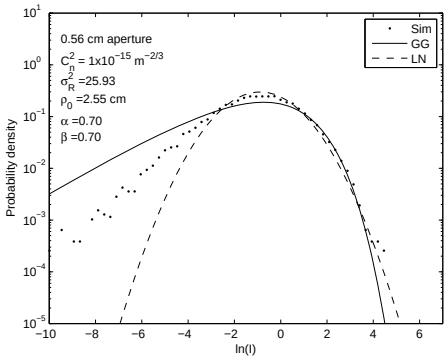

(a) 50 km

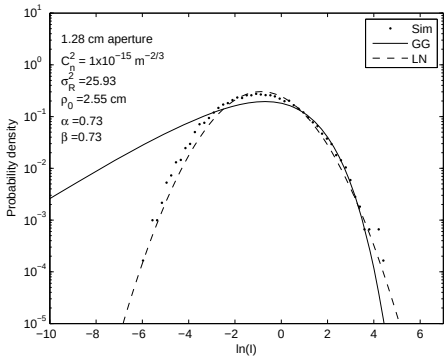

(b) 50 km

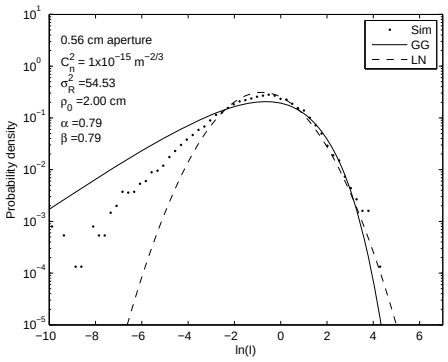

(c) 75 km

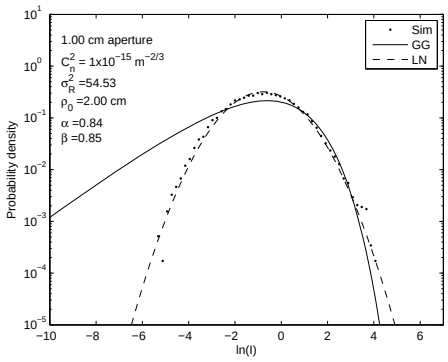

(d) 75 km

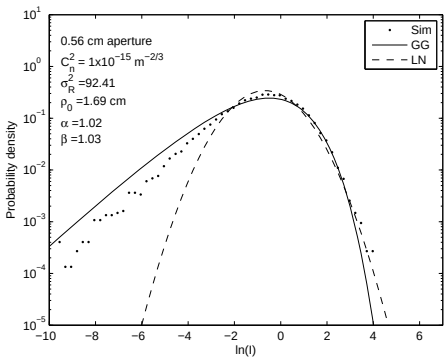

(e) 100 km

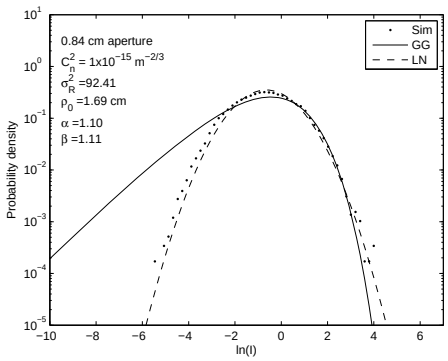

(f) 100 km

Figure 2.8: PDF of the normalized log irradiance $\ln(I)$ for the receiving apertures of diameter 5.6 mm ((a),(c),(e)) and $\rho_0/2$ ((b),(d),(f)). Simulation results for turbulence strength $C_n^2 = 1 \times 10^{-15}\ m^{-2/3}$ and propagation distance of 50 km, 75 km, and 100 km are compared to the gamma-gamma and lognormal PDF for each case.

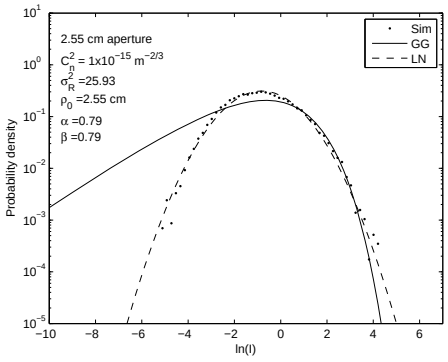

(a) 50 km

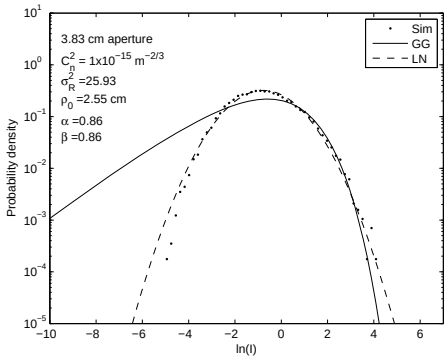

(b) 50 km

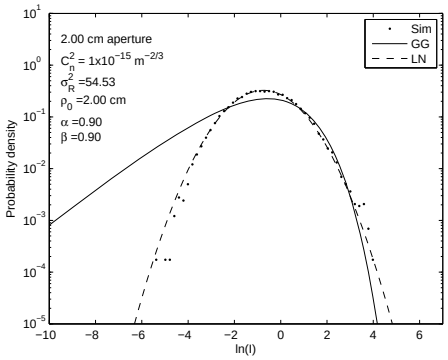

(c) 75 km

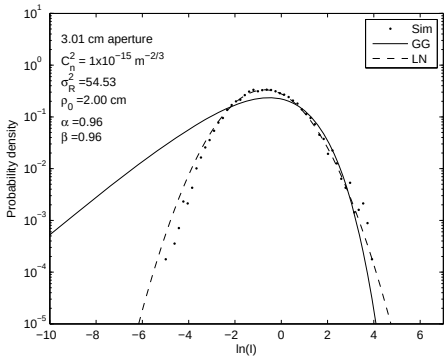

(d) 75 km

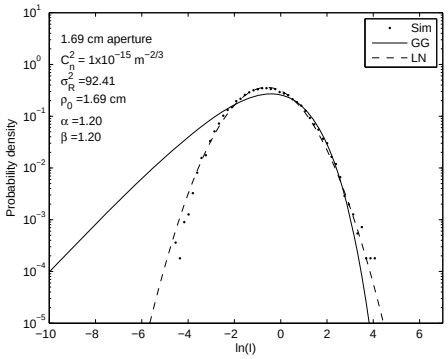

(e) 100 km

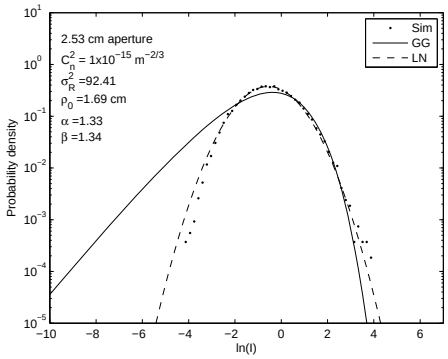

(f) 100 km

Figure 2.9: PDF of the normalized log irradiance $\ln(I)$ for the receiving apertures of diameter ρ_0 ((a),(c),(e)) and $3\rho_0/2$ ((b),(d),(f)). Simulation results for turbulence strength $C_n^2 = 1 \times 10^{-15}\ m^{-2/3}$ and propagation distance of 50 km, 75 km, and 100 km are compared to the gamma-gamma and lognormal PDF for each case.

distribution but much closer to the latter for all propagation distances. For the cases where the aperture size is equal to ρ_0 and larger (Fig. 2.9) the simulation data are closer to a lognormal distribution than they are to a gamma-gamma distribution.

2.4.2 Bit Error Rate

The performance of a FSO communication system can be predicted by computing the bit error rate (BER). The BER using the simulation data PDF for some scintillation cases used in this study was computed and compared to the BER using the theoretical gamma-gamma and lognormal PDFs. The BER expression for on-off keying (OOK) modulation under a Gaussian distribution of noise is given as [7]

$$BER(OOK) = \frac{1}{2}\int_0^\infty p(I)\,\mathrm{erfc}\left(\frac{\langle SNR\rangle I}{2\sqrt{2}}\right) ds, \tag{2.7}$$

where $p(I)$ is the probability distribution of the aperture averaged irradiance at the receiver, erfc is the complimentary error function, I is the aperture averaged irradiance at the receiver normalized by its mean, and $\langle SNR\rangle$ is the time averaged signal-to-noise ratio for the system.

Fig. 2.10 shows some examples of the BER calculated for SNR values ranging from 1 to 50, which have been converted to decibels by the expression $20log(SNR)$. Each subplot within the figure represents the calculated BER using the simulation PDF for a specific case of the laser communication link. Each simulation BER is compared to the BER calcu-

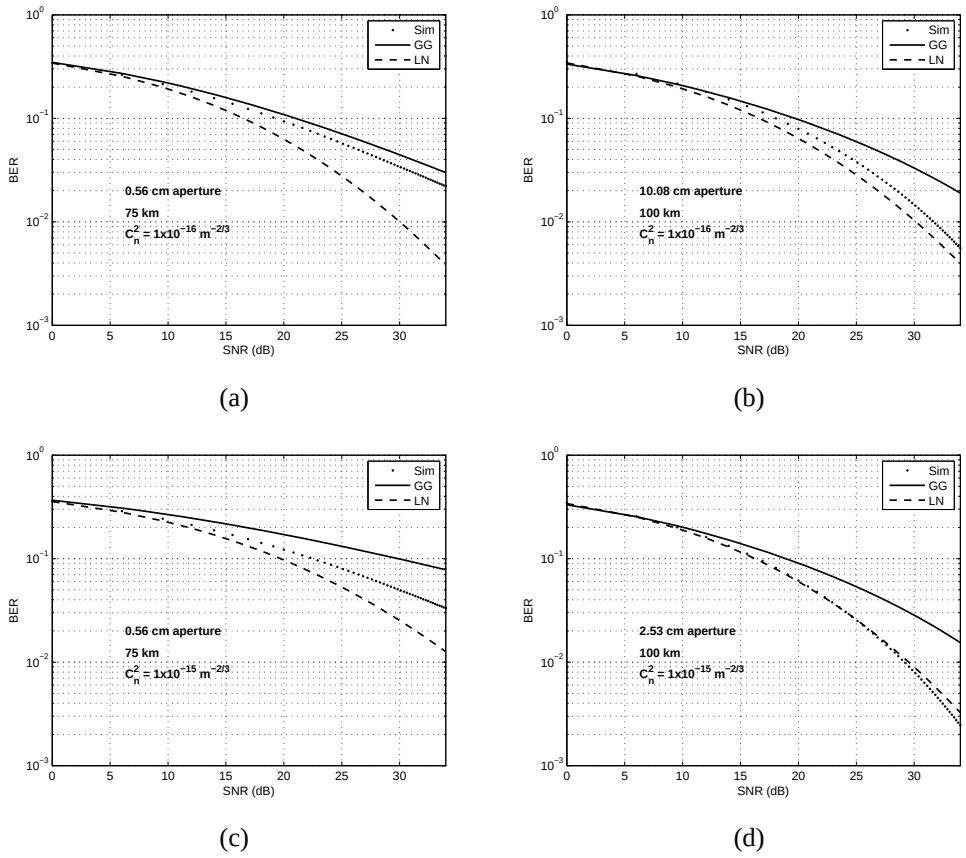

Figure 2.10: BER of the laser communication channel for the point-like and $3\rho_0/2$ diameter apertures for propagation distances of 75 km and 100 km and for turbulence strengths $C_n^2 = 1 \times 10^{-16}\,\mathrm{m}^{-2/3}$ ((a),(b)) and $C_n^2 = 1 \times 10^{-15}\,\mathrm{m}^{-2/3}$ ((c),(d)).

lated using the theoretical gamma-gamma and lognormal PDFs. Figs. 2.10(a) and 2.10(b) show the calculated BER for the point-like aperture and $3\rho_0/2$ diameter aperture with turbulence strength $C_n^2 = 1 \times 10^{-16}\,\mathrm{m}^{-2/3}$ and propagation distances of 75 km and 100 km, respectively. The corresponding PDF plots for these simulation cases are shown in Fig. 2.6(c) and Fig. 2.7(f), respectively. The simulation BER shown in Fig. 2.10(a) is closer to the gamma-gamma BER than to the lognormal BER as expected since the two PDFs were closely fit as shown in Fig. 2.6(c), while the simulation BER in Fig. 2.10(b) is closer to the lognormal BER. Figs. 2.10(c) and 2.10(d) show the calculated BER for the point-like

aperture and $3\rho_0/2$ diameter aperture with turbulence strength $C_n^2 = 1 \times 10^{-15}\,\mathrm{m}^{-2/3}$ and propagation distances of 75 km and 100 km, respectively. The corresponding PDF plots for these simulation cases are shown in Fig. 2.8(c) and Fig. 2.9(f), respectively. The simulation BER shown in Fig. 2.10(c) is in between the gamma-gamma and lognormal BERs similar to the positioning of the PDF in the tail as shown in Fig. 2.8(c). The simulation BER shown in Fig. 2.10(d) nearly overlaps the lognormal BER then as the SNR increases beyond 25 (approximately 28 dB) becomes lower than both theoretical BERs. The examples shown in Fig. 2.10 were chosen because their corresponding PDF plots are representative of those with perhaps more interesting features.

2.5 Conclusions

We have presented a study of the probability density of irradiance fluctuations averaged over receiver apertures varying in diameter from 0.56 cm to $3\rho_0/2$ through scintillation conditions ranging from weak into the very strong regime along horizontal propagation path lengths of 50 km, 75 km and 100 km. Generally, in weak scintillation for apertures larger than the Fresnel zone the lognormal PDF provides a good fit to the irradiance fluctuation data. However, since the gamma-gamma and lognormal PDF models tend to converge in weak turbulence conditions, it can also be argued that the gamma-gamma PDF also fits the data for all aperture sizes we studied. When the scintillation strength is mod-

erate ($0.55 \leq \sigma_R^2 \leq 5.45$ in our simulations), the distributions are gamma-gamma for all aperture sizes. This is interesting since in the moderate scintillation regime we expect the irradiance distribution to be lognormal for apertures larger than the coherence radius. The irradiance fluctuation PDF continues to exhibit a gamma-gamma distribution until the laser beam enters into the strong fluctuation regime. When in strong scintillation the PDF of the irradiance fluctuations have a lognormal distribution for apertures larger than or equal in size to the coherence radius and overall continue to be gamma-gamma distributed for apertures much smaller than the coherence radius. This condition continues into the very strong scintillation regime.

Chapter 3

Probability density of received optical power fluctuations for adaptively compensated Gaussian laser beams

3.1 Introduction

Turbulence in the atmosphere causes undesireable effects on the wavefront of a laser as it propagates to the receiver plane of a free space optical (FSO) communication link. These effects include phase and amplitude perturbations, beam spreading, and beam wander resulting in random fluctuations of the received power. Many studies have been conducted to

characterize the probability density function (PDF) of these fluctuations for point and finite diameter receiving apertures [10, 11, 6, 12, 13, 14, 15, 7, 1, 16, 17, 18, 19, 5]. One way to reduce the effects of turbulence on a laser communication system is by use of adaptive optics (AO) at the transmitter. AO systems use mechanical means to sense phase distortions and partially correct them in real time [3]. An AO system is comprised of some sort of beacon, which acts as a probe of the turbulence, a wavefront sensor (WFS), a deformable mirror (DM), an actuator command computer, and a tracker for beacon wavefront tip-tilt correction.

The goal of this study is to characterize the PDF of the fluctuations in the received power from a Gaussian laser beam that has been adaptively compensated at the transmitter using an AO system. The beacon for the AO system is co-located with the receiver. The complexity of the AO system was varied by changing the number of WFS subapertures spanning the diameter of the transmitter. A WFS with twelve, twenty four, and fifty two subapertures corresponding to low, medium, and high order and link distances of 10 km and 20 km are considered. The configuration of the subapertures was such that there was four, six, and eight subapertures spanning the WFS pupil diameter for the low, medium, and high orders respectively. Fig. 3.1 in section 3.2.2.3 depicts the WFS with the subaperture configurations. The power is collected simultaneously by finite circular receiver apertures of diameter 0.56 cm, $\rho_0/2$, ρ_0, and $3\rho_0/2$, where ρ_0 is the atmospheric spatial coherence radius and its expression can be found in [2]. The resulting PDF for each case is compared to lognormal and gamma-gamma PDF models, where the parameters were com-

puted from sample based estimates obtained from the simulation results, as well as to the uncompensated case.

Results show that a reduction in the variance of the power fluctuations at the receiver results in narrower PDFs for the compensated laser beam compared to the PDFs for the uncompensated beam. Also, the gamma-gamma PDF model provides the best fit to the distribution for the AO compensated cases for all aperture sizes in moderate scintillation as was shown for the uncompensated laser PDFs. However, there is no significant reduction in the variance and small values in the tail of the PDF for the AO compensated cases begin to appear as the degree of complexity in the AO system was increased for low-order to high-order. For the 10 km link distance cases, it can be seen that the BER improves by approximately five orders of magnitude at the maximum signal-to-noise ratio (SNR) for the low order AO system case compared to the uncompensated case. However, the BER increased as the complexity in AO increased, which is counter-intuitive. I conjecture that the non-reciprocal nature of the path is the underlying issue. Specifically, the wave aberration experienced by a beam traveling from the beacon, which is located at the receiver, to the transmitter, is not identical to the wave aberration acquired by a beam traveling in the opposite direction. Based on the empirical results presented here, we conjecture that the lower order correction provided by the simplest adaptive optics system examined here is a better approximation to the optimal beam to transmit than the beam output by the more complicated adaptive optics systems studied. The BER for the 20 km cases decreased slightly from the uncompensated cases to the low order AO case. However, no change in the BER was evident as the AO

complexity was increased. This is likely because of the increase in scintillation from the longer path length and thus no AO scheme is optimal under these scintillation conditions. We conclude that a low order AO system is adequate for precompensating a laser for propagation through a free space optical channel and that the added expense and complexity of a higher order AO system is unnecessary.

The remainder of the chapter is organized as follows. In section 2, the lognormal and gamma-gamma PDF models are presented as well as a detailed description of the AO system. In section 3, the wave-optics simulation is described. In section 4, results with discussion are presented. Also in section four, the bit-error rate (BER) for on-off keying (OOK) modulation for the optical channel is calculated using the measured simulation data PDF and compared to the BERs using the theoretical gamma-gamma and lognormal PDFs. In section 5, conclusions are given.

3.2 Theory

3.2.1 Probability Density Function Models

Several PDFs have been proposed as a model for the distribution function for the integrated irradiance fluctuations in the moderate scintillation regime. We now present the two PDF models that have found the widest acceptance in the literature, the gamma-gamma PDF and

the lognormal PDF.

3.2.1.1 Gamma-Gamma Probability Density Function

The gamma-gamma distribution has been supported by simulation data as a possible model for irradiance fluctuations in weak, moderate and strong scintillation [14]. The integrated irradiance at the receiver plane can be defined as $I = XY$, where X arises from large scale turbulent eddies and Y arises from statistically independent small scale turbulent eddies [15]. Here X and Y are random processes in which one process modulates the other and can be described as a doubly stochastic process. The gamma-gamma distribution is defined by [2]

$$p(I) = \frac{2(\alpha\beta)^{(\alpha+\beta)/2}}{\Gamma(\alpha)\Gamma(\beta)I}(I)^{(\alpha+\beta)/2}K_{\alpha-\beta}(2\sqrt{\alpha\beta I}), \qquad I > 0, \tag{3.1}$$

where α and β are parameters of the gamma-gamma distribution and represent the effects of the large and small spatial scale scintillation respectively, $\Gamma(x)$ is the gamma function, $K_\xi(v)$ is a modified Bessel function of the 2^{nd} kind, and I is the integrated irradiance normalized by it's mean. The parameters α and β are specifically defined as

$$\alpha = \frac{1}{\sigma_X^2}, \qquad \beta = \frac{1}{\sigma_Y^2}. \tag{3.2}$$

σ_X^2 and σ_Y^2 are the variances of the large and small spatial scale integrated irradiance fluctuations [2] and are given as

$$\sigma_X^2 = \exp(\sigma_{\ln X}^2) - 1, \qquad \sigma_Y^2 = \exp(\sigma_{\ln Y}^2) - 1, \tag{3.3}$$

where $\sigma_{\ln X}^2$ and $\sigma_{\ln Y}^2$ are the variances of the large and small spatial scale log irradiance fluctuations [2]. Andrews and Phillips [2] give expressions for $\sigma_{\ln X}^2$ and $\sigma_{\ln Y}^2$ for a Gaussian-beam wave where the receiver aperture diameter is taken into account. However, these expressions are not appropriate for use where AO is present in the system. Therefore α and β in the gamma-gamma PDF model were obtained using a best-fit to the simulation data as in [1, 5], while maintaining the relationship with σ_I^2 given as [1]

$$\sigma_I^2 = \left(1 + \frac{1}{\alpha}\right)\left(1 + \frac{1}{\beta}\right) - 1. \tag{3.4}$$

3.2.1.2 Lognormal Probability Density Function

The lognormal PDF is generally accepted as a representative model for irradiance fluctuations due to propagation through turbulence in the weak scintillation regime. The lognormal PDF assumes that the logarithm of the signal fluctuations are Gaussian distributed or in other words the distribution of the fluctuations are lognormal [2]. This study uses the

expression for the lognormal distribution found in [1]

$$p(I) = \frac{1}{I\sqrt{2\pi\sigma_{lnI}^2}} \exp\left\{ -\frac{\left[\ln(I) + \frac{1}{2}\sigma_{\ln I}^2\right]^2}{2\sigma_{\ln I}^2} \right\}, \qquad I > 0, \tag{3.5}$$

where $\sigma_{\ln I}^2$ is the log-irradiance variance. In the weak scintillation regime the normalized irradiance variance also called the scintillation index σ_I^2 is approximately equal to $\sigma_{\ln I}^2$, however in moderate-to-strong scintillation regimes this approximation no longer holds and the exact relation must be used, as it is always true. The expression for σ_I^2 is given as [2]

$$\sigma_I^2 = \frac{\left\langle I^2 \right\rangle - \langle I \rangle^2}{\langle I \rangle^2}, \tag{3.6}$$

where I is the irradiance measured at the receiver plane and $\langle \cdot \rangle$ represents an ensemble average. The expression for σ_{lnI}^2 is given as [1]

$$\sigma_{\ln I}^2 = \ln\left(\sigma_I^2 + 1\right), \tag{3.7}$$

where σ_I^2 is taken directly from the simulation. For consistency, $\sigma_{\ln I}^2$ is used in the lognormal PDF for all simulations in this study.

3.2.2 Adaptive Optics System

A typical adaptive optics (AO) system consists primarily of a laser beacon or guide star, a wavefront sensor (WFS), a deformable mirror (DM), and an actuator command computer. The purpose of the laser beacon is to probe the atmosphere and provide phase information induced by turbulence that can be used to precompensate the outgoing communication laser beam. The function of the WFS is to measure the phase aberrations in the beacon wavefront and send that information to the actuator command computer. The actuator command computer converts this information to electrical signals for the DM. The DM is a flexible mirror that accepts the signals from the computer and can modify its surface shape at high speeds to approximate the conjugate of the turbulence induced phase error in the beacon wavefront [3]. The phase corrections are then imparted to the outgoing beam upon reflection in order to precompensate it before propagating to the receiver. This process must be performed at speeds on the order of the time-rate-of-change of the turbulence induced phase aberrations [3]. A more detailed description of the AO system used in this study is now presented.

3.2.2.1 Laser Beacon

The laser beacon used in the simulation is modeled as a collimated and spatially truncated Gaussian laser beam that is situated at the receiver plane and has a pupil diameter of 10

cm. A model for a Gaussian beam is given in the simulation section. The purpose of the beacon is to probe the atmosphere along the link path to provide information for the WFS in the form of a phase aberrated wavefront induced by the path averaged turbulence within the channel. The WFS retrieves this information, which can then be used to precompensate the outgoing beam propagated back towards the receiver. Before entering the WFS pupil however, a low-order tracker is employed to correct the tip-tilt in the beacon wavefront. Tilt removal is described in section 3.2.2.2. The perturbed optical field incident upon the WFS can be represented by [3] $\exp[j\phi(\vec{x},t)]$, where $\vec{x}$ is a spatial position in the WFS pupil, t is time, and $\phi(\vec{x},t)$ is the wavefront phase.

3.2.2.2 Tilt Correction

Modern AO systems typically have a tilt correction mirror as the first stage of wavefront compensation [3]. These mirrors are usually separate from the DM in order to reduce the dynamic range requirements of the DM. The simulations used in this study model tilt removal using a method whereby an image is formed of the incident beacon field across the pupil from which the x and y-directed components of the slope of that image are computed. This is a measure of the full aperture tilt and is removed from the beacon field as

$$U_{tr}(x,y,t) = U_i(x,y,t)e^{-j\phi_{tilt}(x,y,t)}, \tag{3.8}$$

where $U_i(x,y,t)$ is the incident beacon wavefront before tilt is removed, $\phi_{tilt}(x,y,t)$ is the phase component of the incident wavefront containing the tilt, and $U_{tr}(x,y,t)$ is the wavefront entering the WFS pupil after tilt has been removed.

3.2.2.3 Wavefront Sensor

Wavefront sensors measure the spatial gradient or Laplacian of the phase $\phi(\vec{x},t)$ [3], which can then be used to estimate $\phi(\vec{x},t)$ through a phase reconstruction algorithm. In this simulation, a least-squares reconstruction algorithm is used. The WFS modeled in the simulation is a Hartman type WFS, where the incoming beacon wavefront is spatially segmented by a series of lenslets arranged in the WFS pupil to optimize the pupil area. Each lenslet, also referred to as a subaperture, focuses a portion of the wavefront onto a series of detectors positioned in the back focal plane of the lenslet. The position of this spot in the detector plane can then be used to calculate the slope of the wavefront across that subaperture. The relationship of the wavefront slope $\vec{s}$ across the subaperture to the spot location $\vec{x}_s$ in the detector plane is given as [3]

$$\vec{s} = k\frac{\vec{x}_s}{f_l}, \tag{3.9}$$

where λ is the laser wavelength, and f_l is the focal length of the subaperture lenslet. This is equivalent to computing the average phase gradient $\phi(\vec{x},t)$ over that subaperture [3].

$$\vec{s}(j) = \int d\vec{x} W_{sj}(\vec{x}) \nabla\phi(\vec{x},t), \tag{3.10}$$

where the subaperture function is normalized so that $\int d\vec{x} W_{sj} = 1$. The configuration of the subapertures in the WFS for low, medium, and high degrees of compensation are shown in Fig. 3.1.

Each subaperture configuration case shown corresponds to a PDF of the power from the resulting compensated laser beam for one of two link distances that are displayed in the results section. Each of these configurations corresponds to a different case used to obtain

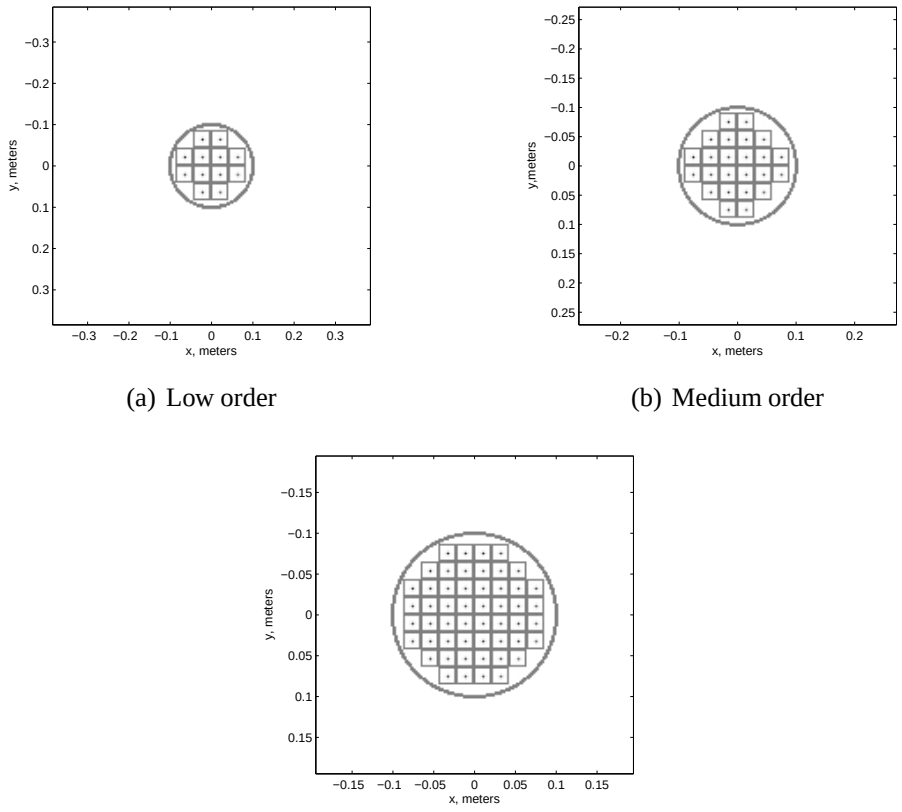

(a) Low order

(b) Medium order

(c) High order

Figure 3.1: Wavefront sensor showing subaperture locations and subaperture centers for a. low order (12 subapertures), b. medium order (24 subapertures), and c. high order (52 subapertures) configurations

a PDF of the resulting power collected at the receiver plane.

3.2.2.4 Deformable Mirror

The WFS measurements are sent to an actuator command computer that processes the information and converts it to electrical signals, which are applied to the DM actuators. The DM is a flexible mirror whose surface shape can be altered at high speeds by actuators positioned behind the mirror surface in locations corresponding to the centers of the WFS subapertures. The actuators accept electrical signals from the actuator command computer and adjust the mirror surface by pushing and pulling the mirror to create a conjugate of the phase aberrated beacon wavefront. The optical field, which has been precompensated by the DM upon reflection can then be represented by

$$\exp[j\varepsilon(\vec{x},t)] = \exp[j\zeta(\vec{x},t)]\exp[-j\hat{\phi}(\vec{x},t)], \tag{3.11}$$

where $\zeta(\vec{x},t)$ is the initial wavefront phase of the outgoing beam just before reflection, $\hat{\phi}(\vec{x},t)$ is the estimate for the tilt-removed beacon wavefront phase and it's conjugate is applied to the surface of the DM, and $\vec{x}$ is a spatial position in the plane containing the DM. The surface of the DM after alteration by the actuators (assuming linearity of all of the actuator responses) can be modeled by [3]

$$\hat{\phi}(\vec{x},t) = \sum_i c_i(t) r_i(\vec{x}), \tag{3.12}$$

where $c_i(t)$ is the control signal applied to the ith actuator at time t, $r_i(\vec{x})$ is the ith influence function, and $\vec{x}$ is a position on the DM surface. The influence function is defined as the change in the DM surface shape due to the application of a signal to an actuator [3]. Finally, the conjugate of the tilt is applied to the outgoing field in order to precompensate it for propagation to the receiver as

$$U_T(x,y,t) = U_r(x,y,t)e^{-j\phi_{tilt}(x,y,t)}, \tag{3.13}$$

where $U_r(x,y,t)$ is the perturbed field reflected off of the DM and $U_T(x,y,t)$ is the transmitted field that is propagated to the receiver.

3.3 Simulation

In order to observe how the PDF of received optical power for a lasercom link through atmospheric turbulence behaves when adaptive optics is incorporated into the system, a numerical wave-optics simulation was developed. A previous study [5] showed the evolution of the PDF of an uncompensated Gaussian laser beam through a comprehensive set of scintillation conditions. This study seeks to incorporate those findings and expand upon them to include an AO system and observe the changes in the PDF of the received optical power from the outgoing laser beam when the number of subapertures within the WFS is increased. Careful attention was placed on the development of the simulation parameters

and for this reason simulation guidelines presented by Rao [22] and Belmonte [23] were followed closely.

The propagation path is assumed to be horizontal, which allows for a constant refractive index structure parameter chosen to be $C_n^2 = 1 \times 10^{-15}\ m^{-2/3}$. The link distances used in this study were chosen to be 10 km and 20 km. The Rytov variance σ_R^2 is a measure of the degree of scintillation and its expression is given as [2]

$$\sigma_R^2 = 1.23 C_n^2 k^{7/6} L^{11/6}, \tag{3.14}$$

where L is the link distance. These link distances and turbulence strength provided scintillation conditions in the moderate regime with Rytov variances calculated to be $\sigma_R^2 = 1.36$ and $\sigma_R^2 = 4.83$ respectively.

A model for an initially collimated and spatially truncated Gaussian beam is

$$U(x,y) = A_0 \exp\left[-\frac{(x^2+y^2)}{W_0^2}\right] \times P(x,y), \tag{3.15}$$

where A_0 represents the peak amplitude of the outgoing beam, taken to be unity. W_0 is the e^{-1} radius at the transmitter. $P(x,y)$ represents the finite pupil, where $P(x,y) = 1$ inside the pupil and $P(x,y) = 0$ outside the pupil. The initial beam radius $W_0 = 7.08$ cm is calculated from the transmitter aperture diameter d by the expression $W_0 = d/2\sqrt{2}$ given in [20], where d was chosen to be 20 cm. The beam wavelength was $\lambda = 1.55\ \mu$m, which is a

widely used wavelength in laser communication. At the receiver plane, the optical power was collected simultaneously by four separate apertures. The diameter of each aperture was chosen to be 0.56 cm, $\rho_0/2$, ρ_0, and $3\rho_0/2$ as was done in [5]. The small aperture was simulated by a single square pixel located in the center of the propagation grid at the receiver plane. The area of the square pixel is $25\,\mathrm{mm}^2$, which corresponds to a circular aperture with a diameter of 5.64 mm. The remaining aperture diameters were calculated separately for each simulation based on the propagation length and turbulence strength.

The complex field was propagated through homogeneous and isotropic atmospheric turbulence using a Fresnel propagator from a Matlab toolbox AOTools [24]. The atmosphere was simulated by dividing the total propagation distance into several smaller distances, each followed by a randomly generated phase screen. The phase screens were comprised of 512×512 grid points for the 10 km case and 750×750 grid points for the 20 km case.

The spatial sampling interval Δx was chosen to be 5 mm for both link distance cases making the edge dimension of each physical grid size 2.56 m and 3.75 m, respectively. The Kolmogorov turbulence spectrum phase screen generator by a widely available software tool from a Matlab toolbox AOTools [24] was used and inner and outer scale effects were ignored. The number of phase screens used for each link distance case was determined by calculating $\sigma_R^2(\Delta z)$ for each propagation step and making sure that it remained under 10 % that of $\sigma_R^2(L)$ for the total link distance. In addition, the scintillation index was kept below 0.1 per propagation step as pointed out by Rao [22].

The log-irradiance variance $\sigma^2_{\ln I}$ was determined by measuring σ^2_I directly from the data and using Eq.(3.7). In addition, α and β in the gamma-gamma PDF model were obtained using a best-fit to the simulation data as in [1, 5], while maintaining the relationship with σ^2_I as given in 3.4

3.4 Results

3.4.1 Probability Distribution

Figs. 3.2 through 3.9 represent the PDFs of the normalized log of the integrated irradiance $\ln(I)$ measured at the receiver plane of a free space optical communication link and are compared to the theoretical lognormal and gamma-gamma PDF models. Each subplot of a figure represents the PDF of $\ln(I)$ data collected for each of four different diameter circular apertures. The aperture diameters used are point-like (5.64 mm), $\rho_0/2$, ρ_0, and $3\rho_0/2$, where ρ_0 is dependent on the atmospheric turbulence strength characterized by the refractive index structure parameter $C_n^2 = 1 \times 10^{-15}\ m^{-2/3}$ and the link distances of 10 km and 20 km. The aperture sizes were chosen in this way to observe the form of the PDF of integrated irradiance fluctuations on a point-like receiving aperture and on apertures as they transition in size through the turbulence coherence radius ρ_0 and beyond to an aperture larger than the coherence radius. The theoretical PDFs used in this comparison

are the lognormal PDF (dashed curve) and the gamma-gamma PDF (solid curve) for both uncompensated and AO compensated laser beam cases and are described in detail in section 2. The log irradiance variance $\sigma^2_{\ln I}$, which is related to the scintillation index by the relation given in Eq. (3.7) was used to calculate the lognormal PDF for all scintillation conditions. As in [5], the comparisons made between the integrated irradiance fluctuation data PDF and the theoretical PDFs focus on the tail (small irradiance values) since this is the portion of the PDF that is important for understanding the fade statistics of FSO communication systems.

Fig. 3.2 shows the PDF for the uncompensated case, while Figs. 3.3 through 3.5 depict the PDFs for the adaptively compensated Gaussian laser beam cases for the low, med, and high order WFS cases respectively for a 10 km horizontal lasercom link through atmospheric turbulence. The link distance and turbulence strength result in a moderate scintillation regime ($\sigma_R^2 = 1.36$). It can be seen in Fig. 3.2 that the gamma-gamma model presents a much better fit to the distribution of the simulated data for the uncompensated case than does the lognormal model as is expected in moderate scintillation from results found in [5]. From Figs. 3.3 through 3.5 it is noticed that the PDFs are narrower for all apertures compared to the uncompensated case in Fig. 3.2 and the figures show that the PDFs become slightly more narrow as the order of the WFS increases. With more subapertures the WFS is better able to measure the details of the aberrations in the beacon wavefront, which is then translated to the DM and subsequently the outgoing laser beam resulting in a reduction in the variance of the power collected at the receiver. In addition, there is a significant

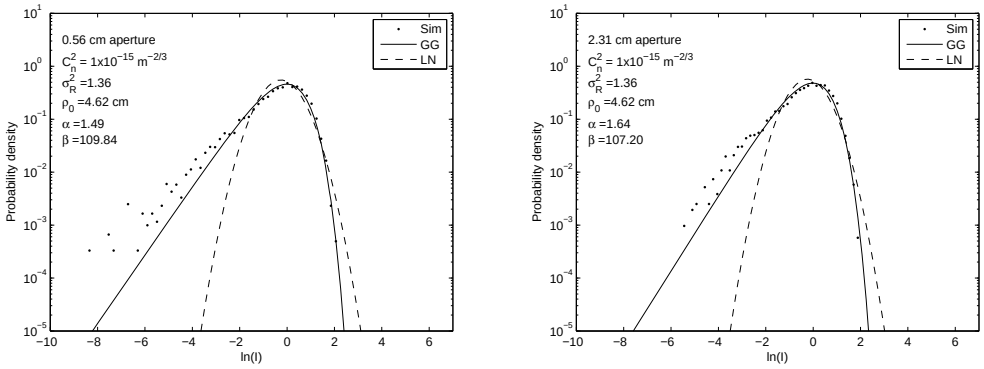

(a) 10 km

(b) 10 km

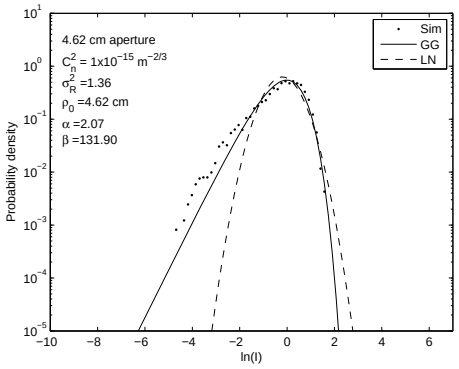

(c) 10 km

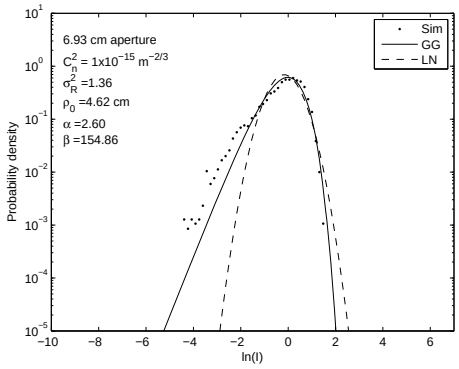

(d) 10 km

Figure 3.2: PDF of the normalized log irradiance $\ln(I)$ for an uncompensated Gaussian beam for the receiving apertures of diameter 5.6 mm(point receiver)(a), $\rho_0/2$ (b), ρ (c), and $3\rho/2$ (d). Simulation results for turbulence strength $C_n^2 = 1 \times 10^{-15}\ m^{-2/3}$ and propagation distance of 10 km are compared to the gamma-gamma and lognormal PDF for each case.

decrease in the number of small values in the tail of the PDF when comparing the low-order compensated PDFs to the uncompensated PDFs. However, it is noted that there is a slight increase in the small values in the tails of the PDFs as the AO complexity is increased. It is also noted that the gamma-gamma PDF model, which provides a better fit to the distribution than does the lognormal model for the uncompensated case also provides a better fit in all cases of the compensated beam. These PDF results are in line with those shown by Tyson [7], however Tyson's study only incorporated tip/tilt AO correction.

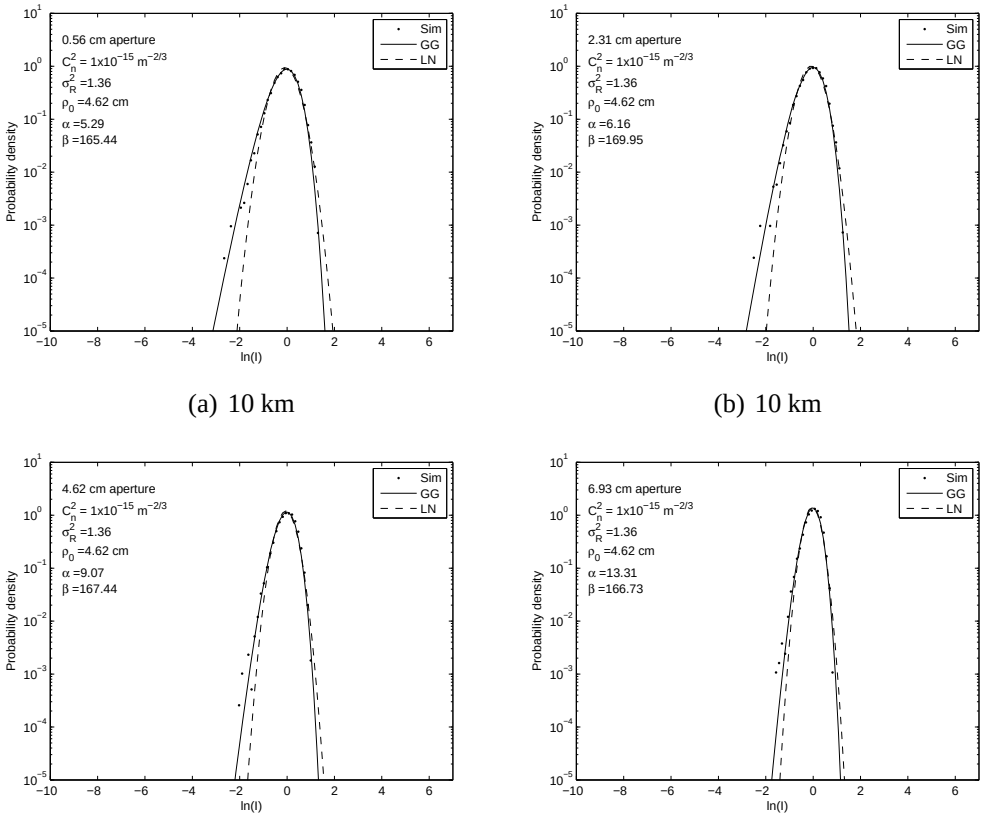

(a) 10 km (b) 10 km

(c) 10 km (d) 10 km

Figure 3.3: PDF of the normalized log irradiance $\ln(I)$ for a low order adaptively compensated Gaussian beam for the receiving apertures of diameter 5.6 mm(point receiver)(a), $\rho_0/2$ (b), ρ (c), and $3\rho/2$ (d). Simulation results for turbulence strength $C_n^2 = 1 \times 10^{-15}\ m^{-2/3}$ and propagation distance of 10 km are compared to the gamma-gamma and lognormal PDF for each case.

Fig. 3.6 depicts the PDF for the uncompensated case, while Figs. 3.7 through 3.9 depict the PDFs for the adaptively compensated Gaussian laser beam cases for the low, med, and high order WFS cases respectively for a 20 km horizontal lasercom link through atmospheric turbulence. At 20 km with a Rytov variance of $\sigma_R^2 = 4.83$, the scintillation conditions are still moderate but entering into the strong regime. It can be seen in Fig. 3.6 that the gamma-gamma PDF model again provides the better fit to the distribution of the simulated data than does the lognormal PDF model. However, it can be seen in the larger aperture

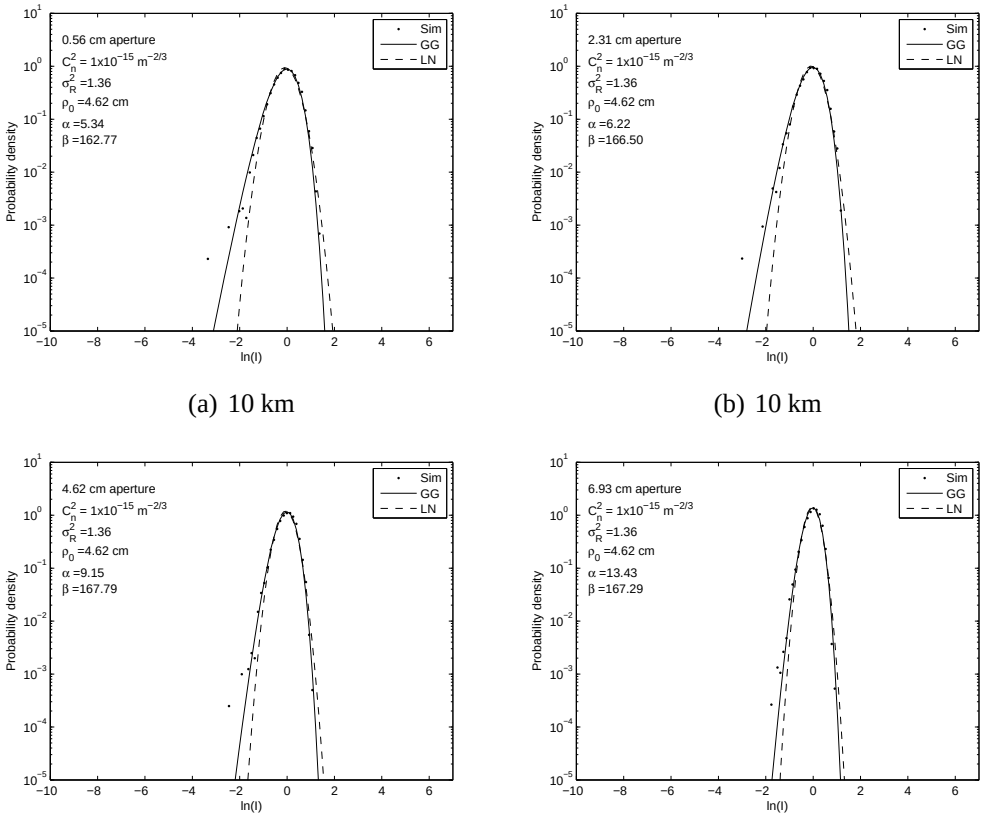

(a) 10 km (b) 10 km

(c) 10 km (d) 10 km

Figure 3.4: PDF of the normalized log irradiance $\ln(I)$ for a medium order adaptively compensated Gaussian beam for the receiving apertures of diameter 5.6 mm(point receiver)(a), $\rho_0/2$ (b), ρ (c), and $3\rho/2$ (d). Simulation results for turbulence strength $C_n^2 = 1 \times 10^{-15}\ m^{-2/3}$ and propagation distance of 10 km are compared to the gamma-gamma and lognormal PDF for each case.

cases (Figs. 3.6(b) through 3.6(d)) that the distribution is perhaps beginning to migrate away from the gamma-gamma PDF towards eventually becoming lognormal in a higher scintillation regime. This phenomenon was well noted in [1, 5]. In Figs. 3.7 through 3.9 it can be seen that the PDFs once again become slightly more narrow compared to the uncompensated case although not as pronounced as was seen in the 10 km cases. This is a consequence of a higher scintillation regime and therefore a less dramatic influence from the AO compensation on the PDF of the received power. It can be seen that the PDF

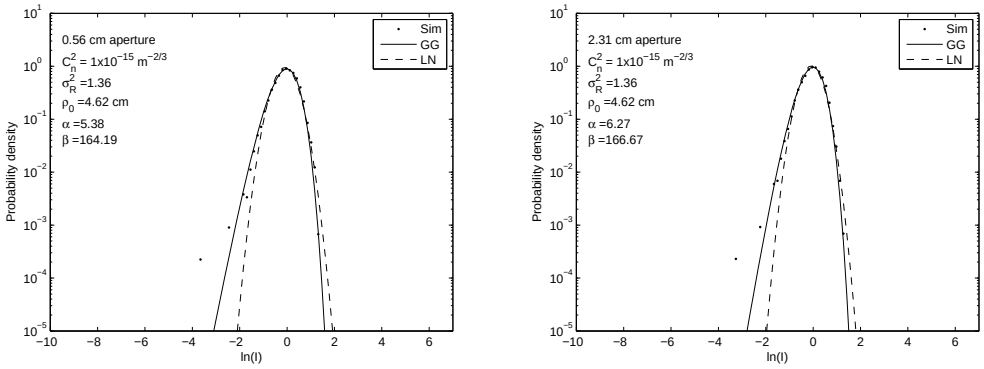

(a) 10 km

(b) 10 km

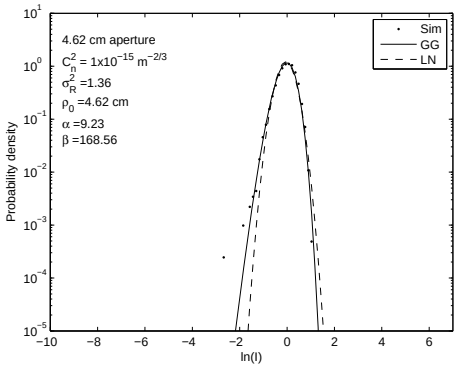

(c) 10 km

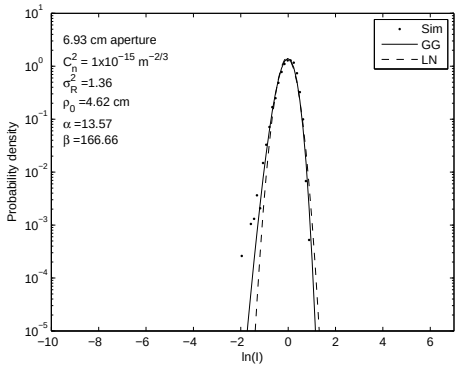

(d) 10 km

Figure 3.5: PDF of the normalized log irradiance $\ln(I)$ for a high order adaptively compensated Gaussian beam for the receiving apertures of diameter 5.6 mm(point receiver)(a), $\rho_0/2$ (b), ρ (c), and $3\rho/2$ (d). Simulation results for turbulence strength $C_n^2 = 1 \times 10^{-15}\ m^{-2/3}$ and propagation distance of 10 km are compared to the gamma-gamma and lognormal PDF for each case.

narrows slightly as the WFS order is increased. In all of the compensated cases it is shown that the gamma-gamma PDF model provides a good fit to the simulated data distribution. In fact the distribution becomes more gamma-gamma distributed in the compensated cases than in the uncompensated case for the $\rho_0/2$, ρ_0, and $3\rho_0/2$ aperture sizes. Unlike the 10 km link distance case, the number of values in the tail (small values) slightly increases. The PDF values shift towards the tail in the larger aperture diameter ρ_0 and $3\rho_0/2$ cases compared to the uncompensated case. As in the 10 km case, there is very little difference

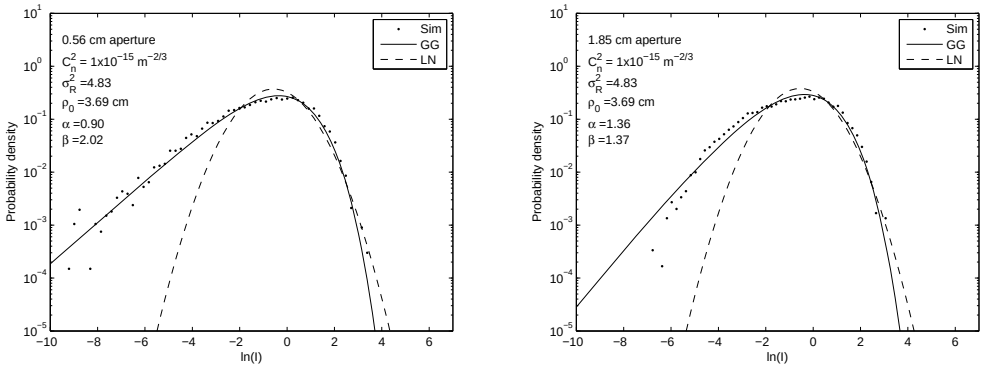

(a) 20 km

(b) 20 km

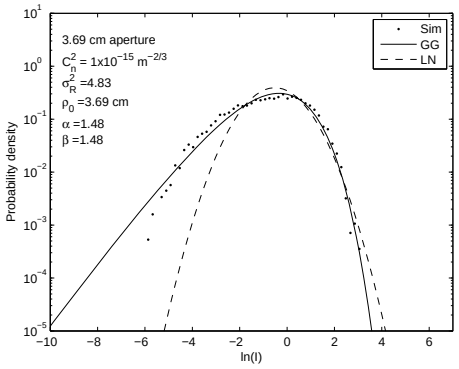

(c) 20 km

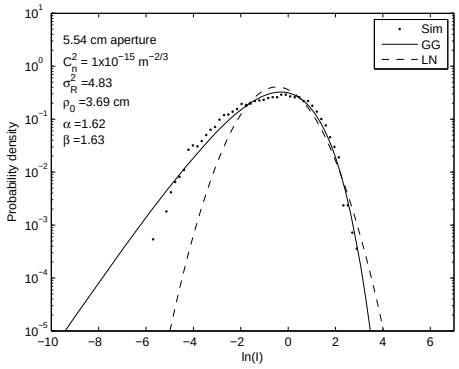

(d) 20 km

Figure 3.6: PDF of the normalized log irradiance $\ln(I)$ for an uncompensated Gaussian beam for the receiving apertures of diameter 5.6 mm(point receiver)(a), $\rho_0/2$ (b), ρ (c), and $3\rho/2$ (d). Simulation results for turbulence strength $C_n^2 = 1 \times 10^{-15}\ m^{-2/3}$ and propagation distance of 20 km are compared to the gamma-gamma and lognormal PDF for each case.

notable in the values of the PDF tails as the WFS order increases.

In both link distance cases, although not shown it is noted that there was a significant increase in received power for the compensated beam compared to the uncompensated for all aperture sizes. However, there was only an insignificant increase in power measured as the order of the WFS was increased beyond the low order.

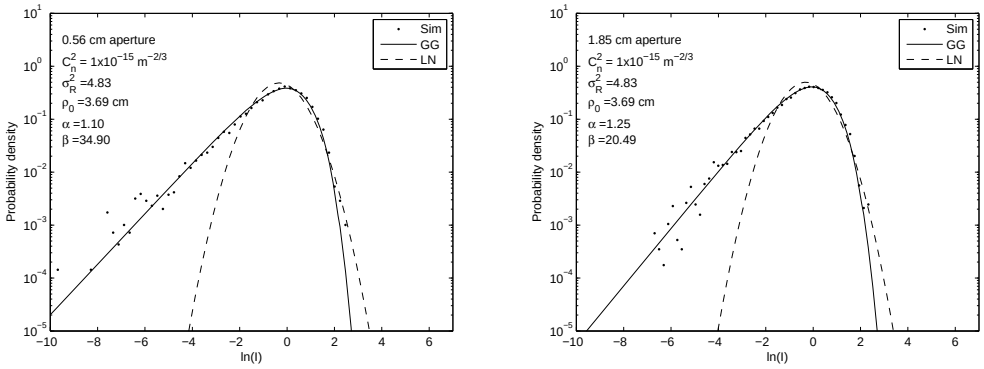

(a) 20 km

(b) 20 km

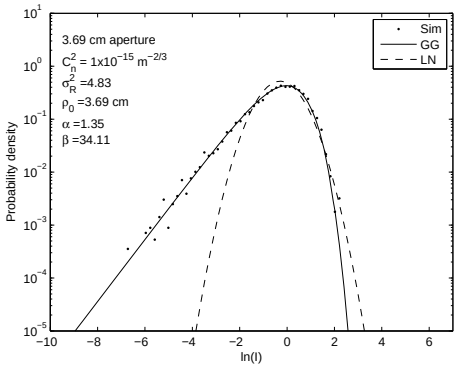

(c) 20 km

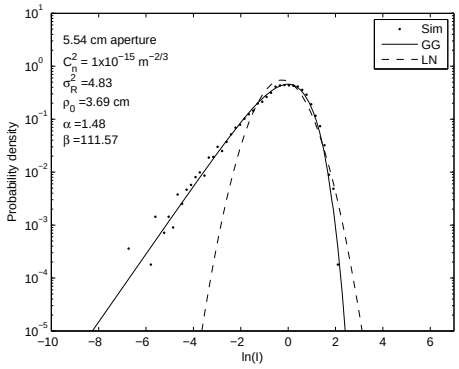

(d) 20 km

Figure 3.7: PDF of the normalized log irradiance $\ln(I)$ for a low order adaptively compensated Gaussian beam for the receiving apertures of diameter 5.6 mm(point receiver)(a), $\rho_0/2$ (b), ρ (c), and $3\rho/2$ (d). Simulation results for turbulence strength $C_n^2 = 1 \times 10^{-15}\ m^{-2/3}$ and propagation distance of 20 km are compared to the gamma-gamma and lognormal PDF for each case.

3.4.2 Bit-Error Rate

The performance of a FSO communication system can be predicted by computing the bit error rate (BER). The BER using the simulation data PDF for some scintillation cases used in this study was computed and compared to the BER using the theoretical gamma-gamma and lognormal PDF models. The BER expression for on-off keying (OOK) modulation is

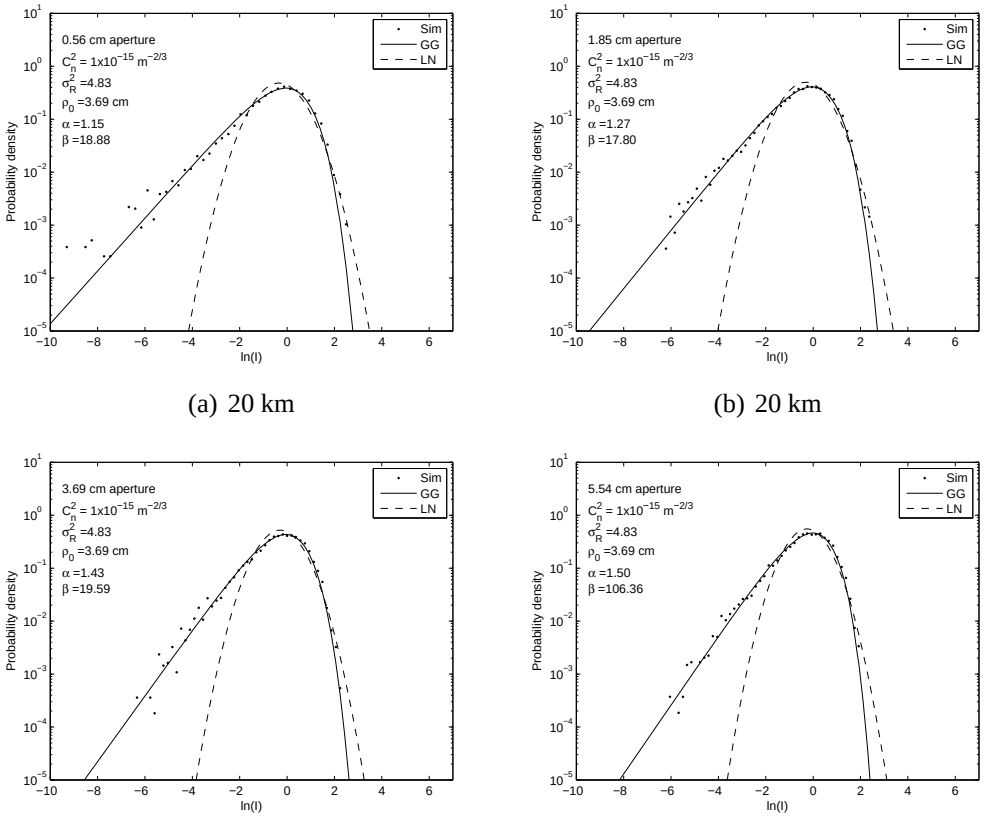

(a) 20 km (b) 20 km

(c) 20 km (d) 20 km

Figure 3.8: PDF of the normalized log irradiance $\ln(I)$ for a medium order adaptively compensated Gaussian beam for the receiving apertures of diameter 5.6 mm(point receiver)(a), $\rho_0/2$ (b), ρ (c), and $3\rho/2$ (d). Simulation results for turbulence strength $C_n^2 = 1 \times 10^{-15}\ m^{-2/3}$ and propagation distance of 20 km are compared to the gamma-gamma and lognormal PDF for each case.

given as [7]

$$BER(OOK) = \frac{1}{2}\int_0^\infty p(I)\,\mathrm{erfc}\left(\frac{\langle SNR\rangle I}{2\sqrt{2}}\right)dI, \tag{3.16}$$

where $p(I)$ is the probability distribution of the integrated irradiance at the receiver, erfc is the complimentary error function, I is the integrated irradiance at the receiver normalized by its mean, and $\langle SNR\rangle$ is the time averaged signal-to-noise ratio for the system.

Figs. 3.10 and 3.11 show some examples of the BER calculated for SNR values rang-

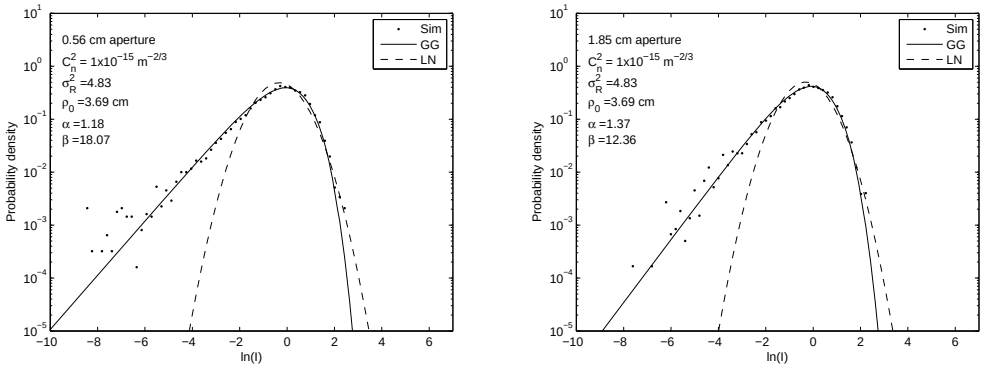

(a) 20 km

(b) 20 km

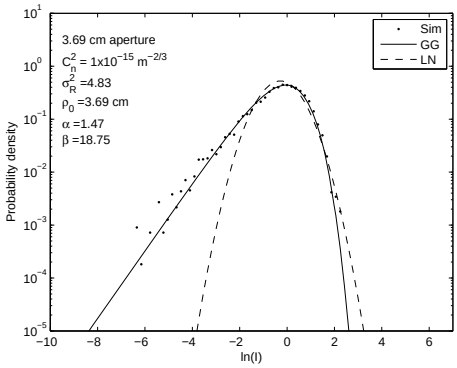

(c) 20 km

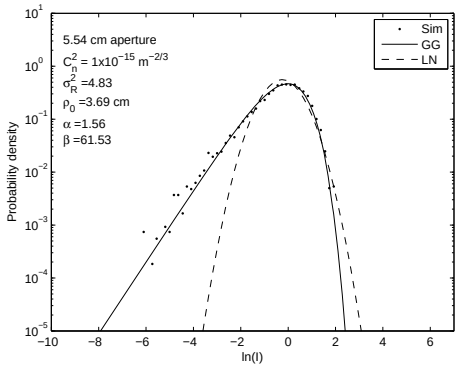

(d) 20 km

Figure 3.9: PDF of the normalized log irradiance $\ln(I)$ for a high order adaptively compensated Gaussian beam for the receiving apertures of diameter 5.6 mm(point receiver)(a), $\rho_0/2$ (b), ρ (c), and $3\rho/2$ (d). Simulation results for turbulence strength $C_n^2 = 1 \times 10^{-15}\ m^{-2/3}$ and propagation distance of 20 km are compared to the gamma-gamma and lognormal PDF for each case.

ing from 1 to 50, which have been converted to decibels by the expression $20log(SNR)$. Each subplot within the figure represents the calculated BER using the simulation PDF of the ρ_0 diameter aperture for the 10 km and 20 km link distances. Each simulation BER is compared to the BER calculated using the theoretical gamma-gamma and lognormal PDFs. Figs. 3.10(a) and 3.10(b) show the calculated BER for the uncompensated cases for the 10 km and 20 km link distances respectively. The corresponding PDF plots for these simulation cases are shown in Figs. 3.2(c) and 3.6(c) respectively. It can be seen

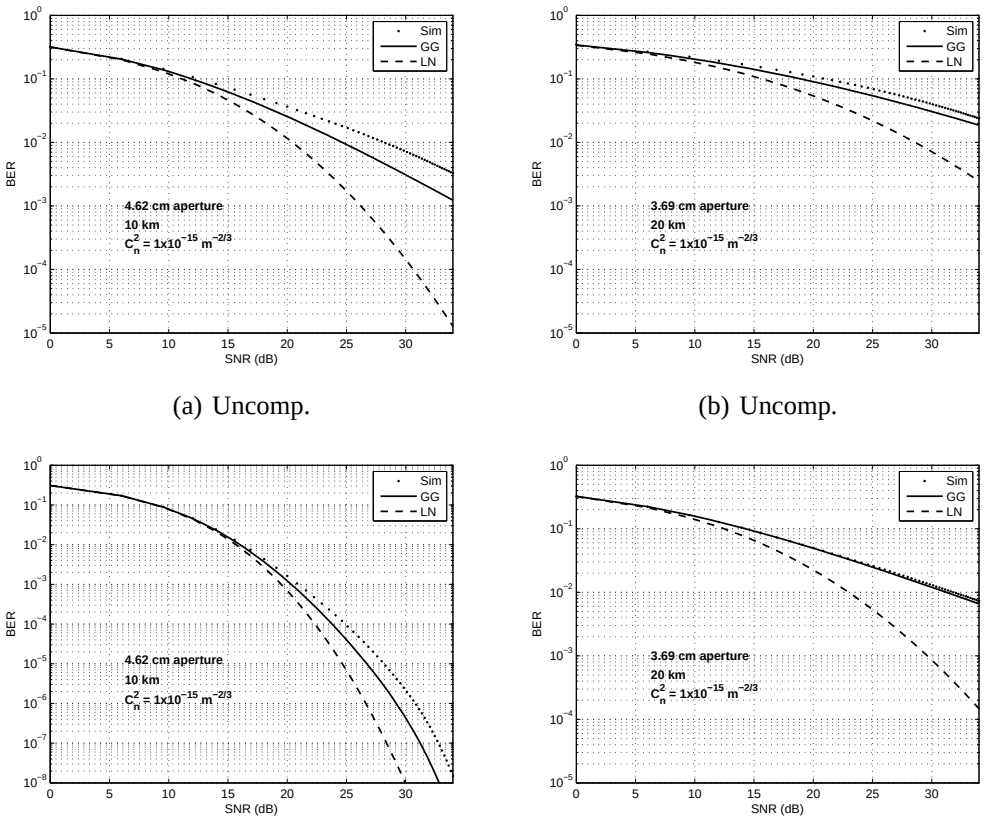

(a) Uncomp. (b) Uncomp.

(c) Low Order (d) Low Order

Figure 3.10: BER of the laser communication channel for the uncompensated laser (a, b) and low order compensated laser (c, d) for the ρ_0 diameter aperture and 10 km and 20 km link distances respectively.

that the simulation BER for the 10 km case dips lower than for the 20 km case. This is to be expected since the 20 km link has a stronger scintillation than does the 10 km link. At the maximum SNR, the BER for the simulation data in the 10 km case is approximately 3.3×10^{-3} compared with 2.4×10^{-2} for the 20 km case at the same SNR. It is also noticed that both theoretical model BERs dip lower in the 10 km case as well. This is especially true for the lognormal BER. For the 10 km low order compensated case shown in Fig. 3.10(c), the simulation BER was improved when compared to the uncompensated case. For example, it is seen that the BER is approximately 1.5×10^{-8} at the maximum SNR,

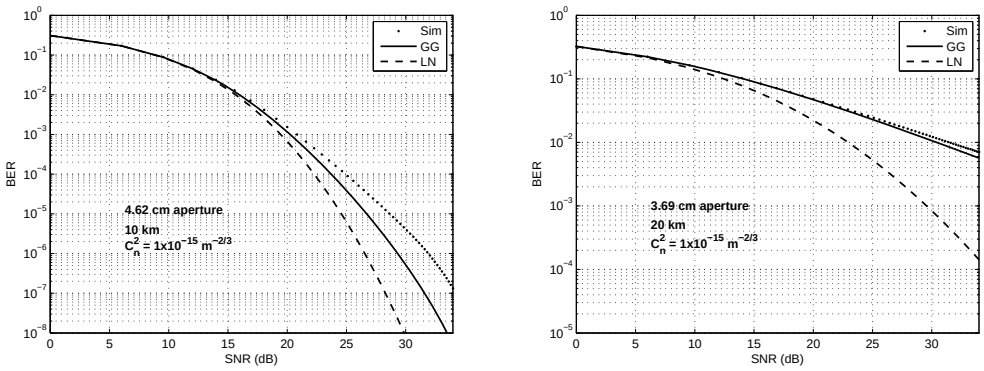

(a) Med. Order

(b) Med. Order

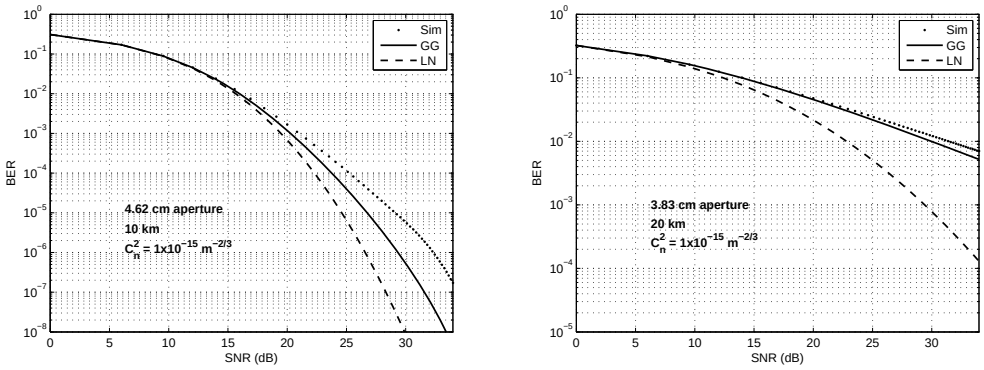

(c) High Order

(d) High Order

Figure 3.11: BER of the laser communication channel for the medium order compensated laser (a, b) and high order compensated laser (c, d) for the ρ_0 diameter aperture and 10 km and 20 km link distances respectively.

which is an improvement of over 5 orders of magnitude. The corresponding PDF plot for this simulation case is shown in Fig. 3.3(c). These results are relatively in line with those by Tyson [8] for a signal-to-noise ratio (SNR) of 21, however the BER for only the 4.62 cm diameter aperture was investigated for the 10 km link in this study whereas Tyson used a 10 cm diameter aperture.

For the 20 km low order compensated case Fig. 3.10(d), the BER showed some improvement when compared to the 20 km uncompensated case. Although, not to the degree shown

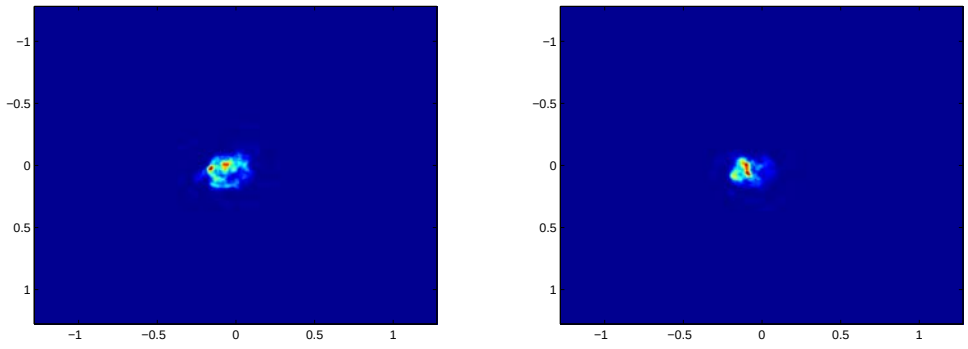

(a) Spot on Transmitter (b) Spot on Receiver

Figure 3.12: Intensity spot at the transmitter (a) and at the receiver (b) for the 10 km link distance showing the non-reciprocal nature of the long distance propagation path.

in the 10 km case. For example, the simulation BER for the compensated case can be seen to be approximately 7.3×10^{-3} at the maximum SNR, which is an slight improvement when compared to the uncompensated case. It can also be seen that the simulation BER follows the gamma-gamma BER closely until around 25 dB in SNR where it diverges only slightly. This is expected since the two PDFs were closely fit as can be seen in the corresponding PDF plot Fig. 3.7(c)

Fig. 3.11 shows the calculated BER of the channel for the medium and high order compensated laser cases. Each case shows the BER calculated for the ρ_0 aperture case for comparison with the plots shown in Fig. 3.10. The corresponding PDF plots for the same parameters can be seen in Figs. 3.4(c) and 3.5(c) for the 10 km medium and high order cases respectively and Figs. 3.8(c) and 3.9(c) for the 20 km medium and high order cases respectively. Inspection of the medium order and high order AO BER plots Figs. 3.11(a) and 3.11(c) and comparing them to the low order AO BER plot Fig 3.10(c) shows

a counter-intuitive result. Specifically, that as the level of complexity of the adaptive optics system increases, so does the BER. Initially we were concerned that perhaps an error in the propagator was causing this issue. However, extensive testing of the propagator has been conducted to verify its accuracy over much longer ranges, and the propagator has also been tested against both theoretical and experimental data [5, 25]. Because of this testing it is necessary to examine other possible explanations for this behavior. We conjecture that the non-reciprocal nature of the path is the underlying issue. Specifically, the wave aberration experienced by a beam traveling from the beacon, which is located at the receiver, to the transmitter, is not identical to the wave aberration acquired by a beam traveling in the opposite direction. Based on the empirical results presented here, we conjecture that the lower order correction provided by the simplest adaptive optics system examined here is a better approximation to the optimal beam to transmit than the beam output by the more complicated adaptive optics systems studied. We note that Enguehard and Hatfield [26] noted that in such non-reciprocal path conditions the optimal beam to transmit is not known. Fig. 3.12 shows evidence of the non-reciprocal nature of the path. Fig. 3.12(a) shows the intensity spot at the transmitter created by the beacon after propagating through the 10 km turbulent atmospheric channel from the receiver, while Fig. 3.12(b) shows the intensity spot on the receiver from a similar beam having passed through the same 10 km turbulent path, but from the opposite direction. It is clearly seen that the intensity spots are not the same thus supporting our conjecture that the path is non-reciprocal and therefore the optimal beam to transmit is unknown.

For the 20 km propagation distance cases, it is seen that there is no improvement from the low order case to the medium order and further to the high order case. Nor, is the same trend of increasing BER shown as in the 10 km cases. This is likely due to the fact that for the 20 km path, the beams in both directions experience even more path integrated turbulence induced phase aberrations than in the 10 km cases and no AO scheme is efficient at reducing these distortions. However, it can be noticed that the spread widens slightly between the simulation data BER and the gamma-gamma BER at the maximum SNR as the WFS order is increased.

3.5 Conclusions

The probability density function (PDF) of adaptively compensated optical power fluctuations at the receiver plane of a free space optical communication link is calculated from wave-optics simulations of a laser after propagating through atmospheric turbulence in order to investigate the changes in the distribution as the number of subapertures in the wavefront sensor is increased. The power was collected by several finite receiving apertures simulataneously and the resulting PDFs are compared to theoretical lognormal and gamma-gamma PDF models. Results show that there is a reduction in the small values of the PDF in the tail for all aperture sizes and scintillation conditions when adaptive optics is incorporated into the lasercom system. In addition, a reduction in the variance of the received optical power from the adaptively compensated laser beam compared to the un-

compensated beam results in a narrower PDF for all aperture sizes. However, there is no significant reduction in the variance and small values in the tail of the PDF for the AO compensated cases begin to appear as the degree of complexity in the AO system was increased for low-order to high-order.

In addition, there is an improvement in the BER, when comparing the low order compensated case to the uncompensated case. This is especially true for the 10 km link distance. However, it can be seen that the BERs for the 10 km link distance cases increase for the medium and high order AO cases. I conjecture that the non-reciprocal nature of the path is the underlying issue. Specifically, the wave aberration experienced by a beam traveling from the beacon, which is located at the receiver, to the transmitter, is not identical to the wave aberration acquired by a beam traveling in the opposite direction. Based on the empirical results presented here, we conjecture that the lower order correction provided by the simplest adaptive optics system examined here is a better approximation to the optimal beam to transmit than the beam output by the more complicated adaptive optics systems studied. For the 20 km AO cases, the BER is improved an almost equal amount for all complexity levels studied. This is likely the result of increased scintillation, due to the longer path and thus no AO complexity scheme will provide the optimal beam to transmit.

It is evident from these results that increasing the order or number of subapertures in the WFS beyond a low order (12 subapertures in this case) does not significantly increase the power falling on a finite receiver aperture, nor does it significantly affect the PDF or BER.

It can therefore be concluded that a low order WFS is adequate for precompensating a laser for propagation through a free space optical channel and that the added expense and complexity of a higher order AO system is unnecessary.

Chapter 4

Temporal power spectral density of the received power for a free space optical channel and coherence times

4.1 Introduction

Atmospheric turbulence along the propagation path can cause severe fluctuations in the optical power within the receiver aperture of a laser communication link. This can cause fading of the received signal known as channel fading where the power randomly dips below a certain threshold, or complete loss of the signal resulting in communications dropouts.

The correlation function obtained from the time series of the received power of a free space optical (FSO) communication link contains information about the coherence time of the received power associated with the optical channel. For channel coding, the coherence time is a measure of the time duration that the received power remains reasonable to allow data symbols to be sent. The coherence interval can then be defined as the channel coherence time normalized by the symbol duration [27]. Channel coherence times can vary widely depending upon many factors including laser wavelength, link distance, receiving aperture size, and turbulence strength. Brookner [9] predicted coherence times ranging from 1.8 ms to 360 ms depending upon those factors mentioned. He used wavelengths of $\lambda = 0.8446\,\mu$m and $\lambda = 10.6\,\mu$m and apertures ranging in diameter from $D \leq 3$ mm to $D = 6$ m. His predictions were based upon measured microwave data and were for a one km horizontal path through what he called "minimum" and "maximum" turbulence and presumably the turbulence strength used in this study $C_n^2 = 10^{-15}\,\mathrm{m}^{2/3}$ falls within this range.

A wave-optics simulation of a collimated, truncated Gaussian laser beam operating at a wavelength of $\lambda = 1550$ nm and propagated distances of 25 km, 50 km, 75 km, and 100 km through atmospheric turbulence was conducted in order to observe the effects of a finite collecting aperture on the channel coherence time in the strong to saturated scintillation regime. In addition to the simulation, received power was collected experimentally from a free space optical communications channel located in Houghton, Michigan in early November, 2009. The nearly horizontal communication link spans 3.1 km at an altitude

of approximately 30 m, partially over water. Optical power was collected at the receiver by apertures with various diameters from a 13 mw semi-conductor laser operating at a wavelength of $\lambda = 808$ nm.

The correlation function $\Gamma_x(\tau)$ for both the simulation and experimental data was calculated from the temporal power spectral density (PSD) $S_x(\nu)$ of the data and the channel coherence time was subsequently estimated from $\Gamma_x(\tau)$. The temporal power spectra of various optical beam wave quantities has been studied extensively in the literature [4, 28, 29, 30, 31, 32, 33, 34, 35, 36, 37, 38, 39, 16].

Aperture averaging refers to the smoothing of optical power fluctuations and occurs when a finite size receiver aperture that is larger than the correlation width of the beam wave is used to collect the laser light, which results in a reduction of the scintillations when compared to point size apertures [2]. Aperture averaging effects on optical scintillation has been the topic of much research [16, 1, 20, 21, 17, 18, 5].

This study seeks to investigate the channel coherence times associated with long propagation distances through the turbulent atmosphere. In addition, the change in the coherence time for a given link distance as the receiver aperture diameter is increased is also investigated. To our knowledge, this is the only study investigating the channel coherence times for such long propagation distances, whether in simulation or experimental.

Results from both simulation data show that the coherence time increases as the receiving

aperture diameter is increased. Also, as the communication link distance increases the coherence time increases for finite apertures. This is most likely due to the increased size of the speckles in the pupil plane of the receiver of the communications link. The implications of this may mean that some practical measure of tradeoff could be obtained between link distance and aperture size in terms of cost and performance in the design of a free space optical communication link. The experimental results, although not directly comparable to the simulation results due to differences in link distance, receiver aperture size, and laser wavelength, nevertheless demonstrate the trend of increasing coherence time with aperture size shown in the simulation results.

The remainder of the chapter is organized as follows: In section 2, a description of how temporal intensity fluctuations affect a digital laser communication system and how channel coding is used to overcome these effects. In section 3, a detailed description of the simulation is presented. In section 4, the experimental setup and data collection along with the calculation of the channel coherence time is given. In section 5, both simulation and experimental results and discussion are presented. In section 6, conclusions are given.

4.2 Background

4.2.1 Temporal Fading Channel

Atmospheric turbulence causes random intensity fluctuations called scintillation at the receiver plane of a FSO communication link. Scintillation can lead to fading of the received signal below a prescribed threshold required for reliable detection of the signal [2]. One way to improve a lasercom signal against scintillation effects is through the use of error correction coding and interleaving. Anquita et al. [40] calculated the channel capacity of a FSO communication link for various atmospheric and scintillation conditions. In addition, they evaluated two error correction codes by plotting the bit error rate (BER) versus the signal to noise ratio (SNR) and comparing to Reed-Solomon (RS) codes for a wide range of scintillation conditions. Their study involved a point receiver and an atmospheric channel modeled as uncorrelated ergodic. In other words, each realization of the atmosphere along the propagation path was independent from the next, so that the channel coherence time τ_c corresponds to a single symbol duration. Actual atmospheric channel statistics do not vary so fast in time. Xu et al. [27] took advantage of this in their study again involving comparing several error correction codes to RS codes and a no-coding case. Their study again involved a point receiver but an atmospheric channel that was modeled as a block fading channel where fades are constant during a fading block corresponding to the coherence interval. The coherence interval is defined as the channel coherence time normalized by the

symbol duration (τ_c/T_s). However, it is known that channel coding alone isn't sufficient to overcome channel fading [27]. Aperture averaging is another technique used to reduce the effects of scintillation at the receiver plane. This study investigates the channel coherence time measured from the correlation function of optical power fluctuations for long distance lasercom links. Knowledge of the channel coherence time is useful in accurately modeling the atmosphere when studying FSO communication links.

4.2.2 Detection of received signal

In the following discussion, intensity modulation with direct detection (IM/DD) using on-off keying (OOK) modulation is considered as this is the most commonly used system [27]. In OOK modulation, each bit symbol is transmitted with a laser pulsed on or off with duration T_s [2]. The presence of a pulse represents a binary bit 1 and the lack of a pulse represents a binary bit 0 [27]. The received electrical signal after conversion from optical power to electrical power can be expressed at any instant in time as [41]

$$r_e(t) = \eta\,(I_s(t) + I_a) + n(t), \tag{4.1}$$

where I_s is the received intensity signal, I_a is the remaining ambient light intensity after filtering to remove optical wavelengths other than the desired optical wavelengths, n is considered additive white Gaussian noise (AWGN) with zero mean and variance σ_n^2 and is

independent of I_s. The conversion coefficient η can be expressed as [41]

$$\eta = \gamma T_0 \cdot \frac{e\lambda}{hc}, \tag{4.2}$$

where γ is the quantum efficiency of the photodetector, T_0 is the receiver integration time, e is the electric charge in coulombs, λ is the signal wavelength, h is Planck's constant, and c is the speed of light in a vacuum. It can be assumed that I_s and I_a are constant over T_0 [41] and that I_a can be perfectly cancelled by subtracting the bias thus reducing the expression for the received signal to [27]

$$r(t) = r_e(t) - I_a = \eta I_s(t) + n(t). \tag{4.3}$$

4.3 Simulation

A numerical simulation of an initially collimated and truncated Gaussian laser beam propagating through Kolmogorov atmospheric turbulence in which inner scale l_0 and outer scale L_0 effects were ignored was developed to obtain the temporal correlation function of the laser power captured at the receiver plane of a FSO communication link. The laser was propagated over distances of 25 km, 50 km, 75 km, and 100 km through homogeneous and isotropic atmospheric turbulence with a constant refractive index structure parameter C_n^2 such as might be experienced along a horizontal propagation path.

An expanding propagation grid simulation scheme was developed in order to reduce propagation time in the simulation [25]. This was necessary since with the long propagation distances involved, number and size of the phase screens necessary in the simulation, and the number of data points necessary to accurately calculate the PSD and subsequently the correlation distribution made conventional simulations involving a large propagating grid impractical. The simulated propagation scheme is described as follows. The laser is propagated 25 km through the turbulent atmosphere using a $N_{Grid} \times N_{Grid}$ propagation grid, where $N_{Grid} = 700$ pixels. At which time the optical power is collected and the grid is expanded to $N_{Grid} = 1024$ pixels. The field is then allowed to continue propagating another 25 km. This process is repeated for $N_{Grid} = 1600$ pixels and again for $N_{Grid} = 1900$ pixels until the field reaches 100 km where the final collection of the optical power occurs.

Several factors were involved in choosing the sizes of the propagation grids in the simulation. First, the screen size must comply with the simulation parameter guidelines outlined by Rao [22] and Belmonte [23]. These guidelines are discussed below. Second, they must be large enough to allow for the cross-wind shift of the grid through 500 iterations. Third, they must be kept as small as possible to minimize computation time.

The guidelines provided by Rao [22] and Belmonte [23] were followed closely in the determination of the simulation parameters. A summary of these guidelines is given as follows.

1) The number of phase screens or propagation steps N_{Step} along the propagation path is dictated by the Rytov variance, which is a measure of the strength of scintillation expe-

rienced by a plane wave as it propagates through the atmosphere in moderate to strong turbulence and is considered a measure of optical turbulence strength when extended to the strong fluctuation regime [15]. The Rytov variance for a constant C_n^2, such as might be experienced along a horizontal propagation path, is defined as [2]

$$\sigma_R^2 = 1.23 C_n^2 k^{7/6} L^{11/6}. \tag{4.4}$$

where L is the propagation distance, $k = 2\pi/\lambda$ is the optical wavenumber, and λ is the laser wavelength. The Rytov variance for each propagation step $\sigma_R^2(\Delta z)$ must be less than 10 % that of the Rytov index for the total propagation path $\sigma_R^2(L)$. Also, $\sigma_R^2(\Delta z)$, which is approximately equal to the scintillation index σ_I^2 in weak turbulence regimes must be less than or equal to 0.1. The scintillation index, which is the normalized variance of irradiance fluctuations can be defined as [1]

$$\sigma_I^2 = \frac{\langle I^2 \rangle - \langle I \rangle^2}{\langle I \rangle^2}, \tag{4.5}$$

where I is the irradiance measured at the receiver plane and $\langle \cdot \rangle$ denotes an ensemble average. The finite aperture counterpart to the scintillation index also called the flux variance of irradiance fluctuations can be defined as [2]

$$\sigma_I^2(D) = \frac{\langle P^2 \rangle - \langle P \rangle^2}{\langle P \rangle^2}, \tag{4.6}$$

where P is the received optical power and D is the diameter of the circular receiver diameter.

2) To determine the computational grid sampling interval Δx, the Fresnel zone $l_{FZ}(\Delta z)$ was computed for each propagation step N_{Step}, which is the distance between phase screens. The Fresnel zone can be defined as [2]

$$l_{FZ}(L) = \sqrt{L/k}. \tag{4.7}$$

Then Δx was held within the confines of a lower limit and an upper limit dictated by l_{FZ} as

$$l_{FZ}(L)/\sqrt{N_{Step}N_{Grid}} < \Delta x < l_{FZ}(\Delta z), \tag{4.8}$$

where N_{Grid} is the number of pixels along one side of the propagation grid and considerations for determining the proper size of N_{Grid} are outlined below.

3) The size of the physical screen must be large enough to contain the naturally diverging laser beam spot during screen-to-screen propagation and prevent wrap-around errors from occurring. Also, the screen must be larger than the scattering disk, which is defined in terms of the first Fresnel zone as [22]

$$l_{SD} = l_{FZ}^2/\rho_0, \tag{4.9}$$

where ρ_0 is the atmospheric coherence radius for a Gaussian wave. The expression for ρ_0

can be found in [2]. Another consideration when determining the size of the sampling grid can be found in [23], where Belmonte states that $N_{Grid} \geq nq$, where q is a dimensionless quantity equivalent to the scattering disk divided by the Gaussian wave atmospheric coherence diameter r_0, and $n > 1$. Belmonte notes that a value of $n = 3$ or 4 will prevent the screen from experiencing any aliasing during propagation.

The laser propagation simulation was accomplished by propagating the complex field through locally homogeneous and locally isotropic atmospheric turbulence using a Fresnel propagator from the Matlab toolbox AOTools [24]. The turbulent atmosphere was simulated by dividing the total propagation distance into several smaller distances, each followed by a randomly generated phase screen. The sample spacing Δx was chosen to be 6 mm between each grid point for all cases of scintillation, making the edge dimension of each physical grid size in the expanding grid simulation 4.20 m, 6.14 m, 9.00 m, and 11.40 m respectively. The Kolmogorov turbulence spectrum phase screen generator from the Matlab toolbox AOTools [24] was used and inner and outer scale effects were ignored. The total number of phase screens were divided evenly along the propagation path, however the first and last phase screens were placed half the distance $\Delta z/2$ of the propagation step from the transmitter and receiver apertures respectively. Twelve independent phase screens were created to simulate the turbulence along the path of each 25 km leg of the communication link making a total of 48 phase screens along the 100 km propagation path.

Taylor's frozen turbulence hypothesis was used in the simulation, where variations in the

turbulence statistics resulting from turbulent eddies evolve over a much longer timeframe than the motion of the atmosphere caused by the mean wind speed [2]. This in effect results in an envelope of atmosphere moving transverse to the propagation path carrying the turbulent eddies within allowing us to greatly simplify the simulation. A uniform cross-wind velocity of $V_{\perp} = 6$ m/s is assumed along the entire propagation path. A time-step of 1 ms between each data point collected means the turbulent atmosphere moves 6 mm across the propagation path between each propagation event. We define propagation event as the process of propagating the laser 100 km through the atmospheric channel and the collection of optical power at each 25 km leg along the way. Therefore, with a computational grid sample spacing of $\Delta x = 6$ mm, the propagation grid shifts 1 pixel in the x-direction between each event. This is accomplished with the help of a software tool from the Matlab toolbox AOTools [24] that allows the propagation grid to circularly shift between each propagation event within the propagation loop. In addition, each column of pixels within the grid was only allowed to pass across the screen once during a cycle. This ensured that the laser never propagated through the same turbulence twice.

Ideally, the simulation would continue with one set of phase screens for the duration of the sampling. But, due to limitations imposed by the finite size of the propagation grid this was not possible. The propagation grid was allowed to shift 500 times for each group of phase screens created to represent the turbulent atmospheric channel. With a cross-wind velocity of $V_{\perp} = 6$ m/s, $\Delta x = 6$ mm, and 1 pixel shift per propagation event meant that 500 shifts represents a wind drift of 3 meters across the screen and 0.5 seconds of sampling before

another group of phase screens was created and the process repeated.

After each 25 km propagation leg, the optical power was captured by seven separate receiver apertures of different diameters simultaneously. The aperture diameters are 0.68 cm, 5 cm, 15 cm, 25 cm, 50 cm, 1 m, and 1.5 m. Finally, after 55,000 data points were collected the temporal PSD was calculated from blocks of 500 data points taken from the time-series and subsequently averaged together. Next, the temporal correlation function was obtained from an inverse Fourier transform of the PSD. The coherence time was then calculated as the half-width of the correlation distribution at the $1/e$ value.

4.4 Experiment, System Design, and Data Collection

The FSO communication channel described in this study consists of a laser, telescope receiver, adaptive optics, photo detector amplified (PDA) and a CCD camera. The laser transmitter incorporates an 808 nm laser diode module with an adjustable power control to obtain the desired flux density at the receiver. The front-sensing receiver is located 3046 m away from the transmitter. In order to accurately measure the turbulence-induced distortions, the wave front sensor must be precalibrated. Both the transmitter and the receiver are at an approximate elevation of 250 m above mean sea level. The portion of the propagation path that is over water has a strong influence on the index of refraction fluctuations, depending on the time of day and season of the year and therefore allows exploring a wide

range of turbulence conditions. Next, the details of the experimental system design of the transmitter and the receiver are presented.

4.4.1 Transmitter

The transmitter setup is given in Fig. 4.1. Fig. 4.1 shows all the components integrated in the transmitter and Fig. 4.2 provides the view from the top and demonstrates all possible directions of adjustment required for the proper alignment of the transmitter and the receiver. The transmitter implements a semiconductor laser operating at a wavelength of $\lambda = 808$ nm and the laser power is adjustable from 0.5 to 13mW. In order to provide a precise alignment of the transmitter and the receiver, a targeting scope was incorporated in the transmitter assembly. Before being brought to the field, the targeting scope is prealligned with the laser source in the laboratory environment[42]. The laser source mounts on the secondary rotation stage which permits the alignment of the laser and the targeting scope to the same point in space. The laser-targeting scope assembly is placed on a two-stage base consisting of a rail with a slider and a primary platform rotation stage. This base assembly provides an additional four levels of freedom (up and down, left and right) for the final alignment of the transmitter and the receiver.

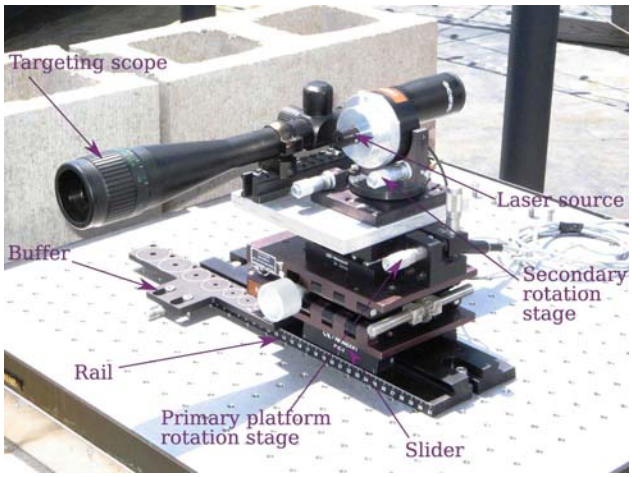

Figure 4.1: Transmitter:Extended view.

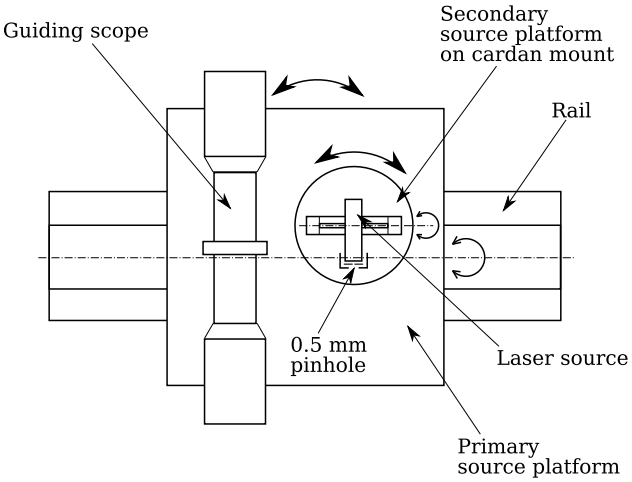

Figure 4.2: Transmitter:View from the top shows directions of adjustments required for proper alignment of the transmitter with the receiver

4.4.2 Receiver

The two-channel receiver shown in Fig. 4.3 incorporates a Schmidt-Cassegrain telescope with an entrance pupil diameter $D = 0.28\,\mathrm{m}$ with a center obscuration of 0.09 m and has a focal distance $f = 2.8\,\mathrm{m}$. On the exit pupil of the telescope, the converging beam falls on the beamsplitter 1 and splits into WFS and visual/PSF channels. The portion of the

Figure 4.3: Receiver:Extended view

laser radiation that is diverted through the WFS is used to estimate the Fried parameter r_0 and subsequently the turbulence refractive index structure parameter C_n^2, which is assumed constant along the horizontal propagation path. The procedure for these estimations is provided in [42]. A detailed view of the WFS-CCD camera system assembly is shown in Fig. 4.4.

In this work, attention was placed on simultaneous data gathering from the WFS channel and the visual channel equipped with the PDA (Thorlabs PDA-100A) silicon photo-diode. The beam entering the visual/PSF channel is focused on the PDA using a relay lens with a focal length $f_r = 75$mm. The photo-diode with a responsivity of 0.5 amps/watt at 808 nm amplifies the current with a transimpedance gain of 50 dB and the resulting voltage data was collected and stored on a computer for future processing.

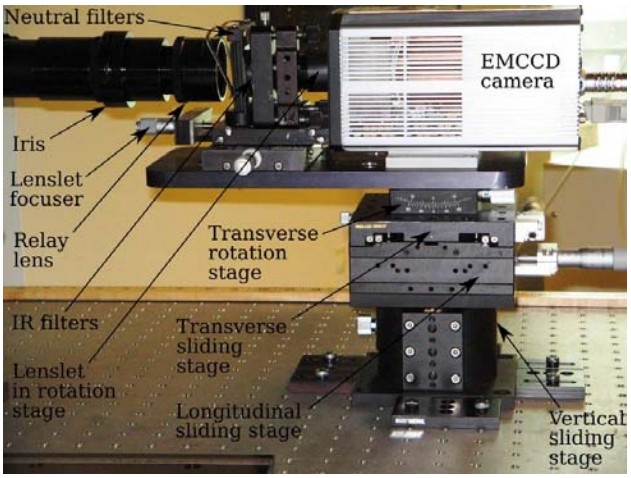

Figure 4.4: Receiver:Details of the WFS assembly

4.4.3 Data Collection

The data was collected in early November 2009. The weather conditions were overcast but otherwise dry and cool with a temperature of approximately 2 ^{o}C during the time that measurements were taken. A steady wind with a velocity of 5.81 m/s was blowing from the north diagonally across the propagation path resulting in a cross-wind velocity $V_{\perp}$ of approximately 5.67 m/s.

Light was first captured with the full telescope pupil, which had a diameter of 28 cm with a 9 cm diameter center obscuration leaving a total receiving area of $552.14\,\mathrm{cm}^2$, which results in an effective circular pupil diameter of approximately 132.57 mm. An opaque foam stop placed in front of the entrance pupil with several different diameter cutouts (which could be removed and replaced as needed) comprised the remaining receiver apertures. The diameters of these apertures were 109.84 mm, 69 mm, 36 mm, and 9 mm. Attempts

were made to obtain data with a smaller aperture but were unsuccessful.

300,000 data points were collected for each aperture at a time-step of 1 ms between each measurement, after which 10,000 data points were collected with the laser off to obtain background light measurements. The mean of these background data were subsequently subtracted from each data point in the power measurement during post processing. The process of collecting the power data and background data therefore took just over five minutes to complete for each aperture.

4.4.4 Coherence Time Calculation

Optical power was collected at the receiver of an FSO communication link in both the simulation and experimental cases. The power was collected at the receiver at intervals of 1 ms resulting in 55,000 individual data points for each simulation case and 300,000 data points for the experimental case. The time series of optical power was then divided into N lengths of $M = 500$ data points for each case. Next, the temporal power spectral density was obtained by squaring the modulus of the Fourier transform of each 500 data point block $x(t)$ of the time series. The average value $\langle x(t) \rangle$ had previously been subtracted from all the values in $x(t)$. Then the PSDs were averaged together in order to estimate the temporal PSD.

$$S_x(\nu) = \frac{1}{N} \sum_{i=1}^{N} \left| FT \left[x_i(t) - \langle x_i(t) \rangle \right] \right|^2 . \tag{4.10}$$

The correlation function was obtained from the inverse Fourier transform of the PSD.

$$\Gamma_x(\tau) = FT^{-1}\left[S_x(\nu)\right]. \tag{4.11}$$

The coherence time of the optical channel was then estimated by measuring the half-width of the resulting correlation distribution at the $1/e$ value.

4.5 Results and Discussion

Table 4.1: Table 1. Coherence times per aperture diameter for simulated data

Aper. Dia. (cm)	0.68	5	15	25	50	100	150
Distance	τ_c (ms)	τ_c (ms)	τ_c (ms)	τ_c (ms)	τ_c (ms)	τ_c (ms)	τ_c (ms)
25 km	5.493	6.620	9.202	11.460	15.820	19.920	23.250
50 km	6.902	9.406	13.770	16.460	20.100	24.490	28.060
75 km	6.407	12.080	19.540	23.570	26.880	32.180	34.560
100 km	5.232	13.360	27.550	34.580	41.290	46.320	48.840

4.5.1 Simulation Results

A list of the coherence times calculated from the correlation function for each propagation distance and the respective receiver aperture diameter is given in Table 1. It is observed that for all link distances involved the coherence time increases as the aperture size increases. This can be attributed to the smoothing effect of a finite receiver aperture in which the

fastest fluctuations in the received power are averaged out causing a reduction in the flux variance. This reduction in the power fluctuations results in longer coherence times for the channel with an increasing receiver aperture diameter. An example of the power spectral density plotted for a single link distance and various aperture diameters is shown in Fig. 4.5(a). The example shown is for the 25 km link and apertures diameters of 0.68 cm, 5 cm, 15 cm, and 50 cm. It can be seen that the PSD narrows as the aperture diameter increases, indicating that the coherence time measured from the associated correlation function is increasing. Because there are no other references to draw upon for comparable results for such long propagation distances, it is difficult to make a judgement about the accuracy of the results shown in Table 1. However, the coherence times, although for much longer distances, are in line with those predicted by Brookner [9].

Interference causes light and dark correlation patches called speckle within the pupil plane of the receiver. These speckles have a lateral intensity coherence length ρ_I [43], which tends to increase in size as the link distance is increased. The speckle size can be roughly estimated as [43]

$$\rho_I \approx 0.4\sqrt{L\lambda}, \tag{4.12}$$

where L is the link distance and λ is the laser wavelength. This means that for an increasing link distance the coherence time associated with larger correlation areas (speckle) would therefore increase. This is consistent with the coherence times observed for the apertures with diameters of 5 cm and larger. It is noted however that the coherence times associated

with the small aperture do not change greatly for all link distances and in fact decrease slightly for the 75 km and 100 km link distance cases. An example of the power spectral density plotted for a single aperture diameter and all link distances is shown in Fig. 4.5(b). The example shown is for the 5 cm aperture diameter. It can be seen that the PSD narrows as the link distance increases, indicating that the coherence time measured from the associated correlation function is increasing.

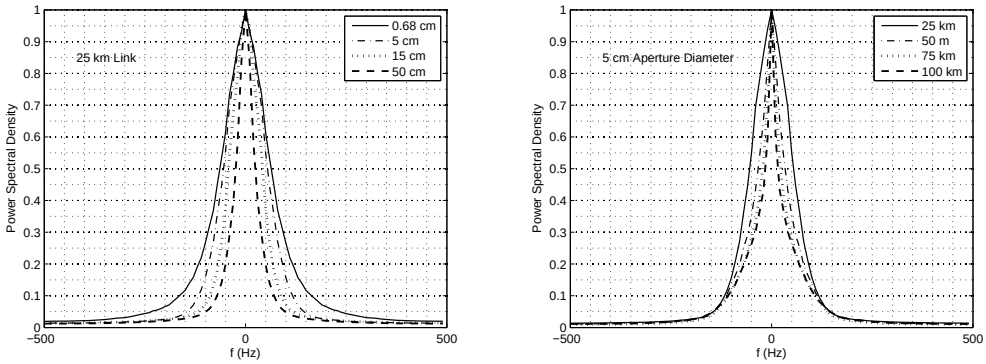

(a) 25 km link (b) 5 cm aperture

Figure 4.5: PSD for 25 km link distance and aperture diameters 0.68 cm, 5 cm, 15 cm, and 50 cm (a) and PSD for 5 cm aperture and all link distances (b) showing that in both cases the PSD narrows, indicating that the coherence time measured from the associated correlation function is increasing

4.5.2 Experimental Results

The coherence time was calculated from the correlation function in the manner described in the previous section from optical power measurement data collected by several receiving apertures of various diameters at the receiver plane of a 3 km laser communication link in the weak scintillation regime. These coherence times are given in Table 2. As can be seen

from the table the coherence time increases as the aperture diameter is increased from 9 mm to 132.57 mm. This is the same trend shown in the simulation results. The results, although perhaps not directly comparable to Brookner [9] due to the longer link distance and presumably weaker turbulence encountered in this experiment, are nevertheless in line with those predicted in [9]. Since the link distance is fixed, no conclusions can be drawn about the effect that propagation distance has on the coherence time of the optical channel. Although, the experimental results are not directly comparable to the simulation results, due to differences in link distance and receiver aperture size a trend can be seen in the increasing coherence time with aperture size. In addition, the coherence times for the experimental case are shorter than for relatively comparable aperture diameters in the simulation case. This can likely be attributed to the smaller speckle size in the receiver aperture that is expected for the short link distance.

Table 4.2: Table 2. Coherence times per aperture diameter for experimental data

Aper. Dia.	9 mm	36 mm	69 mm	109.84 mm	132.57 mm
τ_c (ms)	1.4856	2.945	3.990	4.305	4.210

4.6 Conclusions

A wave-optics simulation of an initially collimated and truncated Gaussian laser beam propagated 100 km through the turbulent atmosphere was conducted and optical power was

collected along the way at intervals of 25 km. The power was captured by several receiver apertures of diameters ranging from 0.68 cm up to 1.5 m. The temporal power spectral density was then calculated from the time sequence of optical power and the coherence time of the optical channel was subsequently obtained from the width of the associated correlation function.

It was found that the coherence times increased as the aperture diameter was increased for each 25 km leg of the optical communication link. It was also noticed for finite apertures of 5 cm and larger that the coherence time in all cases increased as the propagation distance increased. It is thought that this is due to the increasing speckle size in the pupil plane of the receiver aperture as the link distance is increased. The implications of this is that some practical measure of tradeoff could be obtained between link distance and aperture size in terms of cost and performance in the design of a free space optical communication link. These results, although not directly comparable, due mainly to the longer propagation distances in this study, are nevertheless in line with those predicted by Brookner [9] for a much shorter link.

The correlation function was obtained in a similar manner for the experimental case as was for the simulation case. The coherence time was then calculated for each of the respective receiver apertures. The experimental results, although not directly comparable to the simulation results due to differences in link distance, receiver aperture size, and laser wavelength, nevertheless demonstrate the trend of increasing coherence time with aperture size

shown in the simulation results. This is consistent with the trend shown in the simulation. Longer coherence times with aperture size means that more bits can be transmitted through the channel with a larger receiver aperture. However, again there is a tradeoff between the cost of a larger receiver aperture and the performance of the FSO communication link.

Chapter 5

Conclusions

5.1 Summary of Dissertation

We have presented a study of statistics of the received power for a free space optical communication system for long propagation distances under a variety of turbulence conditions from weak to saturated. In the study detailed in chapter 2, we characterize the probability distribution of the received power by comparing the PDF of the received power to the lognormal and gamma-gamma PDF models. A wave-optics simulation was developed to model an FSO system with link distances of 50 km, 75 km, and 100 km and path averaged turbulence strengths of $C_n^2 = 1 \times 10^{-18}$ m$^{-2/3}$ to $C_n^2 = 1 \times 10^{-15}$ m$^{-2/3}$, which resulted in Rytov variances of $\sigma_R^2 = 0.03$ to $\sigma_R^2 = 92.41$, or in other words, very weak to saturated

scintillation conditions. A collimated and spatially trucated Gaussian beam with a wavelength of $\lambda = 1.55\,\mu$m was the optical beam transmitted and the power was received by apertures of diameter 5.6 mm, $\rho_0/2$, ρ_0, and $3\rho_0/2$, where ρ_0 is the atmospheric coherence radius, in order to characterize the PDF as it evolves with the increasing aperture size and changing scintillation conditions. The PDF is comprised of 30,000 data points taken from independant realizations of the laser propagation through the atmospheric channel.

The study detailed in chapter 3 expands upon what was learned in the study detailed in chapter 2 and incorporates adaptive optics into the FSO system. A wave-optics simulation was developed to model an FSO system where the outgoing beam is precompensated before being transmitted through the turbulent channel in the moderate scintillation regime. A brief summary of the system is as follows. A laser beacon is situated at the receiver and is propagated back towards the transmitter, where the signal enters a Hartman wavefront sensor. The WFS measures the phase aberrations in the beacon wavefront then sends that information to the DM where it incorporates the conjugate of the beacon wavefront in the surface of the mirror. These corrections are then imparted to an outgoing beam by reflection, where upon the laser beam is then transmitted through the channel back to the receiver. The complexity of the AO system was increased from low-order to medium-order then to high-order. Low-order refers to a WFS pupil with twelve subapertures, medium-order refers to a WFS pupil with 24 subapertures, and high-order refers to a WFS pupil with 52 subapertures. The configurations of these can be seen in Fig. 3.1 in section 3.2.2.3 of chapter 3. At the receiver, the power is collected by apertures of diameters similar

to those used in the study of the uncompensated laser beam detailed in chapter 2. The transmitted laser beam is a collimated spatially truncated Gaussian beam with a wavelength of $\lambda = 1.55\,\mu$m as in the previous study. The link distances were 10 km and 20 km and the turbulence strength was fixed at $C_n^2 = 1 \times 10^{-15}$ m$^{-2/3}$, which resulted in Rytov variances of $\sigma_R^2 = 1.36$ and $\sigma_R^2 = 4.83$ respectively. The PDF was then calculated using the same number of propagation realizations as in the previous study.

The study detailed in chapter 4 investigates the temporal power spectral density of the received power from a FSO communication link and subsequently the resulting channel coherence time measured from the associated correlation function. A wave-optics simulation of a collimated, truncated Gaussian laser beam operating at a wavelength of $\lambda = 1550$ nm and propagated distances of 25 km, 50 km, 75 km, and 100 km through atmospheric turbulence was conducted in order to observe the effects of a finite collecting aperture on the channel coherence time in the strong to saturated scintillation regime. In addition to the simulation, received power was collected experimentally from a free space optical communications channel located in Houghton, Michigan in early November, 2009. The nearly horizontal communication link spans 3.2 km at an altitude of approximately 30 m, partially over water. Optical power was collected at the receiver by apertures with various diameters from a 13 mw semi-conductor laser operating at a wavelength of $\lambda = 808$ nm.

5.2 Summary of Key Results

Both lognormal and gamma-gamma PDF models provide a good fit to the distribution for all aperture sizes studied in the very weak scintillation regime $\sigma_R^2 < 0.55$. However, as the scintillation increased the PDF widened due to the increase in the variance of the power. The gamma-gamma PDF model became a better fit to the distribution than the lognormal and continued to be a better fit through the moderate scintillation regime $\sigma_R^2 \leq 5$. In the strong scintillation regime $\sigma_R^2 > 5$ the lognormal PDF model became a better fit for apertures larger than or equal in size to the coherence radius ρ_0 and gamma-gamma PDF model continued to be a better fit to the distribution for apertures very much smaller than ρ_0 or for point apertures. This is consistent with previously held theory in the strong scintillation regime [1].

A low-order AO system is adequate for compensation of a transmitted laser beam under the conditions of a non-reciprocal path, that is, a path where the turbulence induced phase aberrations experienced by a beam travelling in one direction of the link is not the same as those experience by a beam travelling in the opposite direction. In the 10 km link distance case the PDFs experienced a slight increase in the small PDF values of the tail as the AO complexity was increased, which led to higher BER values for increasing complexity. In the 20 km link distance case, the PDFs remained nearly unchanged as the AO complexity was increased and the BER values also remained unchanged. This was likely due to the increased scintillation for a longer link distance resulting in a path in which no AO

complexity would provide the correction for an optimal beam to transmit. Thus the low-order AO complexity is deemed adequate for compensation of a transmitted beam for both link distance cases. The PDF results are in line with those shown by Tyson [7], however Tyson's study only incorporated tip/tilt AO correction. These results incorporate low-order, medium-order, and high-order degrees of AO complexity. The BER results for the 10 km link are relatively in line with those by Tyson [8] for a signal-to-noise ratio (SNR) of 21, however the BER for only the 4.62 cm diameter aperture was investigated in this study whereas Tyson used a 10 cm diameter aperture.

The coherence times increased as the aperture diameter was increased for all link distances. This is due to the averaging of the irradiance fluctuations that occurs in a finite receiver aperture diameter, which causes a smoothing effect to the fluctuations resulting in a reduction of the scintillation. This reduction in scintillation allows for an increase in the coherence time. In addition, the coherence times increased as the link distance increased for each finite aperture. This is likely due to the increasing speckle size in the pupil plane of the receiver aperture as the link distance is increased. The implications of this is that some practical measure of tradeoff could be obtained between link distance and aperture size in terms of cost and performance in the design of a free space optical communication link.

The experimental results, although not directly comparable with the simulation results due to the much shorter propagation length in the experiment, show the trend of increasing

coherence time with receiver aperture diameter. This is consistent with the trend shown in the simulation and thus it is shown that the simulation and experiment support one another. Longer coherence times with aperture size means that more bits can be transmitted through the channel with a larger receiver aperture. However, again there is a tradeoff between cost of a larger receiver aperture and performance of the FSO communication link.

5.3 Future Work

One area of future work might involve a similar study to that detailed in 2 with a real-world FSO communication system investigating the probability distribution of received power under a variety of scintillation conditions with apertures similar in size to those used here. Simulations could also be developed to model paths in a weaker scintillation regime than those detailed in 3 in order to evaluate the PDF of received power for a compensated beam transmitted through a channel that is reciprocal. Also, the experiment detailed in chapter 4 involved a lasercom link of 3.1 km. However, in order to better verify the results of the simulation, also detailed in chapter 4, a variety of link distances could be investigated. Another possible study could be to investigate the probability distribution of the received power for a slow fading channel such as was simulated in the PSD study detailed in chapter 4.

References

[1] F. S. Vetelino, C. Young, L. C. Andrews, and J. Recolons. Aperture averaging effects on the probability density function of irradiance fluctuations in moderate-to-strong turbulence. *Appl. Opt.*, 46:2099–2108, 2007.

[2] L. C. Andrews and R. L. Phillips. *Laser Beam Propagation through Random Media*. SPIE Press, 2nd edition, 2005.

[3] M. C. Roggemann and B. M. Welsh. *Imaging Through Turbulence*. CRC Press, 1996.

[4] R. S. Lawrence and J. W. Strohbehn. A survey of clear-air propagation effects relevant to optical communications. *Proc. IEEE*, 58:1523–1545, 1970.

[5] S. D. Lyke, D. G. Voelz, and M. C. Roggemann. Probability density of aperture-averaged irradiance fluctuations for long range free space optical communcation links. *Appl. Opt.*, 48:6511–6527, 2009.

[6] J. H. Churnside and R. J. Hill. Probability density of irradience scintillations for strong path-integrated refractive turbulence. *J. Opt. Soc. Am. A*, 4:727–733, 1987.

[7] R. K. Tyson and D. E. Canning. Indirect measurement of a laser communications bit-error-rate reduction with low-order adaptive optics. *Appl. Opt.*, 42:4239–4243, 2003.

[8] R. K. Tyson. Bit-error rate for free-space adaptive optics laser communications. *J. Opt. Soc. Am. A*, 19:753–758, 2002.

[9] E. Brookner. Atmosphere propagation and communication channel model for laser wavelengths. *IEEE Trans. Comm. Tech.*, COM-18:396–416, 1970.

[10] S. M. Flatt*é*, C. Bracher, and G. Wang. Probability density functions of irradiance for waves in atmospheric turbulence calculated by numerical simulation. *J. Opt. Soc. Am. A*, 11:2080–2092, 1994.

[11] R. J. Hill and R. G. Frehlich. Probability distribution of irradiance for the onset of strong scintillation. *J. Opt. Soc. Am. A*, 14:1530–1540, 1997.

[12] J. H. Churnside and R. G. Frehlich. Experimental evaluation of log-normally modulated rician and *IK* models of optical scintillation in the atmosphere. *J. Opt. Soc. Am. A*, 6:1760–1766, 1989.

[13] J. H. Churnside. Joint probability-density function of irradiance scintillations in the turbulent atmosphere. *J. Opt. Soc. Am. A*, 6:1931–1940, 1989.

[14] M. A. Al-Habush, L. C. Andrews, and R. L. Phillips. Mathematical model for the ir-

radiance pdf of laser beam propagation through turbulent media. *Opt. Eng.*, 40:1554–1562, 2001.

[15] M. A. Al-Habush, L. C. Andrews, and R. L. Phillips. Theory of optical scintillation: Gaussian-beam wave model. *Proc. SPIE*, 4678:91–101, 2002.

[16] L. C. Andrews, R. L. Phillips, and C. Y. Hopen. Aperture averaging of optical scintillations: power fluctuations and the temporal spectrum. *Waves Random Media*, 10:53–71, 2000.

[17] J. H. Churnside and S. F. Clifford. Log-normal rician probability-density function of optical scintillations in the turbulent atmosphere. *J. Opt. Soc. Am. A*, 4:1923–1930, 1987.

[18] J. H. Churnside. Aperture averaging of optical scintillations in the turbulent atmosphere. *Appl. Opt.*, 30:1982–1994, 1991.

[19] Z. Azar, M. Loebenstein, G. Applebaum, E. Azoulay, U. Halavee, M. Tamir, and M. Tur. Aperture averaging of the two-wavelength intensity covariance function in atmospheric turbulence. *Appl. Opt.*, 24:2401–2407, 1985.

[20] F. S. Vetelino, B. Clare, K. Corbett, K. Grant C. Young, and L. C. Andrews. Characterizing the propagation path in moderate to strong optical turbulence. *Appl. Opt.*, 45:3534–3543, 2006.

[21] F. S. Vetelino, C. Young, and L. C. Andrews. Fade statistics and aperture averaging for

gaussian beam waves in moderate-to-strong turbulence. *Appl. Opt.*, 46:3780–3789, 2007.

[22] R. Rao. Statistics of the fractal structure and phase sinularity of a plane light wave propagation in atmospheric turbulence. *Appl. Opt.*, 47:269–276, 2008.

[23] A. Belmonte. Feasibility study for the simulation of beam propagation: consideration of coherent lidar performance. *Appl. Opt.*, 39:5426–5445, 2000.

[24] T. J. Brennan and P. H. Roberts. Aotools the adaptive toolbox users guide. The Optical Sciences Company Website, http://www.tosc.com/downloads/AOToolsUG.pdf, 2006.

[25] D. G. Voelz and M. C. Roggemann. Digital simulation of optical diffraction: revisiting chirp function sampling criteria and consequences. *Appl. Opt.*, 48:6132–6142, 2009.

[26] S. Enguehard and B. Hatfield. Compensated atmospheric optics. *Prog. Quant. Elec.*, 19:239–301, 1995.

[27] F. Xu, A. Khalighi, P. Caussé, and S. Bourennane. Channel coding and time-diversity for optical wireless links. *Opt. Express*, 17:872–887, 2009.

[28] S. F. Clifford. Temporal-frequency spectra for a spherical wave propagating through the atmosphere. *J. Opt. Soc. Am*, 61:264–274, 1971.

[29] A. Ishimaru. Temporal frequency spectra of multifrequency waves in turbulent atmosphere. *IEEE Trans. Antennas Propag.*, 20:10–19, 1972.

[30] H. T. Yura. Temporal-frequency spectrum of an optical wave propagating under saturation conditions. *J. Opt. Soc. Am.*, 64:357–359, 1974.

[31] M. E. Gracheva, A. S. Gurvich, S. S. Kashkarov, and V. V. Pokasov. *Laser Beam Propagation in the Atmosphere ed J. W. Strohbehn*. New York: Springer, 1978.

[32] G. L. Siqueira and R. S. Cole. Temporal-frequency spectra for plane and spherical waves in a millimetric wave absorption band. *IEEE Trans. Antennas Propag.*, 39:229–235, 1991.

[33] J. Conan, G. Rousset, and P. Madec. Wave-front temporal spectra in high-resolution imaging through turbulence. *J. Opt. Soc. Am.*, 12:1559–1570, 1995.

[34] R. Rao, S. Wang, X. Liu, and Z. Gong. Turbulence spectrum effect on wave temporal-frequency spectra for light propagating through the atmosphere. *J. Opt. Soc. Am.*, 16:2755–2762, 1999.

[35] A. R. Gomez, F. Dios, J. A. Rubio, and A. Comeron. Temporal statistics of the beam-wander contribution to scintillation in ground-to-satellite optical links: an analytical approach. *Appl. Opt.*, 44:4574–4581, 2005.

[36] R. M. Manning. An optical inversion technique to remotely sense atmospheric turbulence spectra, C_n^2 profiles and cross-wind velocity. *Proc. SPIE*, 644:60–73, 1986.

[37] R. Rao and Z. Gong. High-frequency behavior of the temporal spectrum of laser beam propagating through the atmosphere. *Proc. SPIE*, 4926:175–180, 2002.

[38] F. Roddier, M. j. Northcott, J. E. Graves, D. L. McKenna, and D. Roddier. One-dimensional spectra of turbulence-induced zernike aberrations: time-delay and isoplanicity error in partial adaptive compensation. *J. Opt. Soc. Am.*, 10:957–965, 1993.

[39] D. Dravins, L. Lindegren, E. Mezey, and A. T. Young. Atmospheric intensity scintillation of stars. iii. effects for different telescope apertures. *Pub. Astron. Soc. Pac.*, 110:610–633, 1998.

[40] J. A. Anguita, I. B. djordjevic, M. A. Neifeld, and B. V. Vasic. Shannon capacities and error-correction codes for optical atmospheric turbulent channels. *J. Opt. Net.*, 4:586–601, 2005.

[41] X. Zhu and J. Kahn. Free-space optical communication through atmospheric turbulence channels. *IEEE Trans. Commun.*, 50:1293–1330, 2002.

[42] A. V. Sergeyev, M. C. Roggemann, C. Middlebrook, P. Piotr, K. Drexler, and C. Demars. An atmospheric turbulence, scattering, and weather monitoring system for three kilometers, partially over water path for monitoring the statistics of turbulence. *Proc. SPIE*, 7324:1–12, 2009.

[43] D. Giggenbach and H. Henniger. Fading-loss assessment in atmospheric free space optical communication links with on-off keying. *Optical Engineeri*, 47:046001–1–6, 2008.

Index

Adaptive optics, 20, 54, 60

Aperture, 88

Aperture averaging, 87, 90

Atmospheric inner scale, 4

Atmospheric outer scale, 4

AWGN, 90

Bandwidth, 13

Beacon, 54, 60

Beckman’s PDF, 14

Bit error rate, 75

Bit-error rate, 18

Carrier frequency, 13

Channel coding, 86

Coherence, 87

Coherence interval, 86, 89

Coherence time, 86, 90, 104

Conjugate, 65

Correlation function, 86, 104

Covariance function, 5

Deformable mirror, 54, 64

Distribution, 18

Eddies, 4

Energy, 4

Error-correction code, 12

Exponential, 14

Fading, 14

Flux variance, 93

Fourier transform, 7, 102

Free space optical, 88

Fresnel, 95

Fresnel propagator, 67

Fresnel zone, 94

Gamma-gamma, 14, 54

Gamma-gamma PDF, 57

Gaussian, 9, 65, 95, 106

Homogeneous, 6

Index of refraction, 4

Inertial forces, 4

Inertial subrange, 4

Information bits, 12

Irradiance, 93

Irradiance fluctuation, 93

Isotropic, 6

K-distribution, 14

Kolmogorov, 8, 91

Laser beam, 15

Link, 18

Log irradiance variance, 58, 59, 68

Lognormal, 14, 54

Lognormal PDF, 58

Non-reciprocal path, 81

OOK modulation, 75, 90

Optical spectrum, 13

Optimal beam, 81

Phase gradient, 62

Photo diode amplified, 100

Photodetector, 91

Planck, 91

Power spectral density, 6, 105

Power-law spectrum

- Kolmogorov, 8
- Tatarskii, 8
- von Karman, 9

Probability density function, 14, 54, 68

Propagation grid, 67

Pupil, 62, 88

Receiver, 99

Responsivity, 100

Rician, 14

Rytov variance, 92

Scattering disk, 94

Scintillation, 14, 66, 89

Scintillation index, 59, 93

Signal-to-noise ratio, 76

Spatial Coherence, 19

Spatial sampling interval, 94

Speckle, 19, 88, 104, 106

Structure function, 6

Symbol duration, 86, 89

Taylor’s hypothesis, 10, 95

Temperature fluctuations, 4

Temperature gradients, 4

Temporal, 16, 107

Tilt, 61

Transmitter, 54, 98

Turbulence, 6, 53

Viscous dissipation range, 4

Wavefront sensor, 54, 62

wavelength, 13

WFS Subaperture, 63

WFS subaperture, 83